TECHNISCHE UNIVERSITÄT DRESDEN

Multiple-Input Multiple-Output Detection Algorithms for Generalized Frequency Division Multiplexing

Maximilian Matthé

der Fakultät Elektrotechnik und Informationstechnik
der Technischen Universität Dresden

zur Erlangung des akademischen Grades eines

Doktoringenieurs
(Dr.-Ing.)

genehmigte Dissertation

Vorsitzender:	Prof. Dr. rer. nat. Johann Bartha
Gutachter:	Prof. Dr-Ing. Dr. h.c. Gerhard Fettweis
	Prof. Dr. Helmut Bölcskei
Tag der Einreichung:	01.12.2017
Tag der Verteidigung:	27.03.2018

Abstract

Since its invention, cellular communication has dramatically transformed personal lifes and the evolution of mobile networks is still ongoing. Evergrowing demand for higher data rates has driven development of 3G and 4G systems, but foreseen 5G requirements also address diverse characteristics such as low latency or massive connectivity. It is speculated that the 4G plain cyclic prefix (CP)-orthogonal frequency division multiplexing (OFDM) cannot sufficiently fulfill all requirements and hence alternative waveforms have been investigated, where generalized frequency division multiplexing (GFDM) is one popular option. An important aspect for any modern wireless communication system is the application of multi-antenna, i.e. MIMO techiques, as MIMO can deliver gains in terms of capacity, reliability and connectivity. Due to its channel-independent orthogonality, CP-OFDM straightforwardly supports broadband MIMO techniques, as the resulting inter-antenna interference (IAI) can readily be resolved. In this regard, CP-OFDM is unique among multicarrier waveforms. Other waveforms suffer from additional inter-carrier interference (ICI), inter-symbol interference (ISI) or both. This possibly 3-dimensional interference renders an optimal MIMO detection much more complex. In this thesis, we investigate how GFDM can support an efficient multiple-input multiple-output (MIMO) operation given its 3-dimensional interference structure. To this end, we first connect the mathematical theory of time-frequency analysis (TFA) with multicarrier waveforms in general, leading to theoretical insights into GFDM. Second, we show that the detection problem can be seen as a detection problem on a large, banded linear model under Gaussian noise. Basing on this observation, we propose methods for applying both space-time code (STC) and spatial multiplexing techniques to GFDM. Subsequently, we propose methods to decode the transmitted signals and numerically and theoretically analyze their performance in terms of complexiy and achieved frame error rate (FER). After showing that GFDM modulation and linear demodulation is a direct application of Gabor expansion and transform, we apply results from TFA to explain singularities of the modulation matrix and derive low-complexity expressions for receiver filters. We derive two linear detection algorithms for STC encoded GFDM signals and we show that their performance is equal to OFDM. In the case of spatial multiplexing, we derive both non-iterative and iterative detection algorithms which base on successive interference cancellation (SIC) and minimum mean squared error (MMSE)-parallel interference cancellation (PIC) detection, respectively. By analyzing the error propagation of the SIC algorithm, we explain its significantly inferior performance compared to OFDM. Using feedback information from the channel decoder, we can eventually show that near-optimal GFDM detection can outperform an optimal OFDM detector by up to 3dB for high SNR regions. We conclude that GFDM, given the obtained results, is not a general-purpose replacement for CP-OFDM, due to higher complexity and varying performance. Instead, we can propose GFDM for scenarios with strong frequency-selectivity and stringent spectral and FER requirements.

Acknowledgement

As I am completing this dissertation, I'm going back over everything I did in my studies. Here, I'd like to thank Prof. Gerhard Fettweis for growing my fascination for communications engineering and signal processing already in my undergraduate studies in 2008. This passion remained over the years and eventually peaked in this dissertation. I thank Gerhard for offering me a position in the Vodafone Chair at TU Dresden during 2013–2017, for supervising me over the years and giving valuable feedback during meetings and seminars. I also thank Prof. Helmut Bölcskei for taking time to review this work as my second supervisor and providing his valuable feedback.

Special thanks goes to Prof. Luciano Leonel Mendes who gave important initial research impulses and taught me how to efficiently write and revise papers. My publication record would not have been possible without his professional guidance. Our group leader Dr. Dan Zhang had always been available for technical exchange, reviews and administrative questions and deserves my highest gratefulness. Our discussions about stochastic signal processing, estimation theory and iterative receivers were invaluable and eventually led to the results presented in Chapter 4, 5 and 6 in this thesis.

Additionally, I want to express my gratitude to Dr. Nicola Michailow and Dr. Ivan Simões Gaspar for rising my interest to GFDM in the first place during my Diploma thesis and for being trustful and valuable colleagues during my Dissertation work. Moreover, thankfulness goes to my colleagues Ahmad, Albrecht, Ana, Martin, Shahab, Roberto, Song, Zhitao for interesting discussions, reviewing this thesis and nice lunch breaks. Kathrin and Sylvia deserve my honest esteem for keeping the chair running and support in any organizational matters.

Finally, I want to thank my parents for supporting my studies and permanent expression of believe in me and my skills. My girlfriend Steffi deserves my heartful affection for supporting me in any situation in life, understanding sometimes stressful times and together with our daughter Pauline maintaining such important and pleasurable diversion from work.

Dresden, November 2017 Maximilian Matthé

Contents

1 Introduction **1**
1.1 Alternative Waveform Candidates . . . 2
1.2 MIMO Wireless Techniques . . . 4
1.3 Contribution of this Work . . . 5
1.4 Prior Work . . . 7
1.5 Notation . . . 7

2 Fundamentals **9**
2.1 Wireless Communication Systems . . . 9
2.2 Wireless Channel . . . 10
2.3 Generic MIMO Receiver . . . 14
2.4 GFDM Fundamentals . . . 17
2.4.1 GFDM Parameters . . . 17
2.4.2 GFDM Modulation . . . 19
2.4.3 Linear GFDM Demodulation . . . 22
2.5 Summary . . . 25

3 Multicarrier Systems in the Context of Gabor Theory **26**
3.1 Time-Frequency Analysis and Gabor Theory . . . 26
3.1.1 The Continuous-Time Case . . . 26
3.1.2 The Finite Discrete-Time Case . . . 30
3.2 Multicarrier Systems and Gabor Theory . . . 32
3.3 GDFM in a Gabor Transform Setting . . . 35
3.4 Summary . . . 38

4 Transmit Diversity Techniques for GFDM **40**
4.1 The Alamouti Space Time Block Code . . . 41
4.2 The Alamouti STBC for GFDM . . . 43
4.2.1 Time-Reversal Space-Time Coding for GFDM . . . 44
4.2.2 Widely Linear Equalization for Space-Time Coded GFDM . . . 45
4.2.3 Simulation Results . . . 48
4.3 Summary . . . 51

5 Non-Iterative Detection for Spatially Multiplexed GFDM 52
5.1 The Linear Model as a Lattice Transform . . . 54
5.2 Successive Interference Cancellation for GFDM . . . 58
5.2.1 Basic Algorithm Description . . . 59
5.2.2 Overcoming Error Propagation . . . 60
5.2.3 Simulation results . . . 62
5.3 Summary . . . 67

6 Iterative Detection for Spatially Multiplexed GFDM 68
6.1 Iterative MIMO Detection . . . 68
6.2 Iterative MMSE-PIC Detection for MIMO-GFDM . . . 69
6.2.1 CWCU LMMSE Estimation . . . 70
6.2.2 SISO LMMSE Demapping . . . 71
6.2.3 Factorization of the channel matrix . . . 72
6.2.4 Low-Complexity Approximation . . . 76
6.3 Simulation results . . . 79
6.3.1 Approximation accuracy . . . 81
6.3.2 MMSE-PIC demapper information transfer . . . 82
6.3.3 Channel decoder information transfer . . . 82
6.3.4 Decoding performance of different channel codes . . . 83
6.3.5 Convergence behaviour . . . 84
6.3.6 Power delay profile and subcarrier allocation . . . 85
6.3.7 Performance with different MCS . . . 86
6.3.8 Achieving the ML detection performance . . . 88
6.4 Summary . . . 89

7 GFDM - A promising waveform? 90

8 Conclusions and Future works 94
8.1 Summary of the results . . . 94
8.2 Open Research Topics . . . 96

Appendix A Proofs 99
A.1 Derivation of Widely Linear Estimator for STC-GFDM . . . 99
A.2 Uncoded Symbol Error Rate of TRSTC . . . 100
A.3 Proof of (6.17) . . . 101

List of Figures

1.1 Comparison of OOB emission of 5G candidate waveforms. 4

2.1 Generic system model of a wireless point-to-point communications system . 9
2.2 Temporal autocorrelation of a single Rayleigh tap. 12
2.3 Separation of the outer receiver into a demapper and decoder block. 15
2.4 GFDM Block structure overview. 18
2.5 Block structure of type I and II GFDM configurations. 19
2.6 GFDM modulation matrix in time and frequency domain. 21
2.7 Performance comparison of linear GFDM receivers. 25

3.1 Example of STFT. 27
3.2 Time and frequency response of biorthogonal filters. 35
3.3 Effect of even and odd M and different rolloff factors on DZT and SER. . . 38

4.1 Example of a flat-fading system exploiting transmit diversity. 41
4.2 Sample equivalent channel illustration. 47
4.3 Simulated performance for TRSTC GFDM. The overhead due to CP for GFDM and OFDM is considered in the E_b/N_0 calculation. 49
4.4 Simulated performance for widely linear MMSE equalization for STC-GFDM. 50

5.1 Comparison of GFDM and OFDM channel structure. 53
5.2 Simulation of minimum distance of OFDM, SC-FDMA and GFDM. 57
5.3 Example of $d_{\min}$ for OFDM and GFDM. 58
5.4 Example $\mathbf{R}$ after QR decomposition. 59
5.5 Detection algorithm from [MGZF15]. The subscripts $S, \bar{S}, :$ denote the last S, all but the last S, and all elements of the subscripted object, respectively. 60
5.6 Soft-SIC demapping algorithm. 61
5.7 K-best demapping algorithm 62
5.8 Uncoded and coded performance of the proposed SIC algorithm. 63
5.9 Histograms of distance difference for GFDM and OFDM. 64
5.10 Histograms of LLR at demapper output at $E_b/N_0 = 15$dB in Channel 1. . . 65
5.11 FER comparison for the proposed demappers in Channel 1. 66

6.1 Schematic representation of an iterative receiver. 69
6.2 Interference structure of data in frequency domain. 72
6.3 Factorized equation system in the noiseless case. 73

6.4 Block diagram of the 3-step MMSE estimation process. 75
6.5 Frame structure. 79
6.6 Information transfer characteristics for GFDM. 81
6.7 Coded FER performance of GFDM. 81
6.8 Information transfer chart of the SISO demapper. 83
6.9 Performance of CC and LDPC channel codes. 84
6.10 Convergence behaviour of GFDM and OFDM. 85
6.11 FER performance for 64QAM modulation, code rate $r = 3/4$ and $\alpha = 1$ for EVA and ETU block fading channels. 86
6.12 Performance of MMSE-PIC iterative receiver with different MCS. 87
6.13 ML lower bound for the GFDM and OFDM. 88

List of Tables

2.1 Power delay profiles of ETU and EVA channels. 11
2.2 Relation of OFDM and GFDM Type I, Type II parameters. 19

4.1 Simulation parameters for space-time coding simulations. 49

5.1 System parameters used for the simulation. 63

6.1 Algorithm description of the Conjugate Gradient Method. 78
6.2 GFDM and OFDM configuration used in the simulation. 80

List of Abbreviations

3GPP	3rd generation partnership project
4G	4th generation
5G	5th generation
AD	analog to digital
AWGN	additive white Gaussian noise
BCJR	Bahl-Cocke-Jelinek-Raviv
BFDM	bi-orthogonal frequency division multiplexing
BLT	Balian-Low theorem
CC	convolutional code
CFO	carrier frequency offset
CGD	conjugate gradient
CIR	channel impulse response
CP-OFDM	cyclic-prefix orthogonal frequency division multiplexing
CP	cyclic prefix
CR	cognitive radio
CSI	channel state information
CWCU	component-wise conditionally unbiased
DA	digital to analog
DFT	discrete Fourier transform
DTFT	discrete-time Fourier transform
DZT	discrete Zak transform
ETU	Extended typical urban
EVA	Extended vehicular A
EXIT	extrinsic information transfer
F-OFDM	filtered OFDM
FBMC/FMT	filter-bank multicarrier filtered multitone
FBMC/OQAM	filter-bank multicarrier offset-QAM
FBMC	filter-bank multicarrier
FCC	Federal Communications Commission
FDMA	frequency division multiple access
FEC	forward error correction
FER	frame error rate
FFT	fast Fourier transform
FMT	filtered multitone
FTN	faster-than-Nyquist
FT	Fourier transform

GFDM	generalized frequency division multiplexing
HARQ	hybrid automatic repeat request
IAI	inter-antenna interference
IBI	inter-block interference
ICI	inter-carrier interference
IDFT	inverse discrete Fourier transform
ISI	inter-symbol interference
LDPC	low-density parity check
LLR	log-likelihood ratio
LMMSE	linear minimum mean squared error
LR	lattice reduction
LTE	Long Term Evolution
M2M	machine to machine
MAP	maximum a-posteriori
MCS	modulation and coding scheme
MF	matched filter
MIMO	multiple-input multiple-output
ML	maximum likelihood
MMSE-PIC	minimum mean squared error with parallel interference cancellation
MMSE	minimum mean squared error
MRC	maximum ratio combining
MSE	mean squared error
NEF	noise enhancement factor
NLOS	non-line of sight
NR	new radio
OFDMA	orthogonal frequency division multiple access
OFDM	orthogonal frequency division multiplexing
OOB	out-of-band
OQAM	offset-QAM
P-OFDM	pulse-shaped OFDM
PAPR	peak-to-average power ratio
PDF	probability density function
PDP	power delay profile
PHY	physical layer
PIC	parallel interference cancellation
PRB	physical resource block
QAM	Quadrature amplitude modulation
RC	raised cosine

RF	radio frequency
RRC	root raised cosine
RSCC	recursive systematic CC
SC-FDMA	single-carrier frequency division multiple access
SD	sphere decoder
SER	symbol error rate
SFC	space-frequency code
SIC	successive interference cancellation
SISO	soft-in soft-out
SMR	specialized mobile radio
SM	spatial multiplexing
SNR	signal to noise ratio
SPA	sum product algorithm
STBC	space-time block code
STC	space-time code
STFT	short-time Fourier transform
STO	symbol timing offset
TDL	tapped delay line
TFA	time-frequency analysis
TR-STC	time-reversal STC
TTI	transmission time interval
UF-OFDM	universal filtered OFDM
URLLC	ultra-reliable low-latency communications
W-OFDM	windowed OFDM
WCP-COQAM	windowed CP offset-QAM
WH	Weyl-Heisenberg
WLAN	wireless local area network
WLE	widely linear estimation
WOLA	weighted overlap-and-add
ZF	zero-forcing
ZT	Zak transform
eMBB	enhanced mobile broadband
mMIMO	massive MIMO
mMTC	massive machine-type communication

Mathematical Notation

Operators and Functions

$\|\cdot\|^2$	Euclidean Norm
$(\cdot)^T$	Matrix transpose
$(\cdot)^H$	Matrix conjugate transpose
$(\cdot)^{-1}$	Matrix inverse
$E[\cdot]$	Expectation operator
$\langle a, b\rangle$	Standard scalar product in L2
$\langle x\rangle_N$	argument x modulo N
$\circ$	Hadamard product (elementwise product)
$\oslash$	Elementwise division
$\otimes$	Kronecker product
$(\cdot)^{\circ -1}$	Elementwise inversion
$\mathrm{DFT}_N(\cdot)$	N-point discrete Fourier transform
$\mathrm{IDFT}_N(\cdot)$	N-point inverse discrete Fourier transform
$\mathrm{sinc}(x)$	Sinc-function, $\mathrm{sinc}(x) = \sin(\pi x)/(\pi x)$
$\delta[n]$	Discrete delta function
δ_{jk}	Kronecker delta symbol
$\mathcal{M}(\vec{b})$	Bit-Mapping function to map bits to constellation symbols

Mathematical Symbols

$\mathbb{B}$	Binary set, $\{0, 1\}$
$\mathbb{R}$	Set of real numbers
$\mathbb{C}$	Set of complex numbers
$\mathbb{Z}$	Set of integers
$\ell^2(\mathcal{X})$	Set of square-summable sequences indexed by the set X
$\mathcal{S}$	Set of constellation symbols
$\mathcal{C}$	Set of possible codewords
N_T	Number of transmit antennas
N_R	Number of receive antennas
M	Number of GFDM subsymbols
K	Number of subcarriers
N	Number of samples per block
μ	Number of bits per QAM symbol
$\vec{b}$	Payload bits
$\vec{b}_c$	Encoded bits
$\vec{d}$	Data vector of constellation points
$x[n], \vec{x}$	Transmit signal (time-domain)
$y[n], \vec{y}$	Received signal (time-domain)
n	Discrete time domain index
ν	Discrete frequency domain index
t	Continuous time coordinate
f	Continuous frequency coordinate
F_s	Baseband sampling frequency
T_S	(Sub)symbol duration
f_D	Doppler spread
f_c	Carrier frequency
$\vec{w}$	Additive white Gaussian noise vector
$\mathbf{H}$	Channel coefficient matrix in $\vec{y} = \mathbf{H}\vec{d} + \vec{w}$
$\mathbf{F}_N$	Unitary N-point DFT matrix
$\lambda^p_{i,b}$	LLR of bth bit in ith constellation symbol

Chapter 1

Introduction

The advancement of wireless and in particular cellular communication systems has a tremendous impact on both personal daily life and global economy. While the 2nd generation of cellular communication networks brought instant, mobile communication to the people, 4th generation (4G) networks allow ubiquitous internet access, social media and on-demand video streaming.

As the development of cellular communication advances, new use cases are being discussed for the 5th generation (5G) of cellular communications [NGM15]. Most obvious, mobile broadband applications will remain to play a central role in future mobile networks. 5G enhanced mobile broadband (eMBB) aims to support additional features like augmented or virtual reality and inter-user interaction which will increase the required data rate beyond current capacities. Further envisioned use cases for 5G include massive machine-type communication (mMTC), where a massive number of low-cost devices is connected to the network, which require sporadic traffic with low energy consumption [ZBC+14]. Applications include smart wearables such as sensors within clothes or sensor networks measuring traffic or environmental conditions in many places in urban or rural areas. The Tactile Internet [SAD+16, Fet14] enables seamless control of remote objects due to ultra-low latency of the communication link. Moreover, ultra-reliable low-latency communications (URLLC) facilitates applications such as automated traffic control and driving, cloud-controlled robot networks or remote surgery [Eri17].

The diverse applications of the envisioned 5G cellular network require a massive rework of all system aspects, such as operations and management facilities, network structure and radio air interface [NGM15]. In this thesis, we will focus on the constitutional basis of the radio air interface: the physical layer (PHY) of the cellular communications system.

The foundation of any PHY implementation is the choice of the waveform which is used to convey messages over the air. While in 2G systems a narrow-band single-carrier system was used [Rah93], 3G employed a wideband CDMA technique [Ric00a]. 4G systems have employed the multicarrier system cyclic-prefix orthogonal frequency division multiplexing (CP-OFDM)[1] in combination with frequency division multiple access (FDMA) for the downlink from the base station to the terminal and the single-carrier frequency

[1] In this work, when referring to OFDM, we implicitely assume the cyclic-prefix aided OFDM waveform which is used by LTE and WiFi.

division multiple access (SC-FDMA) waveform for the uplink in the opposite direction [WZR+16]. Dominated by the need for higher data rates, the choice of the 4G waveforms was led by the flexible orthogonal frequency division multiple access (OFDMA) scheme and a straightforward applicability of multi-antenna technologies to achieve unprecedented spectral efficiencies [JKL+17]. Moreover, both SC-FDMA and OFDMA offer a low-complexity implementation by means of efficient fast Fourier transform (FFT) operations [Bin90].

With the envisioning of 5G use cases it became evident that the plain 4G CP-OFDM system cannot provide the flexibility that is required by upcoming applications [BBC+14]. Its constraint on strict synchronization depends upon bulky synchronization schemes, which creates a severe overhead for sporadic, energy-efficient traffic [WJK+14]. Its inherently high out-of-band (OOB) emission requires large guard bands between adjacent channels, which reduces spectral efficiency and inhibits a heterogenouos signal structure within a single transmission band [FB11]. High peak-to-average power ratio (PAPR) as a general problem of multicarrier waveforms inhibits energy-efficient power amplifiers, which gave rise to the usage of SC-FDMA in the 4G uplink. In this context, research on 5G waveform improvements arose, aiming to overcome the limitations of plain OFDM.

1.1 Alternative Waveform Candidates

The research on alternative multicarrier techniques led to two different paths in the journey towards the 5G waveform. On the one side, attempts to keep the 4G PHY mainly unchanged and to apply techniques on top of OFDM to mitigate the above mentioned drawbacks are mainly pursued by industrial research. In this regard, frame structure, pilot pattern and synchronization sequence design can be reused from the proven 4G PHY. OOB supression for OFDM can be achieved by filtering the OFDM waveform on a subband basis and was proposed by Nokia and Huawei in the form of universal filtered OFDM (UF-OFDM) [SW14, VWS+13] and filtered OFDM (F-OFDM) [AJM15, ZJC+15], respectively. Furthermore, windowed OFDM (W-OFDM) [AKR16] was proposed as a more flexible method for filtering the OFDM signal on a subcarrier basis. Eventually, pulse-shaped OFDM (P-OFDM) [ZSW+15] as a generalization of W-OFDM was proposed to further exploit a tradeoff between controllable inter-symbol interference (ISI) and spectral confinement. The problem of high PAPR for OFDM, which is a problem for multicarrier waveforms in general, is addressed by numerous techniques which are generally applicable to multicarrier waveforms, see e.g. [HL05]. Moreover, the requirement for strict synchronization for OFDM is relaxed by the reduced OOB emission, such that frequency-adjacent, independent systems do not interfer each other and hence can run asynchronously.

The alternative path, which is more closely followed by academia, is to examine waveforms, which are not necessarily limited to the orthogonal techniques used in 4G. Hence, the fundamental limitations of OFDM can be circumvented by completely new designs rather than outmaneuvering them with advanced signal processing on top of OFDM. In general, new waveforms give up the channel independent orthogonality (cf. Sec. 3.2)

or even orthogonality in general, and hence introduce self-interference at the receiver side. Even though self-interference at first seems to have a negative impact on the error performance, in the upcoming chapters we will reveal that self-interference can actually be harnessed. As OFDM alternatives, waveforms such as filter-bank multicarrier offset-QAM (FBMC/OQAM) [Bel10, CPN14], windowed CP offset-QAM (WCP-COQAM) [LS14], filtered multitone (FMT) [CEÖ02, AFB11], bi-orthogonal frequency division multiplexing (BFDM) [KWJM14] and generalized frequency division multiplexing (GFDM) [MMG+14] are under investigation in the context of foreseen 5G requirements. Generally, all mentioned multicarrier waveforms apply subcarrier-based filtering to reduce OOB emissions at the cost of either self-interference or rate-reduction[2]. The group of linearly filtered waveforms, i.e. BFDM, filter-bank multicarrier (FBMC) and FMT achieve unprecedentedly low levels of OOB emissions at the cost of long filter tails that are not suitable for low-latency transmissions [SWC14]. On the other hand, circularly filtered waveforms such as WCP-COQAM and GFDM generally need additional means for OOB reduction such as windowing [MMGF14], but result in a block-structured transmission which is more suitable for low-latency transmissions. Moreover, inserting a CP between the blocks isolates adjacent blocks, which can then be processed separately at the receiver, facilitating frequency-domain processing.

In the literature, numerous studies on the link-level performance of both OFDM-derived waveforms and OFDM-alternatives are available. For example, even though all waveforms clearly outperform OFDM in terms of lower OOB emission (see Fig. 1.1 from [ZMMF17]), large differences between the obtained OOB levels exist. However, depending on the actual application, different levels of OOB emission are acceptable and henceforth, reducing OOB emission below a certain threshold, possibly at the cost of other performance metrics, does not yield benefits. Hence, diverse results on the waveform performance are obtained in literature, depending on the specific application requirements. For example, in [BBC+14] P. Banelli et. al compared spectral efficiency of FBMC, OFDM and SC-FDMA and conclude no clear winner, instead they argue the optimal waveform depends on the actual application scenario. Moreover, in [LLJ+15] several waveform candidates are conceptually compared regarding suitable applications. With the broad requirements of 5G use cases, it is widely accepted that a single waveform parametrization will not be able to jointly fulfill all foreseen requirements and several waveforms have their niches. Hence, flexibility of the PHY is considered a key factor for a successful 5G PHY implementation [SZÖ+17].

Eventually, as the 5G standardization progressed for early 5G standards, the 3rd generation partnership project (3GPP) consortium [3GP17] defined the waveform to be a relative to OFDM, such as F-OFDM or UF-OFDM [Nag17] but leaves freedom to the vendors, how it is actually implemented. The standard solely requires the waveform to obey a given spectral mask, without defining how this spectrum is achieved. The reasons for eventually relying on OFDM-relatives instead of employing a completely new waveform are numerous. Early 5G standard releases aim to mainly keep the Long Term Evolution

[2] Subband filtering for OFDM also implies ISI or rate reduction due to extended cyclic prefix (CP) lengths or overlapping filter tails.

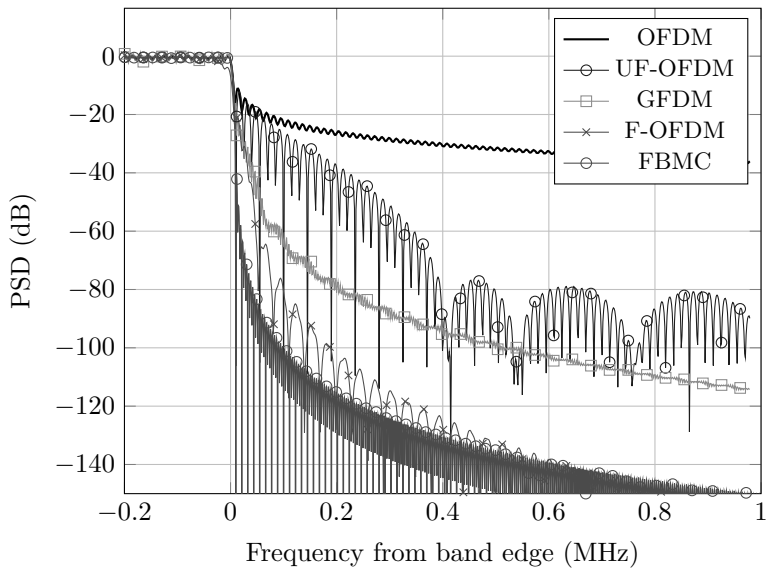

Figure 1.1: Comparison of OOB emission of 5G candidate waveforms at a sampling frequency of 23.04MHz split into 1536 subcarriers, i.e. subcarrier spacing equals 15kHz. F-OFDM and UF-OFDM use a subband that consists of 12 subcarriers, and filters as proposed in [ZJC+15, SWC14]. GFDM employs 15 subsymbols, raised cosine filtering and windowing as in [MMG+14]. FBMC uses the PHYDYAS filter [Bel10] of length $4 \cdot 1536$ samples. Data taken from [ZMMF17]

(LTE) frame structure, with only a scaled numerology for different applications [GWT+17, VZV+16]. Here, subband filtered OFDM-relatives offer the necessary seperation between the channels for different applications. The effort required for designing a completely new frame structure when using a disruptive waveform were not considered worth the marginal gains of alternative waveforms and OFDM-relatives are simply considered "good-enough". Nevertheless, research on OFDM alternatives is important, given that current solutions are merely workarounds for the problems of OFDM. Moreover, theoretical and practical insights gained while researching non-orthogonal waveforms with their inherent ICI can be fed back to OFDM improvement under e.g. non-ideal conditions such as high mobility scenarios.

1.2 MIMO Wireless Techniques

A crucial aspect for any modulation technique is the application of multi-antenna technologies, which are also known as multiple-input multiple-output (MIMO) techniques, since the resulting wireless channel has multiple inputs (i.e. transmit antennas) and multiple outputs (i.e. receive antennas). Through the use of multiple antennas at the transmitter and/or the receiver, significant improvements in terms of link reliability, coverage or spectral efficiency can be achieved compared to single-antenna systems (see e.g. [TV05, YH15]). This compelling property makes MIMO play a central role in both today's cellular (e.g. LTE) and wireless local area network (WLAN) (e.g. IEEE 802.11n [IEE09]) communication systems. Undoubtedly, 5G will adopt and build upon MIMO techniques for its air interface due to the massive gains compared to single-antenna systems [NGM15].

Here, we want to emphasize two specific gains that are achievable by traditional MIMO transmission, which are described as follows [TV05]. Additional gains stemming from MIMO architectures include *array gain* [OPF12] and *multi-user gain* [SKS+16].

Diversity Gain. Wireless techniques obtaining diversity gains transmit the same information over multiple fading links. By means of independent fading, it becomes more unlikely that all links are in a deep fade, eventually improving the robustness of the transmission. We can distinguish between three types of diversity: temporal diversity, frequency diversity and spatial diversity. Temporal diversity and frequency diversity exploits temporal and spectral variations of the wireless channel due to movement and multipath propagation. Both techniques are applicable to both single- and multi-antenna systems, but transmitting the same information over two time- or frequency resources reduces the gross data rate. Thus, based on the assumption that the wireless channels between different transmit and receive antenna pairs experience independent fading, spatial diversity is an additional dimension of diversity in MIMO systems, which does not reduce data rate compared to single-antenna systems. Whereas exploiting diversity with multiple receive antennas is rather trivial [CGE03], more advanced methods were developed to obtain transmit antenna diversity, where the Alamouti space-time code (STC) [Ala98] is one popular example.

Multiplexing Gain. Instead of transmitting the same information over several different transmit antennas, using MIMO techniques it is possible to send independent messages over each transmit antenna. Hence, the data rate is increased compared to a single antenna system without increasing the required bandwidth. This technique is called spatial multiplexing (SM) and the so-called SM gain grows linearly with the minimum of number of transmit and receive antennas [TV05]. Therefore, an increased number of antennas is one of the main reasons for the ever-increasing data rates of modern wireless systems, such as WiFi and LTE, which already nowadays propose to use 8 transmit and receive antennas [Pen15]. Moreover, the proposal of massive MIMO (mMIMO) systems [LMLS14, FMFM14] further increases the number of antennas at the base stations to combine SM gains with beamforming gains to support multiple users at different spatial locations. Consequently, it is no surprise, that discussions about upcoming 5G systems will heavily rely on SM techniques to further boost the achievable data rate.

1.3 Contribution of this Work

While the research on alternatives to OFDM for 5G applications has brought important results regarding spectral efficiency, complexity, spectral properties, few results on the important aspect of MIMO detection for these waveforms are available. However, to consider a waveform to be a serious contestant to OFDM, it is essential to prove its applicability in MIMO systems. Whereas applying MIMO techniques to OFDM derivatives such as (U)F-OFDM is straight-forward [ZMMF17], the self-interference of non-orthogonal alternatives rises problems due to interference resolution and algorithm complexity [ZMMF16].

The goal of this thesis is to design, analyze and optimize algorithms for MIMO detection for non-orthogonal waveforms, where we choose GFDM as a role model for waveforms with subcarierrer-localized interference[3]. To this end, we identify the problems that arise from self-interference for state-of-the-art MIMO detection and propose solutions to overcome and beneficially exploit this interference. In particular, we propose both linear and non-linear MIMO detection algorithms for MIMO-GFDM aiming for both diversity and multiplexing gains. We analyze the proposed algorithms in terms of detection performance, arithmetic complexity and parallelizability for hardware implementation. As a benchmark, we compare the obtained results with state-of-the-art detection algorithms for MIMO-OFDM systems, as they are used in modern communication systems. In more detail, the sequel of this work is structured as follows:

Chapter 2 introduces the necessary fundamentals. After presenting a generic wireless transceiver model, we outline the model of the Rayleigh fading multipath channel which is employed throughout the thesis. Subsequently, we recap the fundamentals of soft-out MIMO detection and detail the soft QAM demapping operation. Chapter 2 concludes with a description of the single-antenna GFDM system and summarizes the error rate performance of linear GFDM receivers.

Before we dive into the details of MIMO detection for GFDM, Chapter 3 relates generic multicarrier systems to the mathematical theory of time-frequency analysis. We describe the relation between the Gabor expansion/transform pair and linear GFDM transmitter/receiver operations and identify the GFDM modulation as a critically sampled Gabor expansion. From this observation, we obtain theoretical properties and low-complexity implementation formulations for GFDM as direct consequences of the underlying Gabor transform structure of GFDM.

In Chapter 4 we present two techniques for GFDM for achieving transmit diversity in a MIMO system. After introducing the basic Alamouti space-time block code, we point out the problems that arise for the application to the non-orthogonal GFDM system. Subsequently, we propose both time-reversal space-time coding and widely linear equalization for GFDM to overcome these problems and to obtain the desired transmit diversity. We conclude this chapter with simulated error rate performance of both proposals.

Chapter 5 and 6 focus on the problem of detecting spatially multiplexed GFDM signals with iterative and non-iterative receivers, respectively. After understanding the MIMO detection as a search for the closest point in a lattice, we present an analysis of the minimum distance of OFDM and GFDM in Chapter 5. We show that GFDM achieves a larger minimum distance for uncoded transmission, indicating a larger capacity for GFDM modulated signals. We propose a receiver algorithm for MIMO-GFDM which is based on successive interference cancellation (SIC), that significantly outperforms OFDM with uncoded transmission, and in addition we analyze reasons why it performs poorly with coded transmissions. Based on these observations, in Chapter 6 we analyze the performance of MMSE with parallel interference cancellation (MMSE-PIC) iterative MIMO detection for GFDM and propose low-complexity approximations that achieve feasible

[3] Other OFDM alternative waveforms also focus on low OOB and hence their subcarriers do not overlap a lot, meaning they all have subcarrier-localized interference.

complexity with superior error performance compared to OFDM. Moreover, we compare the effect of low-density parity checks (LDPCs) and convolutional codes (CCs) on the detection performance and find out that CCs are more suitable for the detection problem at hand.

The short chapter 6 is dedicated to discussing the applicability of GFDM to real-world problems. We highlight problems of commonly used OFDM systems and explain, how GFDM can be more suitable for particular use cases. Finally, the achievements of this work are summarized in Chapter 8 and important remaining challenges for MIMO-GFDM detection are discussed.

1.4 Prior Work

Despite GFDM being a relatively recent topic[4], its research has gained traction in other research groups. In parallel to the results presented in this work regarding MIMO detection for GFDM, advances have been achieved and published on other aspects of GFDM. For example the modeling of symbolic expressions for error rates were studied in e.g. [Bru13, BDM15, YGR16]. There, closed form expressions or approximation for linear receivers in multipath or time-variant channels are presented and verified. The reduction of complexity at the transmitter side and for linear receivers was in the focus of the works in e.g. [FMD15b, CSH17, WXXL16], that mainly exploit the modulation matrix structure which bases on the underlying Gabor structure of GFDM. The authors proposed solutions whose complexities are only slightly higher than that of OFDM, making the implementation feasible on today's hardware. Regarding the detection for MIMO-GFDM systems, few results outside of the author's research group are available in the literature. A rudimentary possibility to perform linear detection for spatially multiplexed MIMO-GFDM was conceptually proposed in [FBM15], though no performance evaluation was presented. In [TWD+15], the authors compared different 5G waveform candidates under large-scale MIMO systems employing linear receivers. Though, the criterion for the detection was different between the waveforms, making the comparison unfair. In their work, GFDM performed poorly compared to a plain OFDM system. The authors in [ÖBÇ17] employed GFDM in the context of a relatively new MIMO technique called *spatial modulation* [RHG11]. There, the authors showed a potential for GFDM to be used in future wireless networks, though only uncoded performance comparison was conducted and hence the results are not too trustworthy. Besides the mentioned works, no considerable work on MIMO-GFDM is available in literature.

1.5 Notation

$\mathbb{Z}, \mathbb{R}, \mathbb{C}$ denote the set of integers, real and complex numbers and $\mathcal{X}^N$ describes N-dimensional tuples of elements of the set $\mathcal{X}$. $\mathbb{B}$ is the set of of binary digits, i.e. $\mathbb{B} = \{0, 1\}$. $L^2(\mathbb{R})$ denotes the space of square integrable functions defined on the real line. $\ell^2(\mathcal{X})$ cor-

[4] The first mentioning was in [FKB09]

responds to the set of square-integrable sequences defined on the set $\mathcal{X}$ and $[\ell^2(\mathcal{X})]^N$ is the set of N-dimensional tuples of elements of $\ell^2(\mathcal{X})$.

Matrices and vectors are denoted in boldface and with an arrow on top, as in $\mathbf{X}, \vec{x}$. The transpose and hermitian transpose operation are denoted by $\mathbf{X}^T, \mathbf{X}^H$, respectively. The $N \times N$ identity matrix is written as $\mathbf{I}_N$, where we omit the index if it can be read from the context. $\vec{e}_i$ is the ith column of the identity matrix. The Kronecker and Hadamard product are denoted by $\otimes$ and $\circ$, respectively and $\oslash$ denotes elementwise vector or matrix division. The matrix vectorization operation is denoted as $\mathrm{vec}(\mathbf{X})$ which stacks the columns of $\mathbf{X}$ on top of each other. Moreover, $\langle x \rangle_N$ denotes the remainer of x divided by N. $\sqrt{\mathbf{X}}, \sqrt{\vec{x}}$ denote the element-wise square root of the matrix of vector $\mathbf{X}$, $\vec{x}$, respectively.

Moreover δ_{ij} denotes the Kronecker delta symbol and $\delta(t)$ denotes the Dirac delta distribution. $\vec{1}_N$ and $\vec{0}_N$ denote the length N vectors of all ones or zeros, respectively.

The unitary Fourier transform for $x \in L^2(\mathbb{R})$ and its inverse are defined as

$$X(f) = \int_{\mathbb{R}} x(t) \exp(-j2\pi f t) dt \qquad x(t) = \int_{\mathbb{R}} X(f) \exp(j2\pi f t) df. \tag{1.1}$$

The discrete Fourier transform of a sequence $x[n], n = 0, \ldots, N-1$ and its inverse operation are given by

$$X[f] = \mathrm{DFT}_N\{x[n]\} = \sum_{n=0}^{N-1} x[n] \exp\left(-j2\pi \frac{nf}{N}\right) \tag{1.2}$$

$$x[n] = \mathrm{IDFT}_N\{X[f]\} = \frac{1}{N} \sum_{f=0}^{N-1} X[f] \exp\left(j2\pi \frac{nf}{N}\right). \tag{1.3}$$

The unitary N-dimensional Fourier transform matrix $\mathbf{F}_N$ is given by

$$\mathbf{F}_N = (\tfrac{1}{\sqrt{N}} w^{lk})_{l=0,\ldots,N-1,k=0,\ldots,N-1} \text{ with } w = \exp(-j2\pi/N)$$

and fulfills $\mathbf{F}_N \mathbf{F}_N^H = \mathbf{F}_N^H \mathbf{F}_N = \mathbf{I}_N$. Moreover, $\mathrm{circ}(\vec{x})$ returns the circulant matrix with $\vec{x}$ being its first column.

Chapter 2

Fundamentals

Before we can dive into the techniques to make MIMO transmission accessible to GFDM, we need to address relevant fundamental principles that evolve around wireless communications and GFDM. In this chapter, we introduce the general notation for a wireless communication system and describe the considered wireless channel model from which we derive the fundamental linear signal model that is used throughout this work. Moreover we introduce the generic building blocks of a MIMO detector. Eventually, we describe the GFDM system in detail and relate its configuration parameters to the well-known OFDM configuration.

2.1 Wireless Communication Systems

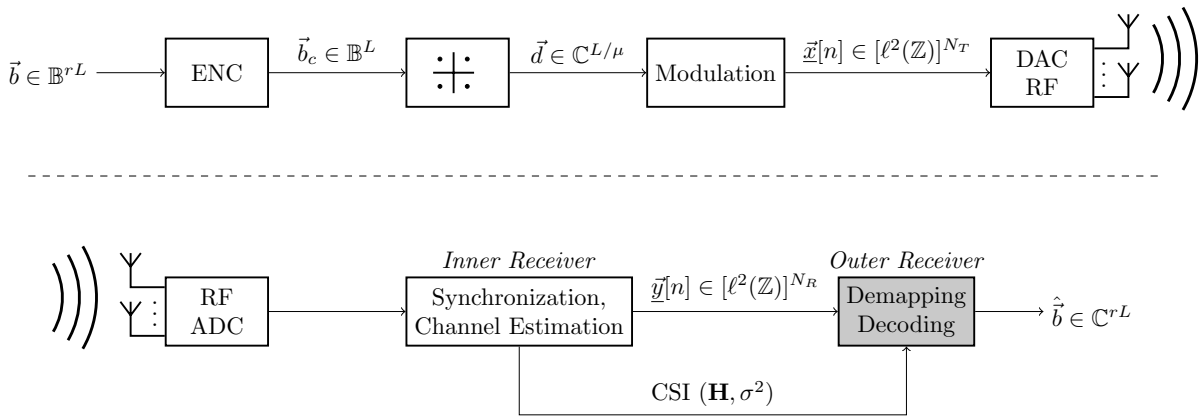

Figure 2.1: Generic system model of a wireless point-to-point communications system

Fig. 2.1 shows a generic system model of a MIMO wireless point-to-point communication systems with N_T transmit and N_R receive antennas. A message $\vec{b} \in \mathbb{B}^{rL}$ consisting of rL bits is encoded with a channel encoder (ENC) with code rate r to yield a codeword $\vec{b}_c \in \mathbb{B}^L$ of length L. We assume that potenial interleaving is already contained within the encoding operation. The codeword is separated into bit groups of length μ and each group is mapped to a complex value from the discrete constellation set $\mathcal{S}$ consisting of 2^μ constellation symbols. In this work, we consider $\mathcal{J}$-QAM modulation with $\mathcal{J} = 2^\mu$. We assume

the resulting constellation points $\vec{d} = \vec{\mathcal{M}}(\vec{b}_c) \in \mathbb{C}^{L/\mu}$ to be uncorrelated and of unit energy, i.e. $E[\vec{d}\vec{d}^H] = \mathbf{I}$. Here, $\vec{\mathcal{M}}(\vec{b}_c)$ describes the mapping from bits to constellation symbols. Throughout this thesis, we assume Gray mapping [Pro95]. In the subsequent modulator, for each transmit antenna a complex-valued baseband transmit signal $\underline{\vec{x}}[n] \in [\ell^2(\mathbb{Z})]^{N_T}$ is then formed from the complex Quadrature amplitude modulation (QAM) symbols $\vec{d}$. Eventually, the baseband signal from each transmit antenna is transformed to an analog signal, upconverted to the carrier frequency and transmitted over the wireless channel.

At the receiver side, the signal at each receive antenna is first downconverted, sampled and quantized to yield the digital received baseband signal, where we assume ideal quantization and no sampling jitter. In the inner receiver synchronization and channel estimation is performed, i.e. the inner receiver compensates time and frequency offset and forwards the signal $\underline{\vec{y}}[n] \in [\ell^2(\mathbb{Z})]^{N_R}$ together with the estimated channel state information (CSI) to the following outer receiver.

The outer receiver uses the baseband signal $\underline{\vec{y}}[n] \in [\ell^2(\mathbb{Z})]^{N_R}$ and estimated CSI to yield an estimate $\hat{\vec{b}} \in \mathbb{C}^{rL}$ of the transmitted message. Eventually, the estimated message $\hat{\vec{b}}$ should match the transmitted message $\vec{b}$ to yield a correct detection.

2.2 Wireless Channel

Time-variant impulse response. Once the complex baseband signal is transformed to analog domain and upconverted to the carrier frequency to yield

$$\underline{\vec{x}}(t) = (x_0(t), x_1(t), \ldots, x_{N_T-1}(t))^T,$$

it is sent via the transmit antennas over the air, where $x_i(t)$ denotes the signal from the ith transmit antenna. The signal propagates through the wireless channel and is distorted according to the channel characteristics. Eventually, the radio frequency (RF) signal

$$\underline{\vec{y}}(t) = (y_0(t), y_1(t), \ldots, y_{N_R-1}(t))^T$$

at the receive antennas is downconverted and discretized to yield the digital baseband signal. With a good approximation, the wireless channel between any pair of transmit antenna i_t and receive antenna i_r can be generally considered a linear system $\mathcal{H}_{i_r i_t}$ with additional additive white Gaussian noise (AWGN) due to thermal noise in the devices [TV05]. The signal $y_{i_r}(t)$ at the i_rth receive antenna then is the superposition of the transmit signals from all transmit antennas, given by

$$y_{i_r}(t) = \sum_{i_t=0}^{N_T-1} (\mathcal{H}_{i_r i_t} x_{i_t})(t) + w_{i_r}(t) \tag{2.1}$$

$$= \sum_{i_t=0}^{N_T-1} \int_{-\infty}^{\infty} h'_{i_r i_t}(t,\tau) x_{i_t}(t-\tau) d\tau + w_{i_r}(t), \tag{2.2}$$

where $h'_{i_r i_t}(t,\tau)$ denotes the time-variant impulse response of the channel from the i_tth transmit to the i_rth receive antenna and $w_{i_r}(t)$ denotes AWGN at the i_rth receive antenna.

Table 2.1: Power delay profiles of ETU and EVA channels. The dB values for the taps are relative to the strongest path in each channel.

EVA Channel									
l	0	1	2	3	4	5	6	7	8
τ_l [ns]	0	30	150	310	370	710	1090	1730	2510
σ_l^2 [dB]	0	-1.5	-1.4	-3.6	-0.6	-9.1	-7	-12	-16.9

ETU Channel									
l	0	1	2	3	4	5	6	7	8
τ_l [ns]	0	50	120	200	230	500	1600	2300	5000
σ_l^2 [dB]	-1.0	-1.0	-1.0	0	0	0	-3.0	-5.0	-7.0

Here, we have omitted rigorous mathematical derivations, as the channel model is not the focus of this thesis. A more detailed description, including the proof that (2.2) can model any linear channel, is given in e.g. [MBH13].

Rayleigh multipath fading. In this thesis, we particularly focus on the important model of the uncorrelated Rayleigh fading multipath channel. This model arises in a rich-scattering non-line of sight (NLOS) environment which is typical for e.g. urban areas [SA05]. In particular, we model the time-variant impulse response between any pair of transmit and receive antennas as a tapped delay line (TDL) by

$$h'_{i_r i_t}(t,\tau) = \sum_{l=0}^{N_L-1} a_{l,i_r i_t}(t)\delta(\tau - \tau_{l,i_r i_t}(t)), \tag{2.3}$$

where N_L denotes the number of paths in the multipath channel, $a_{l,i_r i_t}(t)$ is a stationary proper complex Gaussian random process describing amplitude and phase of the reflection from the lth path and $\tau_{l,i_r i_t}(t)$ denotes the delay of the lth path at time t. Further, we assume the delays $\tau_{l,i_r i_t}(t)$ to be constant for all times and antenna pairs [SA05] and the scatterers are uncorrelated, i.e.

$$E[a_{l,i_r i_t}(t) a_{l',i'_r i'_t}(t')] = r_{l,i_r i_t}(t-t')\delta_{ll'}\delta_{i_t i'_t}\delta_{i_r i'_r},$$

with δ_{jk} denoting the Kronecker delta. $r_{l,i_r i_t}(t-t')$ describes the temporal correlation of the reflection coefficient on the lth path, which is given by

$$r_{l,i_r i_t}(\Delta_t) = \sigma^2_{l,i_r i_t} J_0(2\pi\Delta_t f_D) \tag{2.4}$$

for Rayleigh fading [TV05]. Here, $\sigma^2_{l,i_r i_t}$ is the average power of the lth path and $J_0(x)$ is the 0th order Bessel function of the first kind [BS08]. Further, $f_D = \frac{v}{c} f_c$ is the maximum Doppler spread due to the relative speed v between transmitter and receiver and f_c is the carrier frequency. $c \approx 3 \cdot 10^8 \mathrm{ms}^{-2}$ denotes the wave propagation speed, which equals the speed of light in the medium.

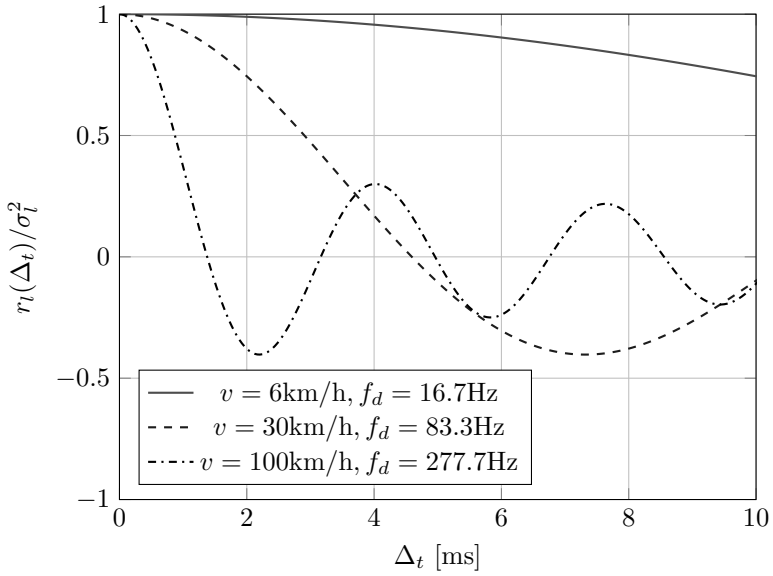

Figure 2.2: Example of temporal autocorrelation of a single tap in a Rayleigh multipath fading channel. The carrier frequency is set to $f_c = 3$GHz.

Power delay profile (PDP). We assume that $\sigma^2_{l,i_r i_t}$ is independent of the antenna pair i_r, i_t, and hence $\sigma^2_l = \sigma^2_{l,i_r i_t}$. Then, the set $\mathcal{P} = \{(\sigma^2_l, \tau_l)\}_{l=0,\ldots,L-1}$ describes the power delay profile (PDP) of the channel, i.e. it characterizes all available paths by their delay and average power. In common channel models, such as the 3GPP Extended typical urban (ETU) and Extended vehicular A (EVA) channels, the PDP is the main characteristic of a wireless channel. As an example, Tab. 2.1 shows the PDP of the 3GPP ETU and EVA channels. Depending on the number of paths in the PDP, different multipath diversity can be harvested in the channel. This multipath diversity directly translates to diversity in the frequency domain, hence longer channels exhibit a larger potential for frequency diversity.

Block fading. Figure 2.2 illustrates the temporal autocorrelation of $a_{l,i_r i_t}(t)$ depending on the relative velocity between transmitter and receiver according to (2.4). As can be seen, for pedestrian movement of 6km/h, the channel can be considered almost constant over at least 2ms. For higher velocities, the channel changes more rapidly, such that for $v = 100$km/h the tap coefficients are completely uncorrelated after already $\Delta_t \approx 1.4$ms.

The term *block-fading* amounts to a channel that changes signifantly slower than the signal duration of one code word (a *block*). In this case, the channel can be considered as a linear time-invariant system and can be approximated by $h'_{i_r i_t}(t, \tau) \approx h'_{i_r i_t}(\tau)$. Then, the channel input-output relation (2.2) simplifies to

$$y_{i_r}(t) = \sum_{i_t=0}^{N_T-1} \int_{-\infty}^{\infty} h'_{i_r i_t}(\tau) x_{i_t}(t-\tau) d\tau = \sum_{i_t=0}^{N_T-1} (h_{i_r i_t} * x_{i_t})(t). \tag{2.5}$$

Equivalent baseband discrete-time channel. Assuming ideal, linear RF devices in transmitter and receiver with no phase noise, IQ imbalance, DC offset etc., the effect of

analog to digital (AD) and digital to analog (DA) conversion and up/down-conversion can be incorporated into the channel impulse response to yield the overall impulse response $h_{i_r i_t}(t,\tau)$. Assuming the baseband sampling frequency equals F_s and the combined impulse response of AD and DA converters equals $u(t) = \mathrm{sinc}(F_s t) = \frac{\sin(\pi F_s t)}{\pi F_s t}$ [TV05], we have

$$h_{i_r i_t}(t,\tau) = \int_{-\infty}^{\infty} u(\tau') h'_{i_r i_t}(t, \tau - \tau') d\tau' = \sum_{l=0}^{N_L-1} a_{l,i_r i_t}(t) \mathrm{sinc}(\tau - \tau_l). \tag{2.6}$$

Then, the equivalent baseband channel impulse response can be modeled by

$$h_{i_r i_t}[n,n'] = h_{i_r i_t}(t,\tau)|_{t=\frac{n}{F_s},\tau=\frac{n'}{F_s}} = \sum_{l=0}^{L-1} a_{l,i_r i_t}\left(\frac{n}{F_s}\right) \mathrm{sinc}\left(\frac{n'}{F_s} - \tau_l\right), \tag{2.7}$$

and the overall digital baseband relation from all transmit signals $\underline{\vec{x}}[n]$ to all received signal $\underline{\vec{y}}[n]$ becomes linear with additional AWGN, given by

$$\underline{\vec{y}}[n] = \sum_{n' \in \mathbb{Z}} \underline{\mathbf{H}}[n,n'] \underline{\vec{x}}[n-n'] + \vec{w}[n], \tag{2.8}$$

where $\underline{\mathbf{H}}[n,n'] = (h_{i_r,i_t}[n,n'])_{i_r=0,\ldots,N_R-1,i_t=0,\ldots,N_T-1} \in \mathbb{C}^{N_R \times N_T}$ is the overall discrete MIMO channel matrix. Note that if $F_s \tau_l \in \mathbb{Z}$, (2.7) simplifies to

$$h_{i_r i_t}[n,n'] = \sum_{l=0}^{L-1} a_{l,i_r i_t}\left(\frac{n}{F_s}\right) \delta[n' - F_s \tau_l], \tag{2.9}$$

i.e. each reflecting path is mapped to a single coefficient in the discrete baseband model. Throughout this thesis, we have assumed this property to hold, by rounding $F_s \tau_l$ to the nearest integer.

Generic linear baseband model. Let us assume that the information for a given message is contained only in a continuous subset of N samples of $\underline{y}[n]$[1]. In this case, we can extract a finite part $\mathbf{y} \in \mathbb{C}^{N_R \times N}$ from $\underline{\vec{y}}[n]$ by $\mathbf{y} = (\underline{\vec{y}}[n])_{n=0,\ldots N-1}$ to process as a single block to estimate the transmitted message. Then, starting from the linear model (2.8) and assuming a linear modulation, i.e. $\underline{\vec{x}}[n]$ depends linearly on $\vec{d}$, we eventually reach the central linear system model

$$\mathrm{vec}(\mathbf{y}^T) = \vec{y} = \mathbf{H}\vec{d} + \vec{w} \tag{2.10}$$

which will be used throughout this thesis. Here, $\mathbf{H} \in \mathbb{C}^{N_R N \times L/\mu}$ is the equivalent channel matrix that jointly describes the transmit signal modulation, upconversion, wireless channel effects and downconversion and can be directly obtained from (2.8). We want to emphasize that (2.10) does not exclusively describe MIMO systems but any linear relation between transmitted data symbols and a received signal is covered. In particular, for non-orthogonal systems where interference cannot be removed by a unitary linear filter, $\mathbf{H}$ can become of considerable size.

[1] We assume non-interleaved, i.e. continuous transmission here. If symbol interleaving is used, the model still holds by increasing the considered signal length.

Relation to flat-fading MIMO channel. Commonly, in the literature, another linear MIMO model according to

$$\vec{y}[k] = \mathbf{C}[k]\vec{d}[k] + w[k] \tag{2.11}$$

is assumed, where $\mathbf{C}[k] \in \mathbb{C}^{N_R \times N_T}$ and k is a symbol index. In particular, this model holds for a flat-fading channel, where $\mathbf{H}$ in (2.10) consists of $N_R \times N_T$ diagonal blocks of size $N \times N$, which can be permuted to (2.11). For CP-OFDM we can obtain (2.11) from (2.10) under the assumption of multipath block-fading with sufficient CP length and k denotes the subcarrier index. Then, (2.10) can be unitarily transformed to (2.11), by noting that

$$\vec{Y} = (\mathbf{I}_{N_R} \otimes \mathbf{F}_N)\vec{y} = (\mathbf{I}_{N_R} \otimes \mathbf{F}_N)\mathbf{H}\vec{d} + (\mathbf{I}_{N_R} \otimes \mathbf{F}_N)\vec{w}$$

becomes a system of $N_R \times N_T$ diagonal blocks of size $N \times N$ and the noise statistics remain equal.[2]

2.3 Generic MIMO Receiver

Given the signal model for the received signal $\vec{y}$

$$\vec{y} = \mathbf{H}\vec{d} + \vec{w}, \tag{2.12}$$

the task of the receiver is to estimate the transmitted message $\vec{b}$, or equivalently $\vec{b}_c$, from $\vec{y}$. The optimal estimate $\hat{b}_{c,ML}$ in the maximum a-posteriori (MAP) sense is given by[3]

$$\hat{b}_{c,\mathrm{MAP}} = \arg\max_{\vec{b}_c \in \mathcal{C}} Pr(\vec{b}_c|\vec{y}, \mathbf{H}), \tag{2.13}$$

where $\mathcal{C} \subset \mathbb{B}^L$ denotes the set of all possible codewords and $Pr(\vec{b}_c|\vec{y}, \mathbf{H})$ denotes the probability that the message was $\vec{b}_c$ given the observations $\mathbf{H}$ and $\vec{y}$. By using Bayes theorem[BS08] this can be reformulated to

$$\hat{b}_{c,\mathrm{MAP}} = \arg\max_{\vec{b}_c \in \mathcal{C}} Pr(\vec{y}|\vec{b}_c, \mathbf{H}) \frac{Pr(\vec{b}_c)}{Pr(\vec{y})}. \tag{2.14}$$

Under the common assumption that all codewords $\vec{b}_c$ are equally likely and hence $Pr(\vec{b}_c) = \frac{1}{|\mathcal{C}|}$, the MAP criterion reduces to the maximum likelihood (ML) criterion given by

$$\hat{b}_{c,\mathrm{ML}} = \arg\max_{\vec{b}_c \in \mathcal{C}} Pr(\vec{y}|\vec{b}_c, \mathbf{H}), \tag{2.15}$$

which is a criterion commonly applied by optimal MIMO detectors. In case $\vec{w}$ is AWGN, the ML criterion reduces to the minimization of the Euclidean distance [BC12] by

$$\hat{b}_{c,\mathrm{ML}} = \arg\min_{\vec{b}_c \in \mathcal{C}} \|\vec{y} - \mathbf{H}\vec{d}\|^2 = \arg\min_{\vec{b}_c \in \mathcal{C}} \|\vec{y} - \mathbf{H}\vec{\mathcal{M}}(\vec{b}_c)\|^2. \tag{2.16}$$

[2] Note that the inverse discrete Fourier transform (IDFT) at the CP-OFDM transmitter is already contained in $\mathbf{H}$ in the obeyed notation, i.e. $\mathbf{H} = \tilde{\mathbf{H}}(\mathbf{I}_{N_T} \otimes \mathbf{F}_N^H)$ where $\tilde{\mathbf{H}}$ contains $N_R \times N_T$ circulant blocks of size $N \times N$

[3] Here, optimum refers to minimizing the expected codeword error rate after detection.

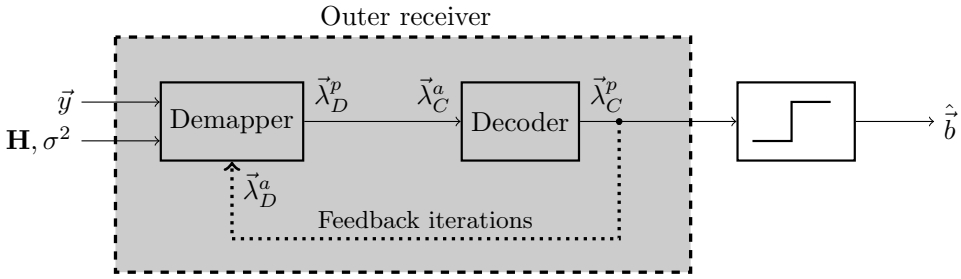

Figure 2.3: Separation of the outer receiver into a demapper and decoder block. The demapper transforms the received signal into LLRs for each bit, considering only the constellation constraint. Subsequently, the decoder improves the estimate by including the code constraint into the detection process. Eventually, the demapper can use the information from the decoder via a feedback loop, yielding an iterative receiver structure. Note that this generic diagram does not consider the difference between extrinsic and intrinsic information and assumes that these are calculated within the demapper and decoder blocks.

Implied by the fact that longer codewords in general yield better receiver performance [RL09], $\mathcal{C}$ does not allow exhaustive search as in (2.16) since $|\mathcal{C}|$ grows exponentially with the code word length. Hence, alternative solutions must be pursued and approximations are inevitable.

Constellation and code constraint. In particular, the outer receiver has the knowledge that the transmitted signal $\vec{x} = \mathbf{H}\vec{d}$ obeys two constraints: First, the transmitted constellation symbols $\vec{d}$ are a discrete subset of $\mathbb{C}^{L/\mu}$, hence only discrete values for $\vec{d}$ are admissable. This constraint is termed *constellation constraint*. Second, only bit combinations that are valid codewords can be transmitted, further reducing the amount of possible $\vec{d}$. We term this second constraint the *code constraint*. Treating each constraint separately, the operation in the outer receiver is commonly split into two steps, which are performed by the *demapper* and *decoder* blocks, respectively, as is outlined in Fig. 2.3.

The demapper. The demapper ignores the code constraint and exclusively considers the constellation constraint of the transmitted signal. Therefore, it considers the model

$$\vec{y} = \mathbf{H}\vec{d} + \vec{w} \tag{2.17}$$

to yield an estimate of the transmitted QAM symbols, or equivalently it estimates the probability for each element in $\vec{b}_c$ to be 0 or 1. The information $\lambda_{i,b}^p$ describes the probability of the bth bit of the ith element of $\vec{d}$ is conveniently expressed in terms of the log-likelihood ratio (LLR) and given by

$$\lambda_{i,b}^p = \log\left(\frac{Pr(b_{i,b} = 1|\vec{y}, \mathbf{H})}{Pr(b_{i,b} = 0|\vec{y}, \mathbf{H})}\right), \tag{2.18}$$

where the superscript $(\cdot)^p$ denotes a-posterori information, i.e. information gained from the demapping operation. Using Bayes's theorem [BS08], we can write (2.18) as

$$\lambda_{i,b}^p = \log\left(\sum_{\vec{d}\in\mathcal{D}_{i,b}^{(1)}} p(\vec{y}|\vec{d}, \mathbf{H})P(\vec{d})\right) - \log\left(\sum_{\vec{d}\in\mathcal{D}_{i,b}^{(0)}} p(\vec{y}|\vec{d}, \mathbf{H})P(\vec{d})\right), \tag{2.19}$$

where $\mathcal{D}_{i,b}^{(1)}, \mathcal{D}_{i,b}^{(0)}$ are the sets of all constellation vectors $\vec{d}$ where the bth bit of the ith symbols is 1 or 0, respectively. $p(\vec{y}|\vec{d}, \mathbf{H})$ denotes the probability density function (PDF) of $\vec{y}$ conditioned on the transmitted data and channel observation and is a Gaussian PDF centered at $\mathbf{H}\vec{d}$ with covariance matrix $\sigma^2\mathbf{I}$. $P(\vec{d})$ contains a-priori information about the probability of each constellation vector. This information can for example be obtained from decdor feedback in an iterative receiver structure (cf. Sec. 6). Alternatively, a uniform distribution of $\vec{d}$ is assumed.

The channel decoder. In a second step, the channel decoder combines the constraint implied by the channel code with the information gathered from the demapper to yield an improved estimate of the transmitted codeword. Depending on the type of applied channel code, different decoding algorithms exist, such as Viterbi or Bahl-Cocke-Jelinek-Raviv (BCJR) decoding for convolutional codes (CCs) or the sum product algorithm (SPA) for low-density parity check (LDPC) channel codes [RL09]. The design of channel decoding algorithm is an important field in communication research, but beyond the scope of this work. Instead, we adopt available channel decoders from the literature (see e.g. [RL09]).

Linear Soft-out MIMO demapping. An important class soft-out demappers are linear demappers that perform a linear equalization of $\vec{y}$ expressed by the matrix $\mathbf{W}$ to get the estimate $\hat{d}$ given by

$$\hat{d} = \mathbf{W}\vec{y} = \mathbf{W}\mathbf{H}\vec{d} + \mathbf{W}\vec{w} \tag{2.20}$$

$$= \mathbf{\Delta}\vec{d} + \underbrace{(\mathbf{W}\mathbf{H} - \mathbf{\Delta})\vec{d} + \mathbf{W}\vec{w}}_{\tilde{w}}, \tag{2.21}$$

where $\mathbf{\Delta} = \mathrm{diag}(\mathbf{W}\mathbf{H})$. The equalizer $\mathbf{W}$ can e.g. be defined by the linear minimum mean squared error (LMMSE) or zero-forcing (ZF) criterion [Kay93] such that $\mathbf{W}\mathbf{H}$ is (approximately) diagonal. The residual term $(\mathbf{W}\mathbf{H}-\mathbf{\Delta})\vec{d}$ amounts to self-interference after the equalization and the noise term $\mathbf{W}\vec{w}$ becomes colored, if $\mathbf{W}$ is not unitary. When $\mathbf{W}$ is a full-rank matrix, (2.20) is a sufficient statistic for (2.17), hence $\hat{d}$ and $\vec{y}$ contain the same information about $\vec{d}$. However, the suboptimality of linear receivers arises from modeling the error terms $\tilde{w}_i, \tilde{w}_j$ on two different elements i, j of $\hat{d}$ as uncorrelated Gaussian random variables with zero mean. In this case the noise correlation is ignored which leads to a loss of information. On the other hand, then (2.20) reduces to decoupled scalar equations

$$\hat{d}_i = \mathbf{\Delta}_{i,i} d_i + \tilde{w}_i \qquad \text{for} \qquad i = 0, \ldots, L/\mu, \tag{2.22}$$

with

$$(\sigma^2_{\tilde{w}_i})_{i=0,\ldots,L/q} = \mathrm{diag}(E[\tilde{w}\tilde{w}^H]) = \mathrm{diag}((\mathbf{W}\mathbf{H} - \mathbf{\Delta})(\mathbf{W}\mathbf{H} - \mathbf{\Delta})^H + \sigma^2\mathbf{I}) \tag{2.23}$$

modeling the variance of post-equalization error term $\tilde{w}$. This way, each data symbol d_i can be detected separately, which significantly reduces complexity. Accordingly, the

post-equalization LLR $\lambda_{i,b}^{p}$ for the bth bit in the ith constellation symbol are given by

$$\begin{aligned}\lambda_{i,b}^{p} = &\log\left(\sum_{a\in\mathcal{S}_b^{(1)}} \exp\left(-\frac{\|\hat{d}_i - \mathbf{\Delta}_{i,i}a\|^2}{\sigma_{\tilde{w}_i}^2} + \log P(\vec{d}_i = a)\right)\right) \\ &- \log\left(\sum_{a\in\mathcal{S}_b^{(0)}} \exp\left(-\frac{\|\hat{d}_i - \mathbf{\Delta}_{i,i}a\|^2}{\sigma_{\tilde{w}_i}^2} + \log P(\vec{d}_i = a)\right)\right),\end{aligned} \tag{2.24}$$

where $\mathcal{S}_b^{(1)}, \mathcal{S}_b^{(0)} \subset \mathcal{S}$ are the set of constellation symbols where the bth bit is 1 or 0, respectively. Employing the max-log approximation [RL09] $\log(\exp(a) + \exp(b)) \approx \max(a, b)$ this expression is simplified to

$$\begin{aligned}\lambda_{i,b}^{p} \approx &\min_{a\in\mathcal{S}_b^{(0)}} \left\{\frac{\|\hat{d}_i - \mathbf{\Delta}_{i,i}a\|^2}{\sigma_{\tilde{w}_i}^2} + \log P(\hat{d}_i = a)\right\} \\ &- \min_{a\in\mathcal{S}_b^{(1)}} \left\{\frac{\|\hat{d}_i - \mathbf{\Delta}_{i,i}a\|^2}{\sigma_{\tilde{w}_i}^2} + \log P(\hat{d}_i = a)\right\}.\end{aligned} \tag{2.25}$$

2.4 GFDM Fundamentals

GFDM is a block-based multicarrier system [MMG+14]. Similar to OFDM, consecutive GFDM blocks can be separated by a CP [TV05], mitigating inter-block interference (IBI) such that each block can be processed separately at the receiver side. In contrast to OFDM, where subsequent symbols are separated by a CP, in GFDM M subsymbols are concatenated to form one GFDM block. Let T_S denote the time distance between adjacent subsymbols, then, similar to OFDM, the frequency spacing F between subcarriers is given by $F = 1/T_S$.

Figure 2.4 presents an overview of the GFDM block structure. Within one GFDM block of total bandwidth F_s, there are M subsymbols, spaced by T_S and $K = F_s T_S$ subcarriers, spaced by $F = {}^{1}/_{T_S}$. On each subcarrier k within each subsymbol m, a complex-valued data symbol $d_{k,m}$ is transmitted and the entire block is protected by a single CP. In the following, we will first relate the introduced GFDM parameters to well-known OFDM system parameters and subsequently describe the GFDM modulation and conventional linear detection in detail.

2.4.1 GFDM Parameters

For a given sampling frequency F_s, in relation to OFDM we can identify two characteristic GFDM configurations, Type I and Type II, which are illustrated in Fig. 2.5. We assume the CP to be of equal length for GFDM and OFDM, as its length is constrained by the channel's PDP. In relation to the generic OFDM system with symbol duration T_O (which corresponds to $U = F_s T_O$ samples), CP duration T_{CP} and subcarrier spacing $F_O = 1/T_O$, GFDM Type I employs a subsymbol spacing equal to the OFDM symbol duration $T_{S,I} =$

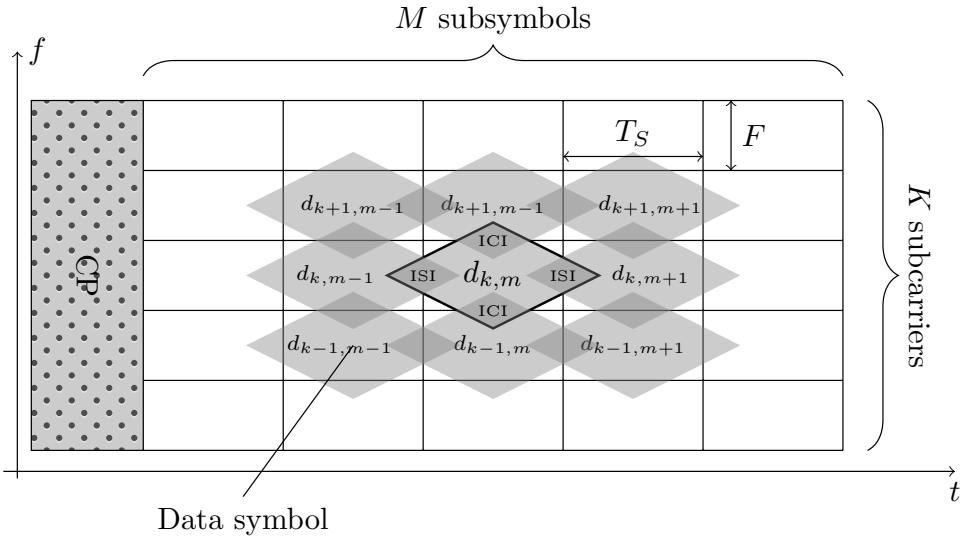

Figure 2.4: GFDM Block structure overview.

T_O and according subcarrier spacing $F_I = F_O$. Since M subsymbols are concatenated into one block, with the GFDM Type I configuration the duration of the GFDM block is larger than a corresponding OFDM block and a better spectral confinement than OFDM can be achieved [MMGF14]. At the same time, since multiple subsymbols share a single CP, the spectral efficiency $r_{G,I}$ of GFDM Type I is larger than that of the corresponding OFDM system r_O. Assuming equal modulation and coding scheme (MCS), pilot overhead and signal bandwidth, the gain can be quantified by

$$\frac{r_{G,I}}{r_O} = \frac{\frac{MT_O}{MT_O+T_{CP}}}{\frac{T_O}{T_O+T_{CP}}} = 1 + \frac{(M-1)T_{CP}}{MT_O + T_{CP}} \xrightarrow{M\to\infty} 1 + \frac{T_{CP}}{T_O}. \tag{2.26}$$

The gain increases with more subsymbols M and is limited by the ratio of the CP duration to the symbol duration, which exactly equals the rate loss due to the CP of OFDM. Hence, theoretically GFDM type I could mitigate the rate loss of the CP of OFDM. However, the wireless channel is required to be static for an entire GFDM block, which limits the amount of applicable subsymbols in practice due to time-varying channels.

In the GFDM Type II configuration, we keep the GFDM block duration equal to the OFDM symbol duration and hence reduce the distance between the subsymbols to $T_{S,II} = T_O/M$. Accordingly, the subcarrier spacing of the system increases to $F_{II} = MF_O$ and the spectral efficiency of GFDM Type II and OFDM remains equal. Here, the wider subcarrier spacing of GFDM compared to OFDM can yield more robustness against residual carrier frequency offset or time-variant channels that exhibit Doppler spread [ZMMF17]. Furthermore, wider subcarriers can potentially harvest more frequency diversity in case of frequency selective channels [MGZF15]. On the other hand, without further means to reduce OOB emission such as windowing [MMG+14], the spectral properties of GFDM Type-II and OFDM become equal.

Table 2.2 shows the relation between the parameters of OFDM and its corresponding GFDM Type I and Type II configurations. Additionally, relations to physical parameters are provided. We start from systems that all have the same bandwith or sampling

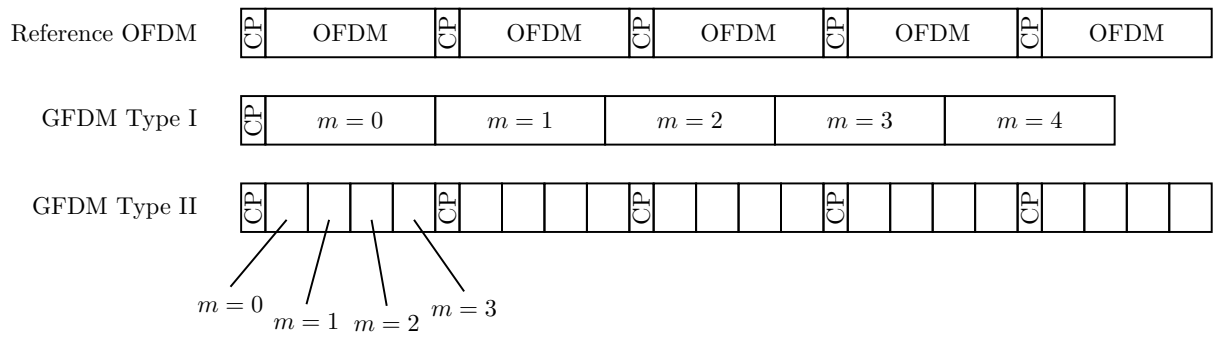

Figure 2.5: Block structure of type I and II GFDM configurations in relation to a reference OFDM system.

Table 2.2: Relation of OFDM and GFDM Type I, Type II parameters and corresponding physical parameters.

Physical Parameter	OFDM	GFDM-I	GFDM-II	Unit
Bandwidth	F_s	F_s	F_s	Hz
Subsymbol duration	T_O	T_O	T_O/M	s
	$U = F_s T_O$	U	U/M	samples
# Subsymbols	1	M	M	-
Block duration	$T_O + T_{CP}$	$MT_O + T_{CP}$	$T_O + T_{CP}$	s
	$U + N_{CP}$	$MU + N_{CP}$	$U + N_{CP}$	samples
Subcarrier spacing	$1/T_O$	$1/T_O$	M/T_O	Hz
# Subcarriers	U	U	U/M	-
GFDM Parameter				
# Subsymbols M		M	M	
# Subcarriers K		U	U/M	
Block length N		MU	U	

frequency of F_s and define the parameters for GFDM Type I and Type II in terms of the corresponding values of OFDM. Additionally, we present the symbol spacing and and block duration in terms of number of samples, corresponding to the sampling frequency F_s.

2.4.2 GFDM Modulation

In this section we describe the structure of the GFDM transmit signal and introduce representations of the transmit equation which are suitable for the subsequent analysis throughout this thesis.

Modulation equation. Let us consider a GFDM system in the discrete time domain, consisting of K subcarriers and M subsymbols, that are equally spaced in time and

frequency. We arrange the data in the data matrix $\mathbf{D}$, given by

$$\mathbf{D} = \begin{pmatrix} d_{0,0} & d_{0,1} & \dots & d_{0,M-1} \\ d_{1,0} & d_{1,1} & \dots & d_{1,M-1} \\ \vdots & \vdots & \ddots & \vdots \\ d_{K-1,0} & d_{K-1,1} & \dots & d_{K-1,M-1} \end{pmatrix}, \tag{2.27}$$

where $d_{k,m}$ denotes the complex-valued constellation symbol that is transmitted on the kth subcarrier and mth subsymbol. Obeying critical sampling, the number of samples N in the time domain required to convey the information of one GFDM block equals $N = KM$. Let $g[n]$, $n = 0, \dots, N-1$ be any time-domain sequence of N samples, denoted as the *prototype filter*. Then, the transmit signal $x[n]$ of one GFDM block, excluding the CP, is given by

$$x[n] = \sum_{m=0}^{M-1} \sum_{k \in \mathcal{K}} d_{k,m} g_{k,m}[n], \quad n = 0, 1, \dots, N-1 \tag{2.28}$$

$$\text{with } g_{k,m}[n] = g[\langle n - mK \rangle_N] \exp\left(j2\pi \frac{nk}{K}\right), \tag{2.29}$$

where $\mathcal{K} \subseteq \{0, 1, \dots, K-1\}$ is the set of switched-on subcarriers and we denote $K_{on} = |\mathcal{K}|$ as the number of switched-on subcarriers.

The sequence $g_{k,m}[n]$ is the prototype filter circularly shifted in time and frequency. The shift in frequency becomes apparent when looking at the N-point discrete Fourier transform (DFT) of $g_{k,m}[n]$, given by

$$\text{DFT}_N\{g_{k,m}[n]\} = G_{k,m}[\nu] = G[\langle \nu - kM \rangle_N] \exp(-j2\pi \frac{m\nu}{M}), \nu = 0, \dots, N-1. \tag{2.30}$$

The index m, denoting the subsymbol index, circularly shifts the prototype filter by mK samples in the time domain. Accordingly, the subcarrier index k circularly shifts the prototype filter by $kM = kN/K$ samples in the DFT domain.

For the subsequent analysis of applying MIMO techniques to the GFDM system, two particular representations of the modulation equation (2.28) are useful, which we will describe in the following. Firstly, observing that (2.28) is a linear combination of $g_{k,m}[n]$ with coefficients $d_{k,m}$ we can express the modulation conveniently as a matrix multiplication [MKLF12]. Let us denote

$$\vec{x} = (x[n])_{n=0,\dots,N-1} \qquad \in \mathbb{C}^N, \tag{2.31}$$

$$\vec{d}_k = (d_{k,0}, d_{k,1}, \dots, d_{k,M-1})^T \qquad \in \mathbb{C}^M, \tag{2.32}$$

$$\vec{d} = (\vec{d}_0^T, \vec{d}_1^T, \dots, \vec{d}_{K-1}^T)^T = \text{vec}(\mathbf{D}^T) \qquad \in \mathbb{C}^N, \tag{2.33}$$

where $\vec{x}$ is the vector of the samples of the transmit signal, $\vec{d}_k$ contains the data on the kth subcarrier and $\vec{d}$ denotes the entire data in the GFDM block[4]. Then, we can define

[4] Note that, in contrast to most literature, here we define the ordering to be grouped by subcarriers rather than subsymbols. This treatment readily provides us a banded structure of the modulation matrix in the frequency domain, given $g[n]$ is band-limited.

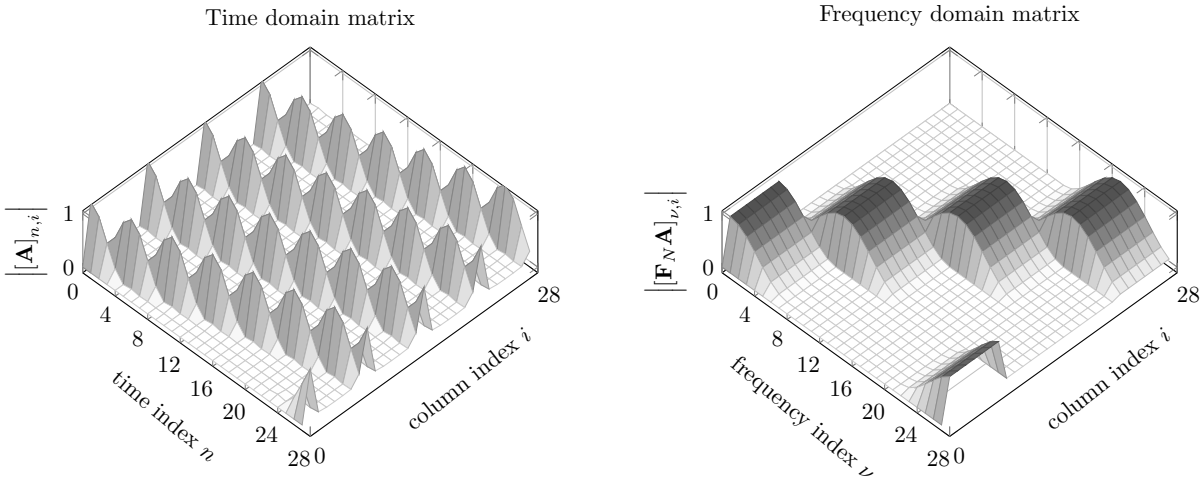

Figure 2.6: Depiction of $\mathbf{A}$ in time and frequency domain for $M = 7, K = 4$ using a RC filter with $\alpha = 1$. One can clearly see the banded structure of $\mathbf{A}$ in the frequency domain, since $G[\nu]$ is band-limited. In the time domain, adjacent columns of $\mathbf{A}$ correspond to different subsymbols, therefore the peaks on each column appear at different times. It is notable that in the time domain the colums of $\mathbf{A}$ cannot be permuted to yield a band-diagonal matrix, since $g[n]$ is not time-limited.

the transmit signal by

$$\vec{x} = \mathbf{A}\vec{d}, \tag{2.34}$$

where $\mathbf{A} = (\vec{g}_{0,0}, \vec{g}_{0,1}, \vec{g}_{0,2}, \ldots, \vec{g}_{1,0}, \vec{g}_{1,1}, \ldots, \vec{g}_{K-1,M-1})$ for $K_{on} = K$ with $\vec{g}_{k,m} = (g_{k,m}[n])_{n=0,\ldots,N-1}$. Hence, the $m + kM$th column of $\mathbf{A}$ is given by $\vec{g}_{k,m}$. In case $K_{on} < K$, $\mathbf{A}$ only contains $\vec{g}_{k,m}$ for switched-on subcarriers and $\mathbf{A}$ has dimensions $N \times K_{on}M$. Fig. 2.6 illustrates the structure of $\mathbf{A}$ in time- and frequency domain.

Secondly, let us examine the structure of the N-point DFT of the transmit signal [GNN+13, MGK+12]:

$$X[\nu] = \mathrm{DFT}_N\{x[n]\} = \sum_{k=0}^{K-1}\sum_{m=0}^{M-1} d_{k,m}G_{k,m}[\nu] \tag{2.35}$$

$$= \sum_{k=0}^{K-1}\sum_{m=0}^{M-1} d_{k,m}G[\langle \nu - kM\rangle_N]\exp(-j2\pi\frac{\nu m}{M}) \tag{2.36}$$

$$= \sum_{k=0}^{K-1} G[\langle \nu - kM\rangle_N]\underbrace{\sum_{m=0}^{M-1} d_{k,m}\exp(-j2\pi\frac{\nu m}{M})}_{\mathrm{DFT}_M\{d_{k,(\cdot)}\}}[\nu] \tag{2.37}$$

Naturally, the transmit signal in the frequency domain is the linear combination of all time and frequency shifted filter responses $G_{k,m}[\nu]$. More remarkably, the modulation can be separated into an M-point DFT of all subsymbols on each subcarrier, $\mathrm{DFT}_M\{d_{k,(\cdot)}\}$, with subsequent freqency domain windowing with $G[\langle \nu - kM\rangle_N]$. Note that since $\mathrm{DFT}_M\{d_{k,(\cdot)}\}$ is periodic with period M, $\mathrm{DFT}_M\{d_{k,(\cdot)}\}[\nu], \nu = 0, \ldots, N-1$ is a K-times repetition of $\mathrm{DFT}_M\{d_{k,(\cdot)}\}[\nu], \nu = 0, \ldots, M-1$. Hence, if the filter $G[\nu]$ has more than M non-zero

elements, adjacent subcarriers overlap. On the one hand, this introduces inter-carrier interference (ICI). On the other hand, at the same time data on one subcarrier is spread onto several frequency bins, raising potential for enhanced frequency diversity in multipath channels, which can improve the obtained diversity of a subsequent channel code. Before transmitting the signal over the wireless channel, a CP is added to each block.

Derivation of the discrete baseband prototype filter. The normalized and periodic pulse shaping prototype filter $g[n]$ for GFDM[5] is commonly derived from a continuous-time filter $g(t)$ by sampling in the time and frequency domain. Let $g(t)$ be any continuous-time filter and F_s be the sampling frequency and hence bandwidth of the discrete baseband system. Then, we first sample $g(t)$ in the time domain to get $\tilde{g}[n]$ given by

$$\tilde{g}[n] = \frac{1}{F_s} g\left(\frac{n}{F_s}\right) \tag{2.38}$$

which has a continuous, periodic spectrum $\tilde{G}(f)$ with $\tilde{G}(f) = \tilde{G}(f + kF_s), k \in \mathbb{Z}$. Subsequently, we sample one period of $\tilde{G}(f)$ with N samples in the frequency domain to get the spectrum of the discrete prototype filter $G[\nu]$ given by

$$G[\nu] = \tilde{G}\left(\frac{\nu}{N} F_s\right), \quad \nu = 0, 1, \ldots, N-1. \tag{2.39}$$

Here, $G[\nu]$ yields the discrete baseband spectrum of the prototype filter and hence the time-domain response of the filter is given by

$$g[n] = \mathrm{IDFT}_N\{G[\nu]\}. \tag{2.40}$$

Note that due to sampling in the frequency domain, $g[n]$ is also periodic with period N, i.e. $g[n+lN] = g[n], l \in \mathbb{Z}$. Hence, understanding GFDM filtering as a circular convolution as in [MKLF12] as well as the definition of $g_{k,m}[n] = g[\langle n - mK \rangle_N] \exp(j2\pi \frac{kn}{K})$ appears natural.

For example, the discrete baseband periodic raised cosine (RC) filter $g[n]$ for GFDM which is used throughout this thesis is derived from the continuous-time RC filter given by

$$g(t) = \frac{1}{T} \mathrm{sinc}\left(\frac{t}{T}\right) \frac{\cos\left(\frac{\pi \alpha t}{T}\right)}{1 - \left(\frac{2\alpha t}{T}\right)^2}, \tag{2.41}$$

with $\mathrm{sinc}(x) = \sin(\pi x)/(\pi x)$, $T = \frac{K}{F_s}$ and $\alpha \in [0, 1]$ is the rolloff factor.

2.4.3 Linear GFDM Demodulation

Consider a single-antenna point-to-point link. Assuming the CP is longer than the channel impulse response (CIR) and the channel remains static over the duration of one GFDM

[5] Here, the normalization constraint is given by $\sum_{n=0}^{N-1} |g[n]|^2 = 1$.

block, i.e. block-fading is considered, after removing the CP at the receiver [TV05], the received signal $\vec{y} \in \mathbb{C}^N$ for one GFDM block can be written as

$$\vec{y} = \tilde{\mathbf{H}}\mathbf{A}\vec{d} + \vec{w}, \tag{2.42}$$

where $\tilde{\mathbf{H}} \in \mathbb{C}^{N\times N}$ is the circulant channel matrix with the CIR in its first column and $\vec{w}$ is AWGN of complex normal distribution $\vec{w} \sim \mathcal{CN}(0, \sigma^2\mathbf{I})$ at the receiver antenna. Assuming $E[\vec{d}\vec{d}^H] = \mathbf{I}$, with the linear model (2.42), we can immediately identify three basic linear receivers [MKLF12], namely matched filter (MF)[6] , ZF and LMMSE receivers. Their characteristics for soft-demapping according to (2.24) are given by

$$\begin{aligned}
\text{MF receiver}^5\text{: } \hat{d} &= \mathbf{A}^H\tilde{\mathbf{H}}^{-1}\vec{y} \\
\text{diag}(\mathbf{\Delta}) &= \vec{1} \qquad (2.43)\\
\mathbf{R}_{\tilde{w}} &= (\mathbf{A}^H\mathbf{A} - \mathbf{I})(\mathbf{A}^H\mathbf{A} - \mathbf{I})^H + \sigma^2\mathbf{A}^H\tilde{\mathbf{H}}^{-1}\tilde{\mathbf{H}}^{-H}\mathbf{A} \\
\text{ZF receiver: } \hat{d} &= \mathbf{A}^{-1}\tilde{\mathbf{H}}^{-1}\vec{y} \\
\text{diag}(\mathbf{\Delta}) &= \vec{1} \qquad (2.44)\\
\mathbf{R}_{\tilde{w}} &= \sigma^2\mathbf{A}^{-1}\tilde{\mathbf{H}}^{-1}\tilde{\mathbf{H}}^{-H}\mathbf{A}^{-H} \\
\text{LMMSE receiver: } \hat{d} &= \mathbf{A}^H\tilde{\mathbf{H}}^H(\tilde{\mathbf{H}}\mathbf{A}\mathbf{A}^H\tilde{\mathbf{H}}^H + \sigma^2\mathbf{I})^{-1}\vec{y} \\
\text{diag}(\mathbf{\Delta}) &= \text{diag}(\mathbf{A}^H\tilde{\mathbf{H}}^H(\tilde{\mathbf{H}}\mathbf{A}\mathbf{A}^H\tilde{\mathbf{H}}^H + \sigma^2\mathbf{I})^{-1}\tilde{\mathbf{H}}\mathbf{A}) \qquad (2.45)\\
\mathbf{R}_{\tilde{w}} &= \mathbf{I} - \mathbf{A}^H\tilde{\mathbf{H}}^H(\tilde{\mathbf{H}}\mathbf{A}\mathbf{A}^H\tilde{\mathbf{H}}^H + \sigma^2\mathbf{I})^{-1}\tilde{\mathbf{H}}\mathbf{A},
\end{aligned}$$

where we have used the notation from Sec. 2.3.

For the uncoded case, closed-form solutions for the symbol error rate (SER) of GFDM for ZF and MF receivers in different channel models are derived in [MMGF14, MMG+14, MMG+15]. In particular, due to self-interference of the MF receiver, an error floor is obtained for higher modulation orders. For the ZF receiver, a constant shift of the SER curves compared to an orthogonal system is experienced, due to noise enhancement during equalization. Specifically, the noise enhancement factor (NEF) ξ for the GFDM ZF receiver is given by [NMZF17, MMG+14]

$$\xi = \frac{1}{N}\text{tr}(\mathbf{A}^{-1}\mathbf{A}^{-H}). \tag{2.46}$$

For the LMMSE receiver, a tradeoff between self-interference and noise-enhancement is exploited, leading to improved performance compared to the ZF receiver. More details on these basic linear receivers are given in e.g. [MMG+14, MKLF12].

Low-complexity LMMSE estimation with banded linear systems. Throughout this work, LMMSE estimation with a band-diagonal linear model plays a central role. Consider a generic linear model

$$\vec{y} = \mathbf{H}\vec{d} + \vec{w} \tag{2.47}$$

[6] Note that we employ ZF equalization here before MF GFDM filtering

with a-priori knowledge of $\vec{w} \sim \mathcal{CN}(0, \sigma^2\mathbf{I})$ and $\vec{d} \sim \mathcal{CN}(\vec{d}^a, \Lambda_d^a)$ where Λ_d^a is diagonal. As we have shown in [MZF16a], the LMMSE estimate of mean $\hat{\vec{d}}^p$ and variance Λ_d^p of $\vec{d}$ can be formulated as

$$\hat{\vec{d}}^p = \mathbf{X}^{-1}(\mathbf{H}^H\vec{y} - \mathbf{G}\vec{d}^a) + \vec{\mu} \circ \vec{d}^a \tag{2.48}$$

$$\mathrm{diag}(\Lambda_d^p) = \vec{\mu} - \Lambda_d^a\vec{\mu} \circ \vec{\mu}, \tag{2.49}$$

with

$$\vec{\mu} = \mathrm{diag}(\mathbf{X}^{-1}\mathbf{G}), \qquad \mathbf{X} = \mathbf{G}\Lambda_d^a + \sigma^2\mathbf{I}, \qquad \mathbf{G} = \mathbf{H}^H\mathbf{H}. \tag{2.50}$$

If $\mathbf{G}$ is a band-diagonal matrix of size $N \times N$ with one-sided bandwidth M, $\mathbf{X}$ obeys the same structure and the complexity required to solve (2.48) grows linearly in N and quadratic in M [(NA, Functions *zgbtrf, zgbtrs*]. However, the arithmetic complexity for directly calculating $\vec{\mu}$ as in (2.50) would grow quadratically in N, which is undesirable. Instead, $\vec{\mu}$ can be estimated from $\mathcal{X} = \mathbf{X}^{-1}(\mathbf{GV})$, where $\mathbf{V}$ is an arbitrary real matrix [BKS07] with preferably less columns than $\mathbf{G}$. An estimate of $\vec{\mu}$ is given by

$$\hat{\vec{\mu}} = [(\mathbf{V} \circ \mathcal{X})\vec{1}] \oslash [(\mathbf{V} \circ \mathbf{V})\vec{1}]. \tag{2.51}$$

The accuracy of the estimation depends on both the structure of $\mathbf{V}$ and $\mathbf{X}^{-1}\mathbf{G}$. The estimation in (2.51) is exact, if the off-diagonal elements of $\mathbf{VV}^T$ are zero where $\mathbf{X}^{-1}\mathbf{G}$ is non-zero. Optimally, $\mathbf{V} = \mathbf{I}$, however in this case the inverse is implicitely calculated, leading to no reduction in complexity. Instead, noting that both $\mathbf{X}$ and $\mathbf{G}$ are band-diagonal, we can assume that $\mathbf{X}^{-1}\mathbf{G}$ is mostly concentrated within the bandwidth $2M$. We can hence design a matrix $\mathbf{V}$ which is zero inside the bandwidth $2M$. As is shown in [MZF16a], submatrices of Hadamard matrices with $2M$ columns fulfill this property, and hence the arithmetic complexity of $\vec{\mu}$ in (2.51) scales linearly with the bandwidth of $\mathbf{X}$ and not with its dimension, leading to an overall complexity that scales linearly with N and quadratic with M. A more detailed derivation including results on accuracy of this approximation and exact arithmetic complexities are given in our work [MZF16a].

Detection performance. Figure 2.7 compares the uncoded SER and coded frame error rate (FER) performance for the three receivers with an example single-antenna GFDM configuration under block-fading multipath channels employing a rate $1/2$ standard $(1, 15/13)_8$ Turbo code [RL09] with 16-QAM modulation. Here, we consider a single-antenna system to present the effect of the different linear receivers in absence of additional inter-antenna interference (IAI). In the following chapters, we will exclusively focus on MIMO-GFDM systems. For comparison, Figure 2.7 additionally shows a reference curve of OFDM . At first glance, the linear MF receiver shows inferior performance for coded and uncoded transmission due to the strong self-interference which is just treated as additional noise in the receiver. Apparently, as has been also shown in [MMGF14, MKLF12], the self-interference increases with increasing rolloff and performance degrades. Therefore, also a similar behaviour is observed with ZF and LMMSE receivers, whereas the influence of the rolloff factor is not as pronounced. For the LMMSE receiver, the degradation due

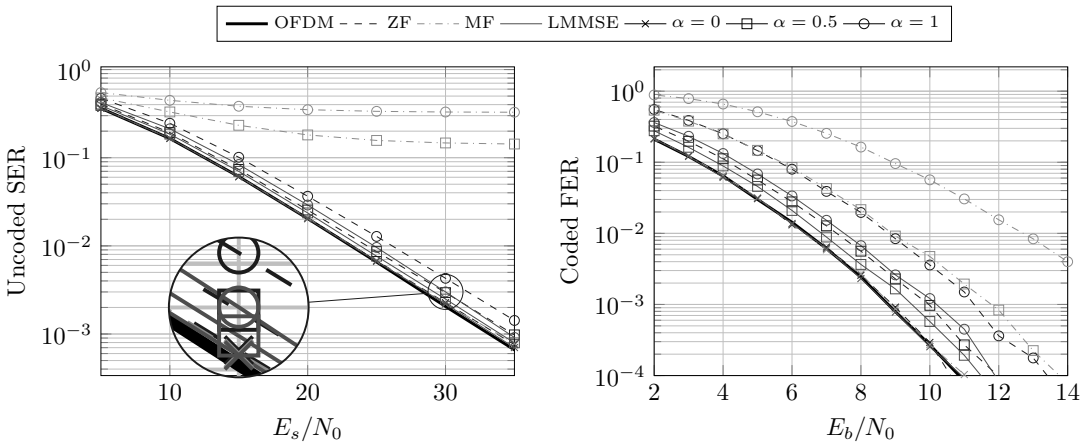

Figure 2.7: Coded and uncoded performance of single-antenna GFDM and OFDM in block-fading Rayleigh multipath channel with PDP $P[n] = [0, -1, -2, -3, -8, -17.2, -20.8]$dB, where this PDP is derived from the EPA channel model. GFDM Type II with $K = 128, M = 7$ and RC filter. 16-QAM modulation with Turbo code of rate $1/2$.

to self-interference is the smallest. As a corner case, for $\alpha = 0$ the modulation matrix $\mathbf{A}$ becomes orthogonal, there is no self-interference and the performance eventually lines up with OFDM. Apparently, treating self-interference as noise will not yield an optimal FER. Instead, we can harvest the information that is contained in the interference as shown in the subsequent chapters on receiver design, using advanced nonlinear receivers. This fact is even more pronounced when additional IAI occurs due to involving multiple antennas.

2.5 Summary

This chapter has laid the foundations for the treatment of different receiver architectures for MIMO-GFDM. In particular, the building blocks of a generic wireless point-to-point communication system have been introduced and the wireless channel was modelled. Moreover, the linear GFDM modulation was presented, leading to the convenient linear expression of the GFDM transmit signal

$$\vec{y} = \mathbf{A}\vec{d}.$$

Moreover, this linear model was extended to include MIMO and the linear effects of the wireless channel, eventually leading to a generic linear model

$$\vec{y} = \mathbf{H}\vec{d} + \vec{w},$$

which will be of central importance in the upcoming chapters. In addition, the performance of linear GFDM receivers in single-antenna systems was presented and compared to OFDM. The findings motivate the investigation of more sophisticated, non-linear, receiver algorithms to exploit the information that is contained in the self-interference, which we will focus on in the upcoming chapters. However, before focusing on receiver design we investigate, how the mathematical theory behind multicarrier systems, namely time-frequency analysis, can bring insights into the theoretical performance of prominent multicarrier systems.

Chapter 3

Multicarrier Systems in the Context of Gabor Theory

In his 1947 work "Theory of Communication" [Gab47], Dennis Gabor laid the mathematical foundations to the theory of multicarrier systems. Since then, a multitude of research has been conducted [FS02, MBH13, Böl03]. In this chapter, we first shortly introduce concepts and theorems from time-frequency analysis (TFA) that are relevant to the present work. Subsequently, we relate properties of multicarrier systems and in particular GFDM to the concepts of TFA. As an outcome of this relation, we will deduct theoretical properties of GFDM and derive low-complexity formulations for receiver implementations.

3.1 Time-Frequency Analysis and Gabor Theory

3.1.1 The Continuous-Time Case

Let x denote an arbitrary signal and let $x(t)$ denote the representation of this signal in the time domain. The same signal can be represented in the frequency domain in terms of its Fourier transform $X(f) = \int_{-\infty}^{\infty} x(t) \exp(-j2\pi ft)dt$ and both $x(t)$ and $X(f)$ contain all information about x. $x(t)$ describes the value of the signal at any given time, whereas $X(f)$ describes the contribution of any frequency to the signal. In other words, $x(t)$ provides us with exact information about the time-domain behaviour, but it does not tell us anything about the frequency of the signal around this time. Analogously, $X(f)$ provides accurate information about the frequency components of x, but does not describe any time-domain behaviour.

In many applications, the signal x is non-stationary and evolves over time. For these signals, it is desirable to obtain information about the frequency of the signal around a given time t_0. Here, we have to point out that the formulation of "frequency around a given time" is, strictly spoken, impossible, because a pure tone is infinitely wide in time. A rigorous treatment of this problem of *instantaneous frequency* is out of scope of this thesis, but more details can be found in e.g. [FS98, FS02, Grö01]. In short, limited by the uncertainty principle of TFA ("A signal cannot be time- and band-limited at the same time") [Dau90], for a given interval of length T around t_0, we can only reach a

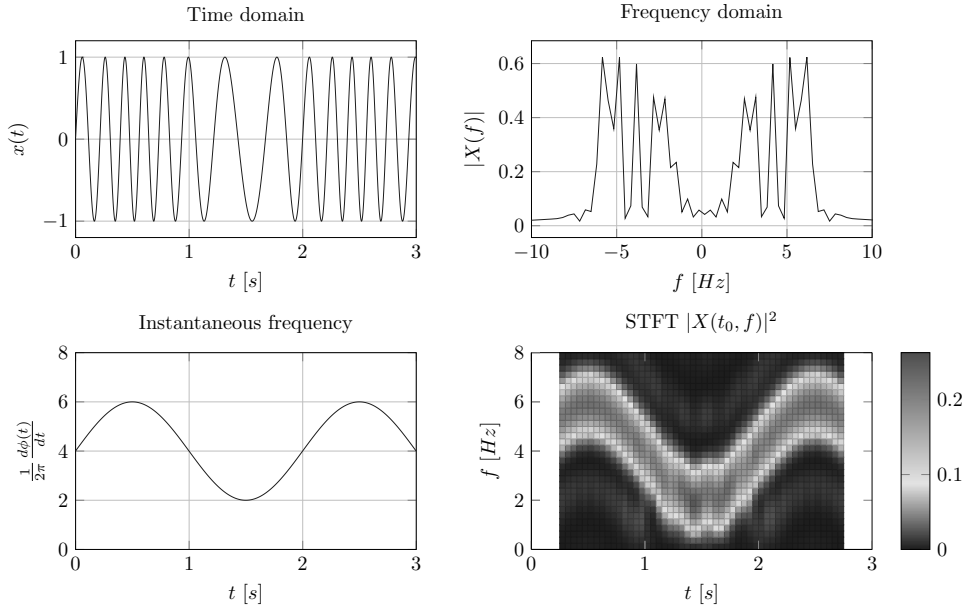

Figure 3.1: Example of the STFT of a frequency varying tone $x(t) = \sin(\phi(t))$ with $\phi(t) = 2\pi \int_0^t f(\tau)d\tau$ with instantaneous frequency $f(t) = 4 + 2\sin(\pi t)$. The time-domain plot $x(t)$ qualitatively shows that the instantaneous frequency changes over time, but no frequency value can be seen. Its spectrum $|X(f)|$ shows that the frequency is around 5Hz, but does not reveal any time-domain information. A quantitative analysis of instantaneous frequency over time is accomplished by the STFT in the right figure, showing that the frequency ranges between 2 and 6Hz which closely matches the analytic expression for $f(t)$. For the STFT, a Tukey window of length $T = 1/2$s with shape parameter 0.25 was used, hence the width of the curve of the STFT is approximately $1/T = 2$Hz.

resolution in frequency domain of $1/T$. The short-time Fourier transform (STFT) $X(t_0, f)$ of $x(t)$ provides the requested information by performing the Fourier transform of the multiplication of the signal with an analysis window $w(t)$[1] around t_0, given by

$$X(t_0, f) = \int_{-\infty}^{\infty} x(t)w(t - t_0)\exp(-j2\pi ft)dt. \tag{3.1}$$

Fig. 3.1 shows an example of the STFT of some artificial signal where the instantaneuos frequency changes over time. As is shown, the STFT accurately describes the time-frequency behaviour of the function.

Gabor transform and expansion. The STFT maps the one-dimensional signal $x(t), t \in \mathbb{R}$ to a two-dimensional signal $X(t_0, f), (t_0, f) \in \mathbb{R}^2$, hence it contains a significant amount of redundancy. In his 1947 work "Theory of communication" [Gab47] Dennis Gabor worked on the question: How dense does the STFT need to be sampled such that no information about $x(t)$ is lost? In particular, given the sampled STFT

$$a_{k,m} = X(mT, kF) = \langle x(t), w(t - mT)\exp(j2\pi kFt)\rangle = \left\langle x(t), w_{k,m}^{(F,T)}(t)\right\rangle \tag{3.2}$$

[1] Throughout this chapter we consider the noisefree case, such that we use $w(t)$ for denoting the analysis window without ambiguity.

where $\langle x(t), y(t)\rangle$ denotes the scalar product in $L^2(\mathbb{R})$ and $w_{k,m}^{(F,T)}(t) = w(t - mT)\exp(j2\pi kFt)$, what is the relation between T and F such that $\{a_{k,m}\}_{(k,m)\in\mathbb{Z}^2}$ completely describes $x(t)$ by means of

$$x(t) = \sum_{k\in\mathbb{Z}}\sum_{m\in\mathbb{Z}} a_{k,m} v(t - mT)\exp(j2\pi kFt) = \sum_{k\in\mathbb{Z}}\sum_{m\in\mathbb{Z}} a_{k,m} v_{k,m}^{(F,T)}(t), \tag{3.3}$$

where $v(t)$ is a suitable synthesis window function? Nowadays, the projection of $x(t)$ onto time-frequency shifts of $w(t)$ in (3.2) is termed *Gabor transform* whereas the linear combination of time-frequency shifts of $v(t)$ in (3.3) is called *Gabor expansion*. The set

$$\mathcal{G}(v, F, T) = \{v_{k,m}^{(F,T)}\}_{(k,m)\in\mathbb{Z}^2} \tag{3.4}$$

is also called a *Weyl-Heisenberg (WH) set* [Jan97].

Time-frequency localization and the Balian-Low theorem. Considering that a single coefficient $a_{k,m}$ in the Gabor expansion should optimally describe only a local aspect of the overall signal, the time-bandwidth product $\Omega(v) = \sigma_t^2(v)\sigma_f^2(v)$ of the synthesis window should be small, where $\sigma_t^2(v)$ and $\sigma_f^2(v)$ are spreading of v in time and frequency given by

$$\sigma_t^2(v) = \int_{-\infty}^{\infty}(t - \mu_t)^2 v(t)dt \qquad \sigma_f^2(v) = \int_{-\infty}^{\infty}(f - \mu_f)^2 V(f)df \tag{3.5}$$

with

$$\mu_t(v) = \int_{-\infty}^{\infty} tv(t)dt \qquad \mu_f(v) = \int_{-\infty}^{\infty} fV(f)df \tag{3.6}$$

being the center of mass in time and frequency and $V(f) = (\mathcal{F}v)(f)$ is the Fourier transform of $v(t)$. Gabor analyzed the question for a Gaussian window $v(t) = \exp(-\pi\left(\frac{t}{T}\right)^2)$ due to its best time-frequency localization $\Omega(v) = 2\pi$. He concluded that $x(t)$ is completely described by $\{a_{k,m}\}$, if $TF \leq 1$. However, later in [BGZ75] it was corrected, that for the Gaussian window, the coefficients are numerically stable only for $TF < 1$ and do not always exist for the case of *critical sampling* with $TF = 1$. In particular, the later found Balian-Low theorem (BLT) [Bal81, BHW98] enforces, that if for $TF = 1$ the pair (3.2) and (3.3) holds for all $x(t)$ for some $w(t)$, then $\Omega(v) \to \infty$ or $\Omega(w) \to \infty$. As a consequence, there do not exist any well-localized analysis and synthesis windows in the critical sampling case.

Dual windows and the Wexler-Raz duality condition. If for all $x(t) \in L^2(R)$ it holds

$$x(t) = \sum_{(k,m)\in\mathbb{Z}^2} a_{k,m} v_{k,m}^{(F,T)}(t) \qquad \text{with } a_{k,m} = \left\langle x(t), w_{k,m}^{(F,T)}(t)\right\rangle \tag{3.7}$$

for a pair $w(t), v(t) \in L^2(R)$ of analysis and synthesis window, $v(t)$ is termed the *dual window* of $w(t)$ and vice versa [2]. A sufficient and necessary condition for (3.7) to hold is the *Wexler-Raz duality condition* [WR90], given by

$$\left\langle w_{k,m}^{(1/T,1/F)}(t), v_{k',m'}^{(1/T,1/F)}(t) \right\rangle = \delta_{kk'}\delta_{mm'}, \tag{3.8}$$

i.e. the windows v and w are biorthogonal when time-frequency shifted on the dual lattice with time-frequency distance $1/T, 1/F$. Further, (3.8) is equivalent to [Jan98]

$$\left\langle w(t), v_{k',m'}^{(1/T,1/F)}(t) \right\rangle = \delta_{0k'}\delta_{0m'}. \tag{3.9}$$

Ron-Shen Duality principle. It can be shown [Jan98] that (3.7) can only hold for all $x(t) \in L^2(R)$ if $TF \leq 1$. In this case, $\mathcal{G}(v, F, T)$ forms a *frame* for $L^2(R)$. It is notable that the coefficients $a_{k,m}$ are in general not unique for $TF < 1$ [FS98], i.e. two different sets of $\{a_{k,m}\}$ can yield the same expansion $x(t)$ in (3.7). Consequently, the duality condition (3.9) does not uniquely determine the dual window, but for $TF < 1$ infinitely many dual windows exist [FS98].

In relation, the Ron-Shen duality principle [RS97] asserts that $\mathcal{G}(v, F, T)$ is a frame for $L^2(R)$ if and only if $\mathcal{G}(v, 1/T, 1/F)$ is a Riesz basis for the linear span of $\mathcal{G}(v, 1/T, 1/F)$. In particular this means that for $TF > 1$ the pair (3.7) only holds for a subspace of $L^2(R)$, but the expansion coefficients $a_{k,m}$ become unique [FS98]. We will see how this property influences the design of digital communication systems in the following section. A mathematical more rigorous, but accessible treatment of this topic can be found in e.g. [Chr03].

The Zak-Transform. Closely related to TFA is the Zak transform (ZT) [Bas98], given by

$$(\mathcal{Z}v)^{(T)}(\tau, \nu) = \sqrt{T} \sum_{m' \in \mathbb{Z}} v((\tau + m')T) \exp(-j2\pi\nu m') = \mathrm{DTFT}\{v((\tau + (\cdot))T)\}, \tag{3.10}$$

which is a unitary transform, with inverse

$$v((t + m')T) = \int_0^1 (\mathcal{Z}v)^{(T)}(t, \nu) \exp(j2\pi m'\nu) d\nu. \tag{3.11}$$

The ZT is quasi-periodic in τ and ν, i.e.

$$(\mathcal{Z}v)^{(T)}(\tau + k, \nu + m) = (\mathcal{Z}v)^{(T)}(\tau, \nu) \exp(j2\pi k\nu), \qquad (m, k) \in \mathbb{Z}^2, \tag{3.12}$$

hence all properties of $(\mathcal{Z}v)^{(T)}$ can be inferred from the fundamental rectangle $(0, 0) \leq (\tau, \nu) \leq (1, 1)$. As shown, the ZT can be considered as the discrete-time Fourier transform (DTFT) of a sampled version of $v(t)$, where the sampling offset τ is a parameter. The ZT is important for a variety of signal processing and time-frequency applications and a more

[2] If (3.7) holds for analysis and synthesis windows $w(t), v(t)$, it also holds for analysis window $v(t)$ and synthesis window $w(t)$ [FS98].

thorough treatment is provided in e.g. [Bas98, BH97, Jan88]. Here, we want to focus on an aspect in relation to the calculation of dual windows. In particular, an analysis $w(t)$ and synthesis window $v(t)$ are directly related in their Zak-domain according to [Str98]

$$(\mathcal{Z}v)^{(T)}(\tau,\nu) = \frac{(\mathcal{Z}w)^{(T)}(\tau,\nu)}{T\sum_{l=0}^{L-1}|(\mathcal{Z}w)^{(T)}(\tau-lT,\nu)|^2} \tag{3.13}$$

when $1/(TF) = L \in \mathbb{N}$ is an integer. In the case of critical sampling, i.e. $TF = 1$, the relation simplifies to

$$(\mathcal{Z}v)^{(T)}(\tau,\nu) = \frac{1}{T(\mathcal{Z}w)^{(T)}(\tau,\nu)^*}, \tag{3.14}$$

i.e. the ZT of one window is the element-wise inverse of the ZT of its dual. In accordance with the BLT, it was shown [Jan88] that the ZT of a window $v(t)$ with $\Omega(v) < \infty$ does become zero for some (τ,ν). In particular, if $v(t)$ is real-valued then $(\mathcal{Z}v)(\tau, 1/2) = 0$ for some τ and if $v(t)$ is even, i.e. $v(t) = v(-t)^*$, then $(\mathcal{Z}v)(1/2, 1/2) = 0$ [Jan88].

3.1.2 The Finite Discrete-Time Case

In the previous sections, the results from TFA have been stated for the continuous-time case. Since digital signal processing deals with discrete-time signals that originate from sampling bandlimited continuous-time signals, it is beneficial to take over the obtained results to a discrete setting. We further consider the discrete-time discrete-frequency case, which corresponds to periodic discrete-time functions[3]. In this setting, we can explain results from TFA with more intuitive arguments from linear algebra. The transition from continuous-time to finite discrete time is achieved via the *periodization and sampling trick* [Orr93], which we will describe in the following.

Periodization and sampling. Similar to how the GFDM discrete-time filter is derived in Sec. 2.4.2, the periodization and sampling trick can be applied to the Gabor expansion and transform [WR90, Orr93, Orr92] and the Zak transform [BH97, BG96]. To give an example of this periodization and sampling trick, let us derive the relation between the discrete [BH97] and the continuous-time [Jan88] Zak transform. Consider the (complex-valued) signal $f(t)$ with (two-sided) bandwidth F_s and its periodic version $f_T(t)$

$$f_T(t) = \sum_{u\in\mathbb{Z}} f(t-uT) \tag{3.15}$$

which is periodic with period T. If we sample $f_T(t)$ with sampling frequency F_s, we get

$$f_T[n] = f_T(n/F_s) = \sum_{u\in\mathbb{Z}} f\left(\frac{n-uTF_s}{F_s}\right). \tag{3.16}$$

[3] Intuitively, the relation between continuous-time and the periodic discrete-time signals is analogous to the relation between the continuous-time and discrete Fourier transform.

Hence, we have $N = TF_s$ samples per period and we can identify $f_T[n], n = 0, \ldots, N-1$ as an N-dimensional vector $\vec{f} \in \mathbb{C}^N$, which opens up the possibility to use common results from linear algebra for the present analysis. Let $N = KM$ with $K, M \in \mathbb{N}$ be an arbitrary factorization of N. Then, calculating the discrete Zak transform (DZT) of $f_T[n]$ with step-size K yields

$$
\begin{aligned}
(\mathcal{Z} f_T)^{(K)}(k,m) &\overset{(a)}{=} \sum_{m'=0}^{M-1} f_T[k+m'K] \exp\left(-j2\pi \frac{mm'}{M}\right) && (3.17)\\
&\overset{(b)}{=} \sum_{m'=0}^{M-1} \sum_{u\in\mathbb{Z}} f\left(\frac{k+m'K-uN}{F_s}\right) \exp\left(-j2\pi \frac{mm'}{M}\right) && (3.18)\\
&\overset{(c)}{=} \sum_{m'\in\mathbb{Z}} f\left(\frac{k+m'K}{F_s}\right) \exp\left(-j2\pi \frac{mm'}{M}\right) && (3.19)\\
&= \sum_{m'\in\mathbb{Z}} f\left(\left(m' + \frac{k}{K}\right)\frac{K}{F_s}\right) \exp\left(-j2\pi \frac{mm'}{M}\right) && (3.20)\\
&\overset{(d)}{=} (\mathcal{Z} f)^{(\frac{K}{F_s})}\left(\tau = \frac{k}{K}, \nu = \frac{m}{M}\right), && (3.21)
\end{aligned}
$$

where (a) is the definition of the DZT [BH97], (b) follows from (3.16), (c) is obtained by the substitution $m' \leftarrow m' + uM$. Eventually (d) points out that the DZT of the periodic and sampled version $f_T[n]$ of $f(t)$ equals the ZT of $f(t)$ sampled at $(k/K, m/M)$.

Discrete Gabor expansion and transform. Let $N = \Delta_F N_F = \Delta_T N_T$ with $\Delta_F, \Delta_M, N_F, N_T \in \mathbb{N}$ be two factorizations of the block length N. Then, the discrete Gabor expansion and transform pair is given by[Orr93, BG96, WR90]

$$
\begin{aligned}
x[n] &= \sum_{k=0}^{N_F-1} \sum_{m=0}^{N_T-1} a_{k,m} v[\langle n - m\Delta_T \rangle_N] \exp\left(-j2\pi \frac{k\Delta_F}{N} n\right) = \sum_{k=0}^{K-1} \sum_{m=0}^{M-1} a_{k,m} v_{k,m}^{(\Delta_F \Delta_M)}[n]\\
a_{k,m} &= \sum_{n=0}^{N-1} x[n] w[\langle n - m\Delta_T \rangle_N] \exp\left(j2\pi \frac{k\Delta_F}{N} n\right) = \left\langle x[n], w_{k,m}^{(\Delta_F,\Delta_T)}[n] \right\rangle_{\mathbb{C}^N},
\end{aligned}
\tag{3.22}
$$

where $\langle \cdot, \cdot \rangle_{\mathbb{C}^N}$ denotes the scalar product in $\mathbb{C}^N$ and $\langle \cdot \rangle_N$ denotes the argument modulo N, resulting from the periodization of w and v and $x[n], n = 0, 1, \ldots, N-1$ denotes the transformed or expanded signal. The sampling density of the Gabor transform is given by $\frac{\Delta_T \Delta_F}{N}$.

Discrete Gabor transform in a linear algebra setting. Let us summarize the results from section 3.1.1 with techniques from linear algebra. Therefore, let $\vec{x}, \vec{v}, \vec{w}, \vec{v}_{k,m}^{(\Delta_F,\Delta_T)}, \vec{w}_{k,m}^{(\Delta_F,\Delta_T)} \in \mathbb{C}^N$ denote the vector equivalents of $x[n], v[n], w[n], v_{k,m}^{(\Delta_F,\Delta_T)}[n], w_{k,m}^{(\Delta_F,\Delta_T)}[n]$ for $n = 0, \ldots, N-1$. Further, let $\vec{a} \in \mathbb{C}^{N_F N_T}$ denote the expansion coefficients with indexing $\vec{a}_{k+mN_F} = a_{k,m}$.

Then, the Gabor expansion and transform pair (3.22) becomes

$$\vec{x} = \mathbf{G}_v \vec{a} \tag{3.23}$$

$$\vec{a} = \mathbf{G}_w^H \vec{x} \tag{3.24}$$

where $\mathbf{G}_v$ is the $N \times N_F N_T$ matrix where the $(k + mN_F)$th column equals $\vec{v}_{k,m}^{(\Delta_F,\Delta_T)}$. Let us assume in the sequel that $\mathbf{G}_v$ has full rank, i.e. $\text{rank}(\mathbf{G}_v) = \min(N, N_F N_T)$.

If we substitute (3.24) into (3.23), we get

$$\vec{x} = \mathbf{G}_v \mathbf{G}_w^H \vec{x}. \tag{3.25}$$

Hence, for (3.25) to be true for all $\vec{x} \in \mathbb{C}^N$, we require $\mathbf{G}_v \mathbf{G}_w^H = \mathbf{I}$ which can only hold for some v, w if $N_F N_T \geq N$, i.e. $\mathbf{G}_w$ and $\mathbf{G}_v$ are fat matrices. This constraint is the equivalent of requiring $TF \leq 1$ such that (3.7) can hold for all $x(t) \in L^2(R)$. Even more, if $N_F N_T > N$, for a fixed v there exists infinitely many w such that $\mathbf{G}_v \mathbf{G}_w^H = \mathbf{I}$ and hence $\vec{a} = \mathbf{G}_w^H \vec{x}$ is not unique.

On the other hand, consider the substitution of (3.23) into (3.24), i.e.

$$\vec{a} = \mathbf{G}_w^H \mathbf{G}_v \vec{a}. \tag{3.26}$$

This can only hold for all $\vec{a} \in \mathbb{C}^{N_F N_T}$, if $N \geq N_F N_T$, which is equivalent to $TF \geq 1$. In this case, for a fixed v, $\vec{x} = \mathbf{G}_v \vec{a}$ lies in an $N_F N_T$-dimensional subspace of $\mathbb{C}^N$, i.e. $\vec{x}$ cannot reach all elements of $\mathbb{C}^N$. This duality is the linear algebraic explanation of the Ron-Shen duality for the infinite-dimensional case.

Furthermore, let $\vec{z}^{(f)} \in \mathbb{C}^N$ with $\vec{z}_{k+mK}^{(f)} = (\mathcal{Z} f)^{(K/F_s)}(m, k)$ denote the vectorized values of the DZT of $\vec{f}$. Then, $\mathbf{Z} = \mathbf{I}_K \otimes \mathbf{F}_M$ performs the DZT, i.e.

$$\vec{z}^{(f)} = \mathbf{Z} \vec{f}. \tag{3.27}$$

We immediately see that $\mathbf{Z}$ is a unitary matrix due to unitarity of $\mathbf{F}_M$, which is in line with the unitarity of the continuous and discrete ZT [HW89, BH97].

3.2 Multicarrier Systems and Gabor Theory

The transmit signal of classic linear multicarrier modulation systems can be readily interpreted as a Gabor expansion of the transmitted data symbols $d_{k,m}$, i.e.

$$x(t) = \sum_{m \in \mathbb{Z}} \sum_{k=-K/2}^{K/2-1} d_{k,m} g(t - mT) \exp(j2\pi kFt), \tag{3.28}$$

where K is the number of subcarriers and $g(t)$ is a prototype transmit filter. Furthermore, assuming a linear receiver, at the receiver a Gabor transform with the receiver filter $\gamma(t)$ is performed, given by

$$\hat{d}_{k,m} = \left\langle x(t), \gamma_{k,m}^{(F,T)}(t) \right\rangle. \tag{3.29}$$

The spectral efficiency ρ of the system is inversely proportional to the time-frequency distance, i.e. $\rho \sim \frac{1}{TF}$, i.e. the product between symbol duration and carrier spacing. Intuitively, we want to minimize TF for highest efficiency. However, the Ron-Shen duality principle implies that for $TF < 1$ the correspondence of $x(t)$ with the data sequence $\{d_{k,m}\}$ is not one-to-one, i.e. the same transmit signal $x(t)$ would correspond to infinitely many transmit data sequences $\{d_{k,m}\}$. This is clearly not practical due to detection ambiguity at the receiver side[4]. On the other hand, the critical sampling $TF = 1$ allows non-ambiguous detection where at the same time $x(t)$ can become every element of $L^2(R)$, leading to full utilization of the signal space. However, in this case due to the BLT $g(t)$ cannot be well-localized. Finally, with $TF > 1$, well-localized $g(t)$ exists that allow non-ambiguous detection. However, then all $x(t)$ are elements of a proper subspace of $L^2(R)$, and hence $x(t)$ cannot reach each element of $L^2(R)$. Therefore, the signal space is not fully utilized which leads to a reduced spectral efficiency compared to $TF = 1$.

CP-OFDM and its orthogonality. With the most prominent multicarrier waveform example being CP-OFDM, we can identify

$$g(t) = \begin{cases} 1 & -T_{CP} \leq t \leq T_S \\ 0 & \text{else} \end{cases} \tag{3.30}$$

$$T = T_S + T_{CP} \tag{3.31}$$

$$F = 1/T_S, \tag{3.32}$$

where T_S is the useful symbol duration and T_{CP} is the duration for the cyclic prefix. At the receiver side, the linear CP-OFDM demodulator uses a rectangular window of length T_S, i.e.

$$\gamma(t) = \begin{cases} 1 & 0 \leq t \leq T_S \\ 0 & \text{else} \end{cases}, \tag{3.33}$$

and achieves orthogonality in the sense of

$$\left\langle \gamma_{k',m'}^{(F,T)}, g_{k,m}^{(F,T)} \right\rangle = \delta_{kk'}\delta_{mm'}. \tag{3.34}$$

By using the rectangular filter, the spectrum of the OFDM signal becomes the slowly decaying sinc-function, implying a large OOB emission. Since $TF = \frac{T_S+T_{CP}}{T_S} > 1$ does not yield the critical sampling, in principle well-localized, orthogonal filters in the sense of (3.34) do exist for this density. However, the celebrated orthogonality property of CP-OFDM which distinguishes it from any other waveform is its channel independent

[4] Here, we refer to $d_{k,m} \in \mathbb{C}$, i.e. the data symbols can take any value. In practice, $d_{k,m}$ are elemements of the discrete constellation set, making $x(t)$ become elements of a discrete subspace of $L^2(R)$. Then, non-ambiguous detection is theoretically possible also for $TF < 1$. At the receiver side, a non-linear demodulator is required to resolve $x(t)$ to a specific discrete lattice point. In practice, the so-called faster-than-Nyquist (FTN) [ARÖ13] waveforms exploit this property and it has been shown that the transmit signal is non-ambiguous up to $TF = 0.8$ if $g(t)$ is a sinc function with BPSK modulation. This bound is nowadays known as the Mazo Limit [Maz75, RA09].

orthogonality. Assuming a time-invariant channel with impulse response $h(t)$ which is shorter than the CP, this special orthogonality can be expressed as

$$\left\langle \gamma_{k,m}^{(F,T)}(t), h(t) * g_{k,m}^{(F,T)}(t) \right\rangle = H(kF)\delta_{kk'}\delta_{mm'} \tag{3.35}$$

$$\left\langle \gamma_{k,m}^{(F,T)}, \gamma_{k',m'}^{(F,T)} \right\rangle = \delta_{kk'}\delta_{mm'}, \tag{3.36}$$

where $H(f) = (\mathcal{F}h)(f)$ is the Fourier transform of the channel impulse response. First the time-frequency shifted receiver filters form an orthogonal basis for the signal space, which is necessary to keep noise uncorrelated after filtering, and second, even in a multipath channel, which introduces ISI in the time domain, the carriers of CP-OFDM remain orthogonal. Mathematically, the OFDM modulation and demodulation unitarily diagonalize the time-invariant channel, which is the unique property of CP-OFDM compared to other waveforms and has made it popular in a multitude of wireless communication systems. Furthermore, it is this particular property which made its application to MIMO systems so straightforward.

FBMC/OQAM. FBMC/OQAM is another multicarrier waveforms, that even predates CP-OFDM [Cha66, Sal67]. It has been rediscovered in the context of 5G waveform research due to its notably low OOB emission while still achieving $TF = 1$. Though this seems to contradict the BLT, in FBMC/OQAM a slightly modified signal structure is used, according to

$$x(t) = \sum_{m\in\mathbb{Z}} \sum_{k=-K/2}^{K/2-1} d_{k,m} g(t - m\frac{T_S}{2}) \exp(j2\pi k \frac{t}{T_S}) \tag{3.37}$$

$$d_{k,m} = j^{k+m} \begin{cases} \Re\{a_{k,m/2}\} & m \text{ even} \\ \Im\{a_{k,(m-1)/2}\} & m \text{ odd} \end{cases}, \tag{3.38}$$

where $a_{k,m}$ are the complex-valued QAM symbols and $d_{k,m}$ are real-valued transmit symbols, which are transformed according to the offset-QAM (OQAM) rule [SSL02]. Apparently for FBMC we have $TF = \frac{1}{2}$, but each data symbol is real-valued instead of complex-valued. This signal construction is derived from the mathematical concept of Wilson bases [DJJ91, Woj07, WOJ08], which circumvent the BLT by allowing orthogonal, well-localized bases, when the filters are simultaneously concentrated at positive and negative frequencies, i.e. the frequency-shifted filters remain real-valued [Grö01]. In OQAM modulation, this constraint is transformed into real-only data symbols with complex-valued filters. Hence, the orthogonality at the receiver is given by

$$\Re \left\langle \gamma(t - m\frac{T}{2}) \exp(j2\pi \frac{kt}{T}), g(t - m'\frac{T}{2}) \exp(j2\pi \frac{k't}{T}) \right\rangle = \delta_{kk'}\delta_{mm'}, \tag{3.39}$$

where the receiver filter $\gamma(t) = g(t)$ is equal to the transmitter filter and interference occurs only on the ignored imaginary part.

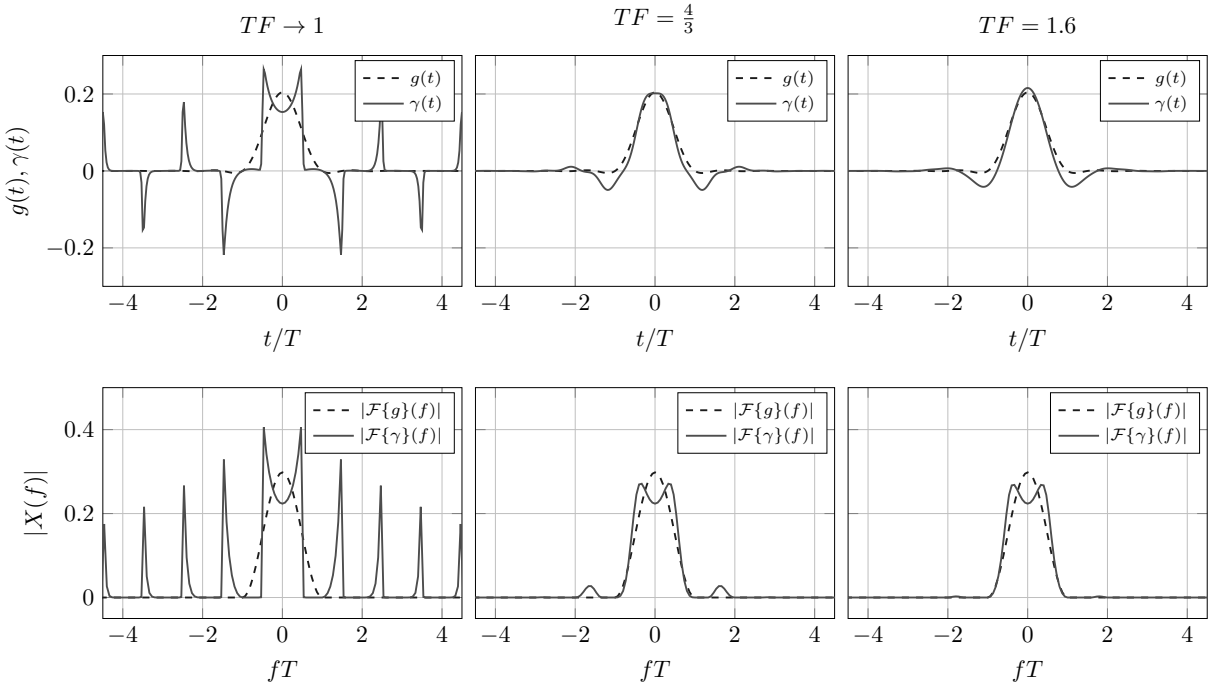

Figure 3.2: Time and frequency response of biorthogonal filters with different TF, where $g(t)$ is a RC filter designed for a symbol duration of $T = 1s$ with rolloff $\alpha = 1$. For $TF \to 1$, the BLT constraints the time-frequency localization and the receiver filter becomes wide in time and frequency. For larger TF, the receiver filter becomes more and more localized.

BFDM. In BFDM [KWJM14], biorthogonal transmit and receive filters are used. In order to be not bound by the BLT, in BFDM spectral efficiency is sacrificed (i.e. $TF > 1$) to achieve well-localized filters. In addition to exhibiting a lower OOB emission, well-localized filters are beneficial in doubly-dispersive channels [MBH13, MH11], as they occur in high-mobility scenarios. As these channels are both time- and frequency-dispersive a well-localized filter in time and frequency creates less interference than non-localized filters when subject to Gabor transform based receivers. Fig. 3.2 shows the biorthogonal transmit and receiver prototype filters for different values of TF. As shown, the biorthogonal receiver filter $\gamma(t)$ becomes more localized in time and frequency, when TF increases.

Moreover, filter-bank multicarrier filtered multitone (FBMC/FMT) [AFB11, CEÖ02] can be considered a special case of BFDM, where the transmitter filter is a half-Nyquist filter. At the receiver a matched filter receiver is employed, yielding an ISI-free overall filter response. At the cost of spectral efficiency, the subcarrier spacing is such that adjacent subcarriers do not overlap and hence no ICI occurs and biorthogonality between transmitter and receiver is ensured.

3.3 GDFM in a Gabor Transform Setting

In this section we will establish the relation between the finite discrete Gabor transform and expansion and GFDM and derive the consequences that become apparent from this relation. As any wireless communication signal, the GFDM signal is certainly bandlimited,

and its circular convolution property and discrete time-baseband processing can naturally be treated in the finite-dimensional setting established in Sec. 3.1.2. The results that are presented in the following summarize the author's work published in [MMF14a], [MGF15].

GFDM Modulation as a critically sampled Gabor expansion. Letting $\Delta_F = M, N_F = K$ and $\Delta_T = K, N_T = M$ we end up with a critically sampled Gabor expansion and transform pair, given by

$$x[n] = \sum_{k=0}^{K-1} \sum_{m=0}^{M-1} a_{k,m} v[\langle n - mK \rangle_N] \exp\left(j2\pi \frac{kn}{K}\right) \tag{3.40}$$

$$a_{k,m} = \sum_{n=0}^{N-1} x[n] w^*[\langle n - mK \rangle_N] \exp\left(j2\pi \frac{kn}{K}\right) \tag{3.41}$$

and we can immediately see that (3.40) exactly matches the modulation equation for GFDM established in (2.28) with $d_{k,m} \equiv a_{k,m}$ and $v[n] \equiv g[n]$. Hence, we can establish the connection $\mathbf{A} = \mathbf{G}_g$ and the GFDM modulation

$$\vec{x} = \mathbf{A}\vec{d} \tag{3.42}$$

equals a critically sampled discrete Gabor expansion.

Linear receivers as critically sampled Gabor transform. Further, we can, under the assumption of an ideal channel, associate the three linear receiver types from section 2.4.3 with the corresponding Gabor transform operation (3.24).

1. The MF receiver with $\hat{d}_{MF} = \mathbf{A}^H \vec{x}$ performs a critically sampled Gabor transform with analysis window $\vec{\gamma}_{MF} = \vec{g}$. Hence, the MF receiver achieves perfect reconstruction, if $\mathbf{A}$ is a unitary matrix or, equally, if $\vec{g}^H \vec{g}_{k,m} = \delta_{0k}\delta_{0m}$, i.e. $\{\vec{g}_{k,m}\}_{k,m}$ forms an orthonormal basis for $\mathbb{C}^N$.

2. For the ZF receiver operation $\hat{d}_{ZF} = \mathbf{A}^{-1}\vec{x}$, from $\mathbf{G}_w^H = \mathbf{A}^{-1}$ it immediately follows, that the rows of $\mathbf{A}^{-1}$ are time-frequency shifts of a prototype receiver filter $\vec{\gamma}_{ZF}$ and hence $\mathbf{A}^{-H}$ obeys the same structure as $\mathbf{A}$. Furthermore, $\mathbf{A}^{-1}\mathbf{A} = \mathbf{I}$ implies that $\vec{\gamma}_{ZF}$ is the dual window to $\vec{g}$, which we denote by $\vec{\gamma}_{ZF} = D(\vec{g})$ and we see that the columns and rows of $\mathbf{A}$ and $\mathbf{A}^{-1}$ form biorthogonal WH sets.

3. Under the assumption of a regular $\mathbf{A}$, the expression $\hat{d}_{\text{LMMSE}} = \mathbf{A}^H(\mathbf{A}\mathbf{A}^H + \sigma^2\mathbf{I})^{-1}\vec{x}$ for the LMMSE receiver with ideal channel can be reformulated to $\hat{d}_{\text{LMMSE}} = (\mathbf{A} + \sigma^2(\mathbf{A}^{-1})^H)^{-1}\vec{x}$. This expression points out that the LMMSE filter matrix is the inverse of a critically sampled Gabor expansion matrix with window $\vec{g} + \sigma^2 D(\vec{g})$, and is hence itself a Gabor transform matrix. Accordingly, the LMMSE filter operation performs a critically sampled Gabor transform with analysis window $D(\vec{g} + \sigma^2 D(\vec{g}))$.

These standard linear GFDM receivers commonly perform a critically sampled Gabor transform, however with different receiver filters. Therefore, the low-complexity frequency-domain implementation that has been proposed in [GNN+13] for the MF receiver can readiliy be applied for implementing ZF and LMMSE receivers, where just the receiver filter needs to be adapted. Furthermore, the more recently proposed time-domain demodulation technique [MMG+16] is generically applicable for MF, ZF and LMMSE receivers.

Observing that $\|\vec{g}\|^2 = \|\vec{g}_{k,m}\|^2$ for all k, m, the NEF of a ZF receiver, which is given by $\xi = \frac{1}{N}\mathrm{tr}(\mathbf{A}^{-1}\mathbf{A}^{-H})$ (cf. Sec. 2.4.3), can be simplified to

$$\xi = \frac{1}{N}\mathrm{tr}(\mathbf{A}^{-1}\mathbf{A}^{-H}) = \|D(\vec{g})\|^2. \tag{3.43}$$

Efficient Receiver filter calculation. As we have shown before, the calculation of the ZF and LMMSE filter matrices requires the calculation of the dual window $D(\vec{g})$, given the prototype filter $\vec{g}$. The dual window $D(\vec{g})$ can be efficiently obtained from (3.14), which describes the relation between the synthesis window $\vec{v}$ and its dual window $\vec{w}$ in the Zak-domain in the case of critical sampling in continuous time. Therefore, in the finite-dimensional case we have

$$D(\vec{g}) = \mathbf{Z}^H[(\mathbf{Z}\vec{g})^{\circ -1}]^*, \tag{3.44}$$

where $(\cdot)^{\circ -1}$ denotes elementwise inversion. Since $\mathbf{Z} = \mathbf{I}_K \otimes \mathbf{F}_M$, a multiplication with $\mathbf{Z}$ equals the K-fold calculation of an M-point DFT and can therefore be done very efficiently. Hence, the calculation of ZF and AWGN channel LMMSE receiver filters does not require to invert a huge matrix, but can be reduced to several short DFT operations [MMF14a]. Furthermore, due to unitarity of $\mathbf{Z}$, the NEF of the ZF is given in direct relation to the transmitter filter by $\xi = \|(\mathbf{Z}\vec{g})^{\circ -1}\|^2$, i.e. small values in $\mathbf{Z}\vec{g}$ imply a larger NEF. For the LMMSE receiver with presence of a multipath fading channels, a low-complexity implementation has been proposed by the author in [MGF15] which bases on the block-diagonalization of block-circulant matrices via the DZT [Qiu95].

Singular Modulation matrix. In original works on GFDM (e.g. [MMG+14]) it has been pointed out that $\mathbf{A}$ can become a singular matrix. In this case, $\mathrm{rank}(\mathbf{A}) < MK$ and hence the signal space does not have maximum dimension, leading to ambiguous detection at the receiver side. Clearly, this situation is not desirable.

With the knowledge about the Gabor expansion properties, we can immediately understand the singularity as a direct consequence of the BLT. By means of the BLT, any well-localized filter $g(t)$ has a zero in its continuous-time Zak transform (ZT). Since the DZT is the sampled ZT, whenever the zero is sampled, $D(\vec{g})$ does not exist (cf. (3.44)) and hence $\mathbf{A}$ becomes singular. Furthermore, assuming a continuous ZT (which is the case for any well-localized function [HW89]), even when the zero is not directly sampled, finer sampling moves the sampling points closer to the zero (see also Fig. 3.3). Hence, the NEF of a ZF receiver increases with increasing M and/or K.

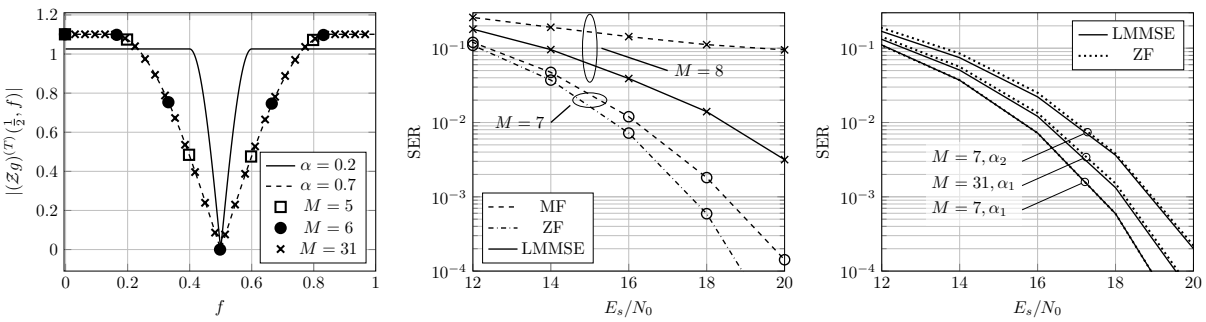

Figure 3.3: Effect of even and odd M and different rolloff factors on the DZT (left) and uncoded SER (right) for GFDM with RC filter. The marks in the left figure denote the sampling points of the continuous ZT. The smaller the rolloff, the narrower the valley in the ZT and the larger the sampled values, improving $\mathbf{A}$ matrix condition. $K = 128, \alpha_1 = 0.2, \alpha_2 = 0.7$, 16QAM modulation.

Constraint on M and K. For a real-valued, symmetric, well-localized filter $g(t)$ we have $(\mathcal{Z}^{(T)}g)(1/2, 1/2) = 0$ [Jan88]. Therefore, for commonly used GFDM filters such as the RC or root raised cosine (RRC), this requires either M or K to become an odd number. For the alternative of the non-symmetric Xia-filter [TB99a, Xia97, MMGF14] it can be shown that $(\mathcal{Z}^{(T)}g)(1/4, 1/2) = 0$ [MMF14a] and similarly either M or K should be odd-valued. Fig. 3.3 illustrates the sampling of the continuous ZT of a RC filter and presents the resulting SER performance of different linear receivers. The results confirm the theoretical derivations and show a poorer performance for larger rolloff-factors and increased M. Remarkably also the MF receiver, which is not directly connected to the condition of $\mathbf{A}$, shows a significantly degraded performance for even values of M.

The constraint on odd M or K puts a major restriction on the real-time implementation, since the most efficient radix-2 FFT algorithms are not applicable in this case. Only recently, a filter design has been found [NMZF17], which allows even-valued M and K for well-localized filters derived from e.g. standard RC filters. The design exploits the frequency-shifting property of the ZT and applies a shift of half a frequency bin to the prototype filter, to shift the zero of the ZT away from the sampling point [NMZF17].

3.4 Summary

In this chapter, we have first reviewed the fundamental results from time-frequency analysis (TFA) that are most relevant for theoretically describing multicarrier systems. We would like to note that the present summary is by far not exhaustive and more detailed literature on TFA is available in e.g. [FS98, Grö01, FS02]. Subsequently, we have described multicarrier systems with concepts from TFA. The relation between the mathematical theory of TFA and the practical application of multicarrier modulation is a beautiful example, how mathematical results directly have implications on real-world applications. As one example, the Ron-Shen duality principle explains, why $TF = 1$ is the limiting case for maximizing spectral efficiency, as the data becomes ambiguous for $TF < 1$. As another example, Wilson bases find their direct application in the Offset-QAM modulation used for FBMC/OQAM. In particular for GFDM, we have identified the modulation

and linear demodulation as a critically sampled Gabor expansion and transform pair, being the archetype of multicarrier modulation. We have used this knowledge to derive low-complexity filter calculations and provide insights into criteria when the modulation matrix becomes singular.

Chapter 4

Transmit Diversity Techniques for GFDM

5G use cases of URLLC such as time-critical industrial automation or communications for vehicular coordination require an extremely high reliability of the transmission (e.g. frame error rates of 10^{-6}) with at the same time low latency (e.g. 1ms end-to-end). These requirements pose a massive challenge onto the PHY. In 4G systems, reliability is obtained by the hybrid automatic repeat request (HARQ) procedure, which retransmits erroneously received packets. However, the tight timing constraint of URLLC does not allow retransmissions. Hence, the reliability of the link itself becomes of major importance. Since the temporal fading of the wireless channel is the main source of erroneously received packets, it is advisable to reduce the impact of deep channel fades onto the data transmission. Here, the concept of diversity is a central topic: In plain terms, diversity refers to the situation where the same data is transmitted over different channels. In case these channels realize independent fading processes, there is a good chance that if one channel is in a deep fade, the other channel is currently not in a deep fade, and as such the data can be transmitted more reliably.

Diversity techniques aim to exploit two (or more) independent channels to reliably transmit data. With spatial diversity, the channels are the paths between pairs of transmit and receive antennas. Accordingly, we can distinguish between two types of spatial diversity: Receive diversity and transmit diversity. Receive diversity can be obtained, when multiple receive antennas receive the same signal and hence their signals can be combined to yield an improved signal. Here, selection combining, equal-gain combining and maximum ratio combining (MRC) are main techniques to exploit receive diversity [Bre03]. The application of these techniques for GFDM is straight-forward in the frequency domain and will not be treated in this work.

On the other hand, transmit diversity can be obtained by a single receive antenna and multiple transmit antennas. Moreover, both diversity techniques can be combined by employing multiple receive and transmit antennas. For transmit diversity, one cannot simply transmit identical signals from all antennas, but the signals at the transmit antennas have to be precoded such that the diversity gain can be exploited. To understand this, let us consider a flat fading system as in Fig. 4.1. Assume the transmit signals on both

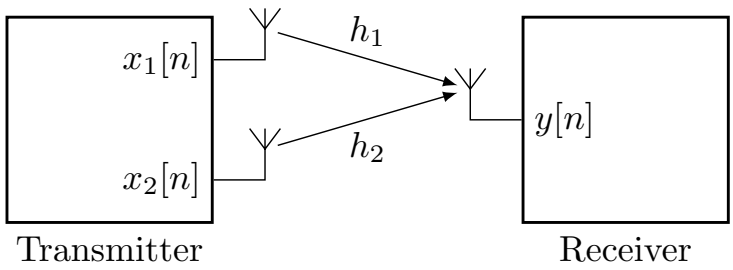

Figure 4.1: Example of a flat-fading system exploiting transmit diversity. The two antennas TX1 and TX2 transmit the signals $x_1[n], x_2[n]$ over the two flat channels with channel gain h_1, h_2, which can be assumed to be independently Rayleigh-faded. Hence, the received signal is given by $y[n] = h_1 x_1[n] + h_2 x_2[n] + w[n]$, where $w[n]$ is AWGN.

antennas are equal, i.e. $x_1[n] = x_2[n]$ and by coincidence for one channel realization we have $h_1 = -h_2$. Then, the received signal $y[n]$ is only noise since both signals cancel out. Hence, more sophisticated methods to achieve transmit diversity are necessary, which are in general termed *Space-Time Codes*, since they distribute the transmit signal in space (i.e. the antennas) and time (i.e. they perform some precoding along the time-dimension)[1]. The overall aim of these techniques is to combine the signal at the receiver such that it appears to be transmitted over a single channel with better fading conditions. Available transmit diversity techniques can be categorized into two classes, depending on the need of CSI at the transmitter side (TX-CSI).

The most basic method to achieve transmit diversity that does not require TX-CSI is to transmit the same signal first over one antenna and then over the other. However, obviously, this technique halves the data rate. Instead, more advanced techniques have been developed [NSC00]. In the following, we will first introduce the prominent Alamouti space-time block code (STBC) [Ala98] for flat fading and later on describe how this technique can be applied to the non-orthogonal GFDM system. The results in this chapter are based on the author's works in [MMF14b, MMG+15, MMM+15].

4.1 The Alamouti Space Time Block Code

The most prominent example of an STBC for a flat-fading channel is the Alamouti technique [Ala98]. This technique employs two transmit antennas to transmit a single data stream without reducing the data rate compared to a single transmit antenna. Remarkably, it was proven that such code exists only for 2 transmit antennas. For more antennas the orthogonality constraint implies a rate reduction [TJC99]. The Alamouti STBC keeps both signal streams orthogonal to each other, such that low-complexity linear STC combining at the receiver yields the optimal detection rule. However, the technique requires the wireless channel to be constant over two symbol slots.

[1] There also exist space-frequency codes (SFC) [LW00] which essentially work similar, but the redundant signals are transmitted over different frequencies rather than different time slots.

Transmit and receive signal. The Alamouti code groups the transmit symbol stream $x[n]$ into adjacent pairs of two samples, $x_{n,1}, x_{n,2}, n \in \mathbb{Z}$ with

$$x_{n,1} = x[2n]\,, \qquad x_{n,2} = x[2n+1]. \tag{4.1}$$

Then, the transmit signals $x_1[n]$ and $x_2[n]$ are given by

$$x_1[2n] = x_{n,1}\,, \qquad x_1[2n+1] = x_{n,2}\,, \tag{4.2}$$
$$x_2[2n] = -x^*_{n,2}\,, \qquad x_2[2n+1] = x^*_{n,1}. \tag{4.3}$$

At the receive antenna, the signals transmitted over the two channels superpose and the received signal $y[n]$ is given by

$$y[2n] = h_1 x_{n,1} - h_2 x^*_{n,2} + w[2n] \qquad y[2n+1] = h_1 x_{n,2} + h_2 x^*_{n,1} + w[2n+1]. \tag{4.4}$$

STC Combining. In order to obtain the transmitted symbols $x_{n,1}, x_{n,2}$, the following operations are carried out:

$$\begin{aligned} \frac{h_1^* y[2n] + h_2 y[2n+1]^*}{\|h_1\|^2 + \|h_2\|^2} &= x_{n,1} + \frac{h_1^*}{\|h_1\|^2 + \|h_2\|^2} w[2n] + \frac{h_2}{\|h_1\|^2 + \|h_2\|^2} w[2n+1]^* \\ \frac{-h_2 y[2n]^* + h_1^* y[2n+1]}{\|h_1\|^2 + \|h_2\|^2} &= x_{n,2} - \frac{h_2}{\|h_1\|^2 + \|h_2\|^2} w[2n]^* + \frac{h_1^*}{\|h_1\|^2 + \|h_2\|^2} w[2n+1] \end{aligned} \tag{4.5}$$

As this expression shows, already a linear processing at the receiver decouples the both transmitted signals, sucht that they appear to be transmitted over a single channel with gain $\|h_1\|^2 + \|h_2\|^2$. Hence, optimal ML detection is possible boils down to the single-antenna case with very low decoding complexity. Assuming i.i.d. Rayleigh fading for both $\|h_1\|, \|h_2\|$, the equivalent channel gain $\|h_1\|^2 + \|h_2\|^2$ is Chi-squared distributed with 4 degrees of freedom. Compared to the single channel gain $\|h_1\|^2$ which is Chi-squared distributed with 2 degrees of freedom, the probability for deep fades is significantly reduced [TV05], yielding the diversity gain.

Application of Alamouti STC for CP-OFDM. Originally, the Alamouti STBC only works for flat-fading channels, i.e. adjacent symbols in time do not interfer with each other due to ISI. This assumption requires a narrowband transmission such that the symbol length is much longer than the multipath response of the channel. However, in the orthogonal CP-OFDM system, we have seen that the multipath channel is diagonalized (cf. Sec. 3.2), and each carrier experiences perfectly flat fading, due to the application of the CP. In this case, the Alamouti STBC can be straight-forwardly applied to each carrier separately, and each carrier can be demodulated independently. Hence, at the receiver, for the kth carrier we have the relation

$$Y_1[k] = H_1[k]^* d_{1,k} + H_2[k] d^*_{2,k} \qquad Y_2[k] = H_1[k]^* d_{2,k} - H_2[k] d^*_{1,k}, \tag{4.6}$$

where $d_{i_t,k}$ are the QAM symbols on the kth carrier and i_tth timeslot ($i_t = 1, 2$), $Y_{i_t}[k]$ is the received constellation at the kth carrier and $H_{i_t}[k]$ is the frequency response of

the kth carrier from the i_tth transmit antenna to the receiver, which is constant over the two subsequent symbols. Then, the space-time combining can be carried out for each carrier separately analogously to (4.5). Even though here we focus on receivers with a single antenna, the Alamouti STC can be straight-forwardly extended to multiple receiver antennas, by applying MRC at the receiver.

In addition to performing the Alamouti coding in the time domain, a multicarrier structure allows to perform Alamouti coding in the frequency domain, leadign to so called space-frequency codes (SFCs). Instead of using two adjacent time slots to convey two data symbols using two transmit antennes with STC, SFC employs two adjacent OFDM subcarriers to convey two data symbols using two transmit antennas [LW00]. The advantage of this system is a reduced latency, as only one time slot is needed. However, this technique requires that two adjacent carriers have the same frequency response. Hence, this technique is less applicable with highly frequency-selective channels. In the following, we focus on STC, however the presented techniques for GFDM can straight-forwardly be extended to SFC.

4.2 The Alamouti STBC for GFDM

Starting from the straight-forward application of the STBC to CP-OFDM, it is tempting to introduce the Alamouti STBC for GFDM according to the following pattern: Given the transmit data matrix $\mathbf{D}$ as in Sec. 2.4.2, we define the data symbols $\mathbf{D}_1, \mathbf{D}_2$ to be transmitted from the first and second transmit antenna, as follows

$$\mathbf{D}_1 = \begin{pmatrix} 0 & d_{0,1} & d_{0,2} & \dots & d_{0,M-2} & d_{0,M-1} \\ 0 & d_{1,1} & d_{1,2} & \dots & d_{1,M-2} & d_{1,M-1} \\ \vdots & \vdots & \vdots & \ddots & \vdots & \vdots \\ 0 & d_{K-1,1} & d_{K-1,2} & \dots & d_{K-1,M-2} & d_{K-1,M-1} \end{pmatrix} \tag{4.7}$$

$$\mathbf{D}_2 = \begin{pmatrix} 0 & -d^*_{0,2} & d^*_{0,1} & \dots & -d^*_{0,M-1} & d^*_{0,M-2} \\ 0 & -d^*_{1,2} & d^*_{1,1} & \dots & -d^*_{1,M-1} & d^*_{1,M-2} \\ \vdots & \vdots & \vdots & \ddots & \vdots & \vdots \\ 0 & -d^*_{K-1,2} & d^*_{K-1,1} & \dots & -d^*_{K-1,M-1} & d^*_{K-1,M-2} \end{pmatrix}. \tag{4.8}$$

Here, the Alamouti encoding is performed on two adjacent columns in the data matrix. Assuming an odd M (cf. Sec. 3.3), we leave the first column empty. However, this time resource can serve as a guard symbol for OOB reduction [MMGF14] or can contain pilots for channel estimation or synchronization [MF16]. In case of even M, e.g. when applying the pulse shaping design from [NMZF17], also the first column of $\mathbf{D}$ can be used for data transmission. The received signal after CP removal at the receiver is given by

$$\vec{y} = \mathbf{H}_1 \mathbf{A} \mathrm{vec}(\mathbf{D}_1^T) + \mathbf{H}_2 \mathbf{A} \mathrm{vec}(\mathbf{D}_2^T) + \vec{w}, \tag{4.9}$$

where $\mathbf{H}_1, \mathbf{H}_2$ denote the circulant channel matrices generated from channel impulse responses $\vec{h}_1, \vec{h}_2$ and $\vec{w}$ denotes AWGN. In the OFDM case, the channels are diagonalized by

the modulation and demodulation and hence each symbol experiences flat fading and no ISI occurs. However, when taking over this demodulation technique to GFDM according to

$$\hat{d}_{k,m} = \frac{H_1[k]^* y_{k,m} + H_2[k] y_{k,m+1}^*}{|H_1[k]|^2 + |H_2[k]|^2} \qquad m \text{ even} \tag{4.10}$$

$$\hat{d}_{k,m} = \frac{H_1[k]^* y_{k,m} - H_2[k] y_{k,m-1}^*}{|H_1[k]|^2 + |H_2[k]|^2} \qquad m \text{ odd}, \tag{4.11}$$

where $y_{k,m} = \vec{\gamma}_{k,m}^H \vec{y}$ is the received constellation point at subcarrier k and subsymbol m and $\vec{\gamma}$ is any receiver filter from Sec. 2.4.3, the channel-induced ISI is not resolved appropriately and hence an error floor depending on the channel length will appear [MMF14b, MMM+15]. There, $H_t[k]$ is the kth element of the K-point DFT of $\vec{h}_t$, which describes the average frequency response on the kth subcarrier. The difficulty with (4.10) is that GFDM is not a channel-independent orthogonal system as CP-OFDM is (see Sec. 3.2), but a multipath channel introduces interference that needs to be removed before GFDM demodulation is performed. Hence, more sophisticated methods for the application of the Alamouti STBC to GFDM need to be found. In the following we will introduce two of the possible techniques.

4.2.1 Time-Reversal Space-Time Coding for GFDM

The time-reversal STC (TR-STC) has been proposed by [AD01] to allow the use of STC for single carrier transmission over frequency-selective channels. The proposed approach operates on two subsequent signals $\vec{x}_i$ and $\vec{x}_{i+1}$ of length N which are separated by a CP. Their corresponding discrete Fourier transforms are $\vec{X}_{(\cdot)} = \mathbf{F}\vec{x}_{(\cdot)}$. The transmit signals on both antennas for two subsequent time slots $1, 2$ are given by

	TX Antenna 1	TX Antenna 2
Time slot 1	$\mathbf{F}^{\mathrm{H}}\vec{X}_1$	$-\mathbf{F}^{\mathrm{H}}\vec{X}_2^*$
Time slot 2	$\mathbf{F}^{\mathrm{H}}\vec{X}_2$	$\mathbf{F}^{\mathrm{H}}\vec{X}_1^*$,

(4.12)

Note that the property

$$(\mathbf{F}^{\mathrm{H}}\vec{X}_i^*)_n = x_i^*[\langle -n \rangle_N] \tag{4.13}$$

of the discrete Fourier transform reasons the name "time-reversal space-time coding".

At the receiver, after removing the CP, the transmit signals appear circularly convolved with the CIR and therefore, the channel is diagonalized in the frequency domain. Assuming the channel remains constant during the transmission of two subsequent blocks, the received blocks in the frequency domain are given by

$$\vec{Y}_1 = \vec{H}_1 \circ \vec{X}_1 - \vec{H}_2 \circ \vec{X}_2^* + \vec{W}_1 \tag{4.14}$$

$$\vec{Y}_2 = \vec{H}_1 \circ \vec{X}_2 + \vec{H}_2 \circ \vec{X}_1^* + \vec{W}_2, \tag{4.15}$$

where $\vec{H}_{i_t} = \sqrt{N}\mathbf{F}\vec{h}_{i_t}$. Using a ZF equalizer, the received signals can be combined in the frequency domain by

$$\begin{aligned} \hat{\vec{X}}_1 &= \vec{H}_{eq}^{-1} \circ (\vec{H}_1^* \circ \vec{Y}_1 + \vec{H}_2 \circ \vec{Y}_2^*) \\ \hat{\vec{X}}_2 &= \vec{H}_{eq}^{-1} \circ (\vec{H}_1^* \circ \vec{Y}_2 - \vec{H}_2 \circ \vec{Y}_1^*), \end{aligned} \tag{4.16}$$

$$\text{where } \vec{H}_{eq}^{-1} = (\vec{H}_1^* \circ \vec{H}_1 + \vec{H}_2^* \circ \vec{H}_2)^{\circ -1}. \tag{4.17}$$

Finally, the estimates of the transmitted blocks are acquired by inverse Fourier transform

$$\hat{\vec{x}}_i = \mathbf{F}^{\mathrm{H}} \hat{\vec{X}}_i, \quad i = 1, 2. \tag{4.18}$$

Essentially, the TR-STC treats the signal as if it was a CP-OFDM signal where the constellation points have been replaced with $\vec{X}_i$, i.e. the frequency domain samples of the transmit signal. Accordingly, the frequency domain combining is done equally to the CP-OFDM case.

TR-STC can be directly applied to GFDM. Consider two data vectors $\vec{d}_1, \vec{d}_2$ that generate two consecutive GFDM frames $\vec{x}_1, \vec{x}_2$ by

$$\vec{x}_i = \mathbf{A}\vec{d}_i. \tag{4.19}$$

The GFDM signals $\vec{x}_i$ and $\vec{x}_{i+1}$ can be space-time encoded as described in (4.12) and (4.16) can be used to recover the signals on the receiver side. Then, conventional linear GFDM demodulation according to Sec. 2.4.3, e.g. using the ZF demodulation can be carried out to get an estimate of the transmitted symbols.

$$\hat{\vec{d}}_i = \mathbf{A}^{-1}\hat{\vec{x}}_i. \tag{4.20}$$

Furthermore, the noise covariance after demodulation that is used for soft-QAM demapping is given by

$$\mathbf{R}_{\tilde{n}} = \sigma^2 \mathbf{A}^{-1} \mathrm{diag}(\vec{H}_{eq}^{-1}) \mathbf{A}^{-H}. \tag{4.21}$$

This technique has been analyzed in detail, including multiple-access and scheduling aspects in [MMG+15]. Despite achieving full diversity gain and very low complexity, TR-STC has the drawback of encoding two adjacent GFDM blocks. This requires the channel to remain stable over two GFDM blocks and increases latency to two GFDM blocks. Alternatively, a more elaborate decoding scheme for the STC in (4.7) is shown in the following.

4.2.2 Widely Linear Equalization for Space-Time Coded GFDM

Considering the problems of naive application of the Alamouti STC combining in (4.10), a more garnished technique is required to successfully decode a GFDM signal that has been space-time encoded according to (4.7). In particular, as has been pointed out, the problem is to perform Alamouti STC combining on data that suffers from inter-symbol

interference. In [GOS+02] the application of widely linear estimation (WLE) [PC95] has been proposed to combat this problem and achieve the full diversity gain even in interfered transmissions. In order to exploit this technique for GFDM, let us write (4.7) as

$$\mathbf{D}_1 = (\vec{0} \quad \mathbf{D}_s^{(1)}) \qquad\qquad \mathbf{D}_2 = (\vec{0} \quad \mathbf{D}_s^{(2)}) \tag{4.22}$$

with

$$\mathbf{D}_s^{(1)} = \begin{pmatrix} d_{0,1} & \dots & d_{0,M-1} \\ d_{1,1} & \dots & d_{1,M-1} \\ \vdots & \ddots & \vdots \\ d_{K-1,1} & \dots & d_{K-1,M-1} \end{pmatrix} = \mathbf{D}_s \qquad\qquad \mathbf{D}_s^{(2)} = \mathbf{D}_s^* \mathbf{P}_s \tag{4.23}$$

being the non-zero columns of $\mathbf{D}_1, \mathbf{D}_2$, respectively and

$$\mathbf{P}_s = \mathbf{I}_{\frac{M-1}{2}} \otimes \begin{pmatrix} 0 & 1 \\ -1 & 0 \end{pmatrix} \tag{4.24}$$

denotes the transformation from $\mathbf{D}_s^*$ to $\mathbf{D}_s^{(2)}$. Moreover, let $\mathbf{A}_s$ denote $\mathbf{A}$ where the columns that correspond to the first subsymbol are removed. Then, the signal transmitted from the ith antenna is given by

$$\vec{x}^{(i)} = \mathbf{A}_s \mathrm{vec}(\mathbf{D}_s^{(i)^T}). \tag{4.25}$$

Accordingly, taking the N-point DFT of (4.9) we can express the received signal $\vec{Y}$ in the frequency domain by

$$\vec{Y} = \begin{pmatrix} \hat{\mathbf{H}}_1 & \hat{\mathbf{H}}_2 \mathbf{P} \end{pmatrix} \begin{pmatrix} \vec{d}_s \\ \vec{d}_s^* \end{pmatrix} + \vec{W}, \tag{4.26}$$

where $\vec{W} = \mathbf{F}_N \vec{w}$, $\hat{\mathbf{H}}_i = \mathbf{F}_N \mathbf{H}_i \mathbf{A}_s$, $\vec{d}_s = \mathrm{vec}(\mathbf{D}_s^T)$ and $\mathbf{P} = \mathbf{I}_K \otimes \mathbf{P}_s^T$.

From the linear model (4.26), one could readiliy derive an LMMSE estimator for $\vec{d}_s$, treating $\hat{\mathbf{H}}_2 \mathbf{P} \vec{d}_s^*$ as (correlated) interference. Unfortunately, since $E[\vec{d}_s (\vec{d}_s^*)^H] = 0$ as $\vec{d}_s$ takes rotationally symmetric constellation points, for the LMMSE receiver the interference appears uncorrelated. On the other hand, clearly there is dependence, in fact a deterministic relation, between $\vec{d}_s$ and $\vec{d}_s^*$, given by $E[\vec{d}_s (\vec{d}_s^*)^T] = \mathbf{I}$, which is known as the pseudocorrelation between $\vec{d}_s$ and $\vec{d}_s^*$. This extra relation is considered by a widely linear estimation (WLE). Referring to the derivation in Appendix A.1, the WLE for $\vec{d}_s$ in (4.26) is given by [MMM+15]

$$\begin{pmatrix} \hat{\vec{d}}_s \\ \hat{\vec{d}}_s^* \end{pmatrix} = (\hat{\mathbf{H}}_{eq}^H \hat{\mathbf{H}}_{eq} + \sigma^2 \mathbf{I})^{-1} \hat{\mathbf{H}}_{eq}^H \begin{pmatrix} \vec{Y} \\ \vec{Y}^* \end{pmatrix} \tag{4.27}$$

$$\text{with } \hat{\mathbf{H}}_{eq} = \begin{pmatrix} \hat{\mathbf{H}}_1 & \hat{\mathbf{H}}_2 \mathbf{P} \\ \hat{\mathbf{H}}_2^* \mathbf{P} & \hat{\mathbf{H}}_1^* \end{pmatrix}. \tag{4.28}$$

Equation (4.27) yields the widely linear MMSE receiver, and it can be easily modified to get the widely linear ZF receiver by fixing $\sigma^2 = 0$ in (4.27). Accordingly, the noise variance for widely linear ZF and MMSE receivers can be derived straight-forwardly from (2.43).

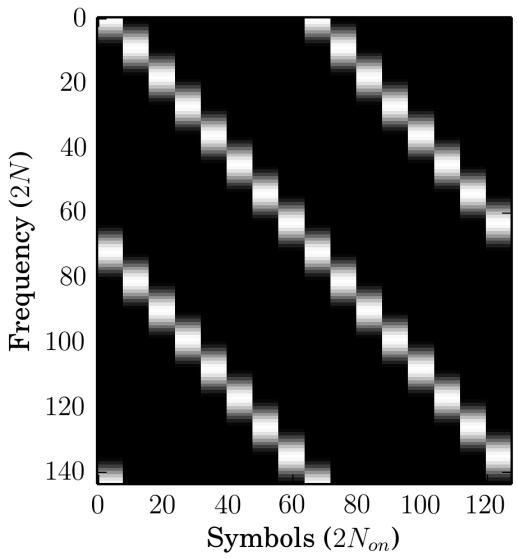

Figure 4.2: Sample equivalent channel $\hat{\mathbf{H}}_{eq}$ for $M = 9$, $K = 8$ using a RC filter with $\alpha = 1$.

Algorithm complexity. According to (4.27), the widely linear minimum mean squared error (MMSE) and ZF estimators for $\mathbf{d}_s$ require to solve a linear equation system with $2K(M-1) = 2N_{on}$ equations. The application of general-purpose solvers for such systems requires a computational complexity of cubic order in both the number of subcarriers and subsymbols which is prohibitively complex for real-time implementations of practical system dimensions. However, due to the sparsity of the transmit filter in the frequency domain, a solution can be found with linear complexity in the number of subcarriers, where the number of complex operations is considered as a figure of merit.

Consider the equivalent channel matrix $\hat{\mathbf{H}}_{eq}$ in (4.28). As shown in Sec. 2.4.2, $\mathbf{F}_N\mathbf{A}$ is a band-diagonal matrix with only B non-zero coefficients per column, where B is the number of non-zero coefficients of $\mathbf{F}_N\vec{g}$. For example with a RC filter with rolloff α, we have $B = (1+\alpha)M$. Accordingly,

$$\mathbf{F}_N\mathbf{H}_i\mathbf{A}_s = \mathbf{F}_N\mathbf{H}_i\mathbf{F}_N^H\mathbf{F}_N\mathbf{A}_s \tag{4.29}$$

is also band-diagonal since the channel matrix $\mathbf{H}_i$ is diagonalized by the DFT. Since $\mathbf{P}$ only operates within isolated subcarriers, the blocks of $\hat{\mathbf{H}}_{eq}$ are also band-diagonal. An illustration for $\hat{\mathbf{H}}_{eq}$ is given in Fig. 4.2.

Let $\mathbf{T}_{2U}$ be a $2U \times 2U$ permutation matrix given by

$$\mathbf{T}_{2U} = [\mathbf{e}_0\ \mathbf{e}_U\ \mathbf{e}_1\ \mathbf{e}_{U+1}\ \ldots\ \mathbf{e}_{U-1}\ \mathbf{e}_{2U-1}]^T \tag{4.30}$$

where $\mathbf{e}_i$ is a zero column vector of length $2U$ with 1 at its ith position. The permutation is applied to (4.27) by

$$\begin{pmatrix} \hat{\vec{d}}_s \\ \hat{\vec{d}}_s^* \end{pmatrix} = \mathbf{T}_{2N_{on}}^H(\underbrace{\mathbf{T}_{2N_{on}}\hat{\mathbf{H}}_{eq}^H\mathbf{T}_{2N}^H}_{\mathbf{Q}_{\mathrm{eq}}^H}\underbrace{\mathbf{T}_{2N}\hat{\mathbf{H}}_{eq}\mathbf{T}_{2N_{on}}}_{\mathbf{Q}_{\mathrm{eq}}}+\sigma^2\mathbf{I})^{-1}\underbrace{\mathbf{T}_{2N_{on}}\hat{\mathbf{H}}_{eq}^H\mathbf{T}_{2N}^H}_{\mathbf{Q}_{\mathrm{eq}}^H}\mathbf{T}_{2N}\begin{pmatrix} \vec{Y} \\ \vec{Y}^* \end{pmatrix} \tag{4.31}$$

where $\mathbf{Q}_{\text{eq}}$ is a sparse matrix of size $2N \times 2N_{on}$ where each column only has $2B$ non-zero elements. Since fixed permutations essentially only describe a fixed wiring, this transformation does not increase implementation complexity.

The calcuation $\mathbf{Q}_{\text{eq}}^H(\vec{Y}^T \quad (\vec{Y}^*)^T)^T$ requires only $2BN$ complex multiplications. $(\mathbf{Q}_{\text{eq}}^{(j)})^H\mathbf{Q}_{\text{eq}}^{(j)}$ is a positive definite Hermitian band diagonal matrix with periodic boundary conditions with $S = 4(M-1)-1$ superdiagonals[2] since only the subsymbols of adjacent subcarriers overlap in the frequency domain. The periodic boundary condition exists due to the edge subcarriers, that wrap around in the discrete frequency domain. Accordingly, such subcarriers simultaneously have frequency components at the lowest and highest frequencies, making them unsuitable for spectral localization and are normally not used, i.e. $K_{on} < K$. In this case, the periodic boundary conditions vanish and the band diagonal structure of (4.31) can be solved with $N_{on}((S^2+1)+4S)$ complex multiplications [(NA, LAPACK zpbsv]. If $K = K_{on}$, the periodic boundary conditions can be overcome with the application of the Woodbury formula [PTVF07] and the solution is accomplished with an extra effort in the order of $\mathcal{O}(K \cdot M^3)$ complex multiplications which is still linear with the number of subcarriers. Hence, by exploiting the structure of the equation system, the computational effort can be significantly reduced to $\mathcal{O}(K \cdot M^3)$ compared to $\mathcal{O}(K^3M^3)$ when general-purpose solvers are employed. In the beneficial case of empty edge carriers, even the application of the Woodbury formula is not necessary at all and complexity reduces to $\mathcal{O}(K \cdot M^2)$

4.2.3 Simulation Results

This section presents simulation results for uncoded and coded transmissions for the presented techniques to achieve transmit diversity with GFDM. We show both the performance of ZF equalization for TR-STC encoded GFDM signals and of widely linear equalization for STC-encoded GFDM. Tab. 4.1 shows the system parameters that have been used in the simulations.

Time-Reversal Space-Time Coding. For the TR-STC simulation, GFDM was configured according to GFDM Type-I, i.e. in the simulation OFDM suffers from a larger CP overhead. In particular, the ratio ρ between CP overhead for GFDM and OFDM is given by (see Sec. 2.4.1)

$$\rho = \frac{1}{1+\frac{(M-1)T_{CP}}{MT_O+T_{CP}}} = \frac{1}{1+\frac{(9-1)\cdot 16}{9\cdot 64+16}} = 0.82 \triangleq -0.85\text{dB}. \tag{4.32}$$

In case of uncoded transmission, the theoretic expression of the SER of GFDM and OFDM in block-fading Rayleigh fading has been derived in [MMG+15] (also see Appendix), and an approximation is given by

$$Pr(\text{Symbol error}) \approx 4\beta \sum_{i=0}^{1} \binom{1+i}{i} \left(\frac{1+\epsilon}{2}\right)^i, \tag{4.33}$$

[2] $4(M-1)-1$ holds for RC with rolloff $\alpha = 1$. For smaller alpha, S decreases.

Table 4.1: Simulation parameters for space-time coding simulations.

Parameter	Symbol	GFDM	OFDM in Fig. 4.3	OFDM in Fig. 4.4
Number of Subcarriers	K	64	64	$64 \cdot 9$
Allocated Subcarriers	K_{on}	64	64	$64 \cdot 9$
Number of Subsymbols	M	9	1	1
Prototype filter	$\vec{g}$	RC	Rect	Rect
Bandwidth			5 MHz	
CP length			16 samples	
Modulation			16-QAM	
Channel Code			Rate 1/2 Turbo Code, 8 Turbo iterations	
Codeword length			2048 bits	
Channel Model			EVA PDP	
Fading Model			Block Rayleigh fading	

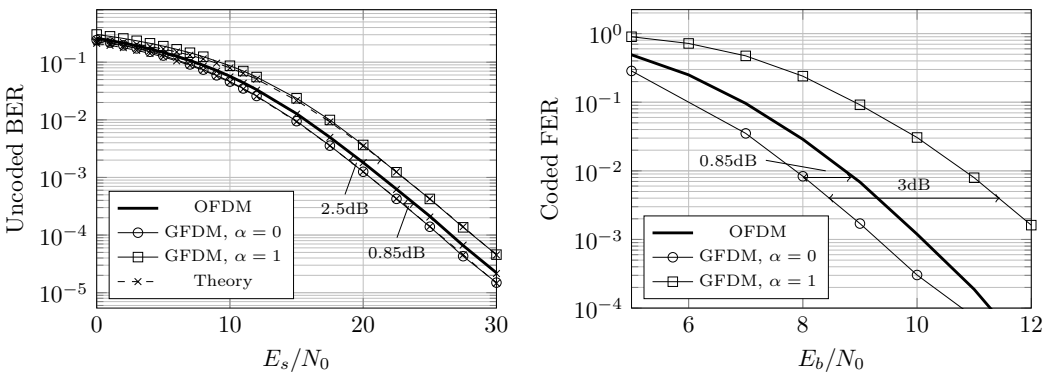

Figure 4.3: Simulated performance for TRSTC GFDM. The overhead due to CP for GFDM and OFDM is considered in the E_b/N_0 calculation.

where

$$\beta = \left(\frac{\sqrt{\mathcal{J}} - 1}{\sqrt{\mathcal{J}}}\right)\left(\frac{1-\epsilon}{2}\right)^2, \tag{4.34}$$

$$\epsilon = \sqrt{\frac{\frac{3}{\mathcal{J}-1}\frac{E_s}{\xi_0 N_0}}{2 + \frac{3}{\mathcal{J}-1}\frac{E_s}{\xi_0 N_0}}}, \tag{4.35}$$

with E_S/N_0 denoting the average symbol to noise energy ratio, $\mathcal{J} = 2^\mu$ denotes the size of the QAM constellation and ξ_0 denotes the product of the CP overhead and the NEF of GFDM. Equation (4.33) follows from the well-known expression for the SER in flat fading channels with diversity combining, which is e.g. given in [SA05, Eq. (9.23)]. There, only the equivalent signal to noise ratio (SNR) needs to be adapted to account for the noise enhancement and CP overhead. Assuming that due to Gray-mapping only one bit error occurs per symbol error [Pro95], we have

$$Pr(\text{Bit error}) = \frac{1}{\mu} Pr(\text{Symbol error}). \tag{4.36}$$

Fig. 4.3 presents the simulated performance of the TRSTC GFDM system, in comparison to a conventional STC OFDM system for coded and uncoded transmission. There,

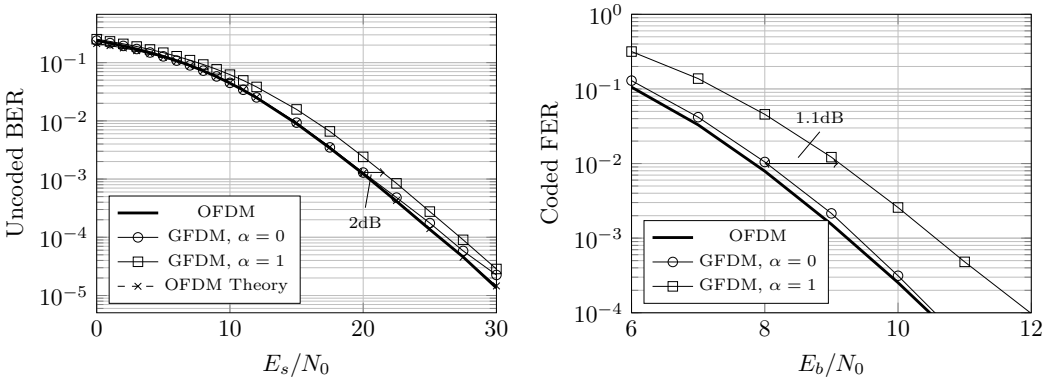

Figure 4.4: Simulated performance for widely linear MMSE equalization for STC-GFDM.

the CP overhead is reflected in the E_b/N_0 calculation. In the case of TRSTC GFDM, the space-time combining of GFDM and OFDM is very similar, since both systems combine and equalize the received signal in the frequency domain. As an additional processing step, GFDM performs ZF equalization of the GFDM modulation matrix, whereas the OFDM data is directly obtained from the equalized signal. In case of $\alpha = 0$, the GFDM equalization is unitary, and hence no extra distortion is introduced. In this case, the calculated CP overhead $\rho = -0.85$dB is directly reflected in the obtained coded and uncoded performance. When the rolloff increases, the noise enhancement of the ZF GFDM equalizer (cf. Sec. 2.4.3) comes into play and the performance curve shifts to the right by the amount of the NEF.

Fig. 4.3 shows a close match between the theoretic and simulated curves for the uncoded bit error rate, which indicates that the approximation in (4.33) is very tight. Additionally, for $\alpha = 1$, we see a significant BER degradation due to the high NEF for the non-orthogonal filter. In the simulation setup, the NEF amounts $\xi = 1.77 \triangleq 2.5$dB, which can also be observed in Fig. 4.3. For $\alpha = 0$, GFDM slightly outperforms OFDM due to the smaller CP overhead. In the coded results, we can observe the 0.85dB shift between the OFDM curve and the GFDM curve for $\alpha = 0$. Clearly, the gap stems from the CP overhead of OFDM and the unitary GFDM equalization yields an optimal detection. For $\alpha = 1$, we observe a gap that is larger than the expected 2.5dB stemming from the NEF. We can explain this larger gap by the fact that the ZF equalization matrix for $\alpha = 1$ is not unitary. Hence, the equalization introduces post-equalization noise correlation. In the subsequent soft-QAM demapping according to Sec. 2.3, this correlation is not considered. Accordingly, we see a larger gap in the coded performance curves.

Widely Linear MMSE Equalization. Fig. 4.4 presents the obtained simulation results with the widely linear MMSE equalizer for GFDM. In this case, GFDM was configured according to Type-II, i.e. one GFDM block has equal length as one OFDM symbol. Hence, both systems have a similar CP overhead. We have used this configuration to emphasize its usage for low-latency applications, compared to the TR-STC GFDM system. Here, we have assumed that the first column of the GFDM data matrix is allocated with pilots and assume the same pilot overhead for OFDM. Looking at the uncoded results

for low SNR, GFDM with $\alpha = 0$ follows the OFDM curve. For higher SNR, the slope of the GFDM curve, compared to OFDM, decreases. In [MMM+15], this observation is explained by a non-uniform noise-enhancement over the subcarriers, which eventually yields a degradation in the SER performance. For $\alpha = 1$, the gap is 0.5dB smaller than expected from the NEF. We can explain this by the application of the LMMSE equalizer, which does trade noise enhancement for a small amount of self-interference and can therefore improve the performance compared to a ZF equalizer. This effect becomes even more obvious in the coded FER performance in Fig. 4.4, where the gap between $\alpha = 0$ and $\alpha = 1$ reduces to $1.1dB$. Nevertheless, the orthogonal OFDM system outperforms GFDM with $\alpha = 0$ by approximately 0.18dB at a FER of 10^{-3}. In the WLE setting, even for $\alpha = 0$, the equalizer matrix in (4.27) is not unitary, and therefore introduces noise correlation after equalization. Hence, the soft-QAM demapping as described in Sec. 2.3 is not optimal, which explains the performance degradation. On the other hand, the GFDM approach using WLE exhibits half the latency of OFDM, as it requires only one block for the STC application. Accordingly, also the channel needs to be stable for only one block, allowing for more rapid channel variations. Equal latency could be achieved when using SFC for OFDM, however with the premise that adjacent subcarriers experience the same fading coefficient, which makes it unsuitable for highly frequency selective scenarios.

4.3 Summary

Even though receiver diversity is theoretically easy to achieve, it requires multiple antennas at the receiver. Transmit antenna diversity is an important means to increase reliability of a transmission when a receiver cannot afford multiple receive antennas and is widely applied in today's communication systems. In this chapter we have provided two solutions to achieve transmit diversity with GFDM and compared their performance to the straight-forward algorithm for OFDM. In particular we have proposed TR-STC which encodes the GFDM transmit signal from two subsequent blocks. This method achieves full diversity gain with low complexity, but at the cost of increased latency and requires the channel to be static for two subsequent blocks. Alternatively, we have proposed a widely linear equalizer for GFDM which harvests diversity when the STC is performed within one GFDM block. When comparing the simulated performance in the uncoded case, it was found that the proposed (widely) linear receivers for GFDM achieve full diversity and perform similar to OFDM, depending on the rolloff. However, we conclude that the information loss of the soft-out QAM demapper by ignoring post-equalization noise correlation is larger for GFDM, leading to a degraded coded performance compared to OFDM. Our findings imply that linear detection for GFDM cannot achieve superior performance compared to OFDM and more elaborate receiver structures should be analyzed in the sequel. The problem of interference becomes even more severe when IAI needs to be considered, as is the case in spatial multiplexing (SM) systems. Therefore, in the following chapter, we propose two non-linear receivers for spatially multiplexed GFDM streams and analyze their performance and complexity.

Chapter 5

Non-Iterative Detection for Spatially Multiplexed GFDM

In the previous chapter we have analyzed how linear GFDM demodulators can be used to detect space-time encoded GFDM signals. We have seen that the linear receivers severely suffer from self-interference, such that smaller rolloff factors yielded better performance. In this chapter, we analyse a non-linear non-iterative receiver structure that can beneficially exploit the extra information coupling introduced by the self-interference and aim at optimal maximum likelihood (ML) decoding performance. We apply this algorithm to spatially multiplexed GFDM signals. In order to explain the beneficial effect of self-interference, we introduce the equivalence between the received signal of linearly modulated data and points on a lattice. We further introduce the notion of the minimum distance of this lattice and connect it to the error performance of the modulation. Subsequently, we introduce the proposed receiver structure for GFDM and analyze it in terms of complexity and detection performance for coded and uncoded transmission. The results in this chapter are based on the author's works in [MGZF15, MZF16b].

System model. In the present and following chapter we consider the general linear model

$$\vec{y} = \mathbf{H}\vec{d} + \vec{w}, \tag{5.1}$$

where $\vec{w}$ is complex-valued zero-mean AWGN with variance σ^2. Moreover, $\vec{y}$ is the received signal and $\mathbf{H}$ is the equivalent channel matrix that contains the modulation operation and the wireless channel. This model is generally applicable to any linear modulation, including MIMO transmission (cf. Sec. 2.2) and can be expressed in both time and frequency domain.

The equivalent channel $\mathbf{H}$ can become very large, but most of the time it has a very special structure. For example in case of the $N_T \times N_R$ MIMO transmission using orthogonal CP-OFDM, in the frequency domain $\mathbf{H}$ is equivalent to a block-diagonal matrix, where each $N_R \times N_T$ block corresponds to the inter-antenna interference on a single subcarrier.

Let us first detail out the linear system model for GFDM. Consider a MIMO GFDM system with N_T transmit and N_R receive antennas operating in spatial multiplexing mode which equally distributes transmit power over the antennas. Then, the signal $\vec{y}$ at the

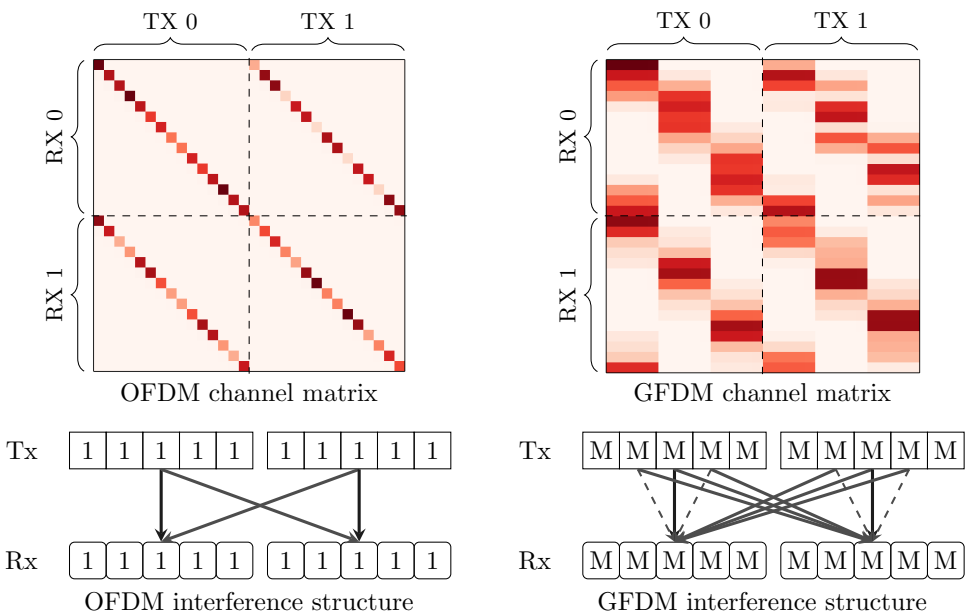

Figure 5.1: Comparison of GFDM and OFDM channel structure for a 2×2 MIMO system.

receive antennas is given by

$$\underbrace{\begin{bmatrix} \vec{y}_1 \\ \vdots \\ \vec{y}_R \end{bmatrix}}_{\vec{y}} = \underbrace{\begin{bmatrix} \mathbf{H}_{1,1}\mathbf{A} & \dots & \mathbf{H}_{1,T}\mathbf{A} \\ \vdots & \ddots & \vdots \\ \mathbf{H}_{R,1}\mathbf{A} & \dots & \mathbf{H}_{R,T}\mathbf{A} \end{bmatrix}}_{\mathbf{H}} \underbrace{\begin{bmatrix} \vec{d}_1 \\ \vdots \\ \vec{d}_T \end{bmatrix}}_{\vec{d}} + \vec{w}. \tag{5.2}$$

Here, $\mathbf{H}_{i_r,i_t}$ is the circulant channel matrix between the i_tth transmit and i_rth receive antenna, $\vec{d}$ contains all $\vec{\delta}_{i_t}$, representing the transmit data of the i_tth transmit antenna and $\vec{w} \sim \mathcal{CN}(0, \sigma^2 \mathbf{I}_{RN})$ is AWGN. Note that (5.2) also holds for OFDM, when $\mathbf{A}$ is the unitary Fourier transform (FT) matrix. A similar model can also be formulated in the frequency domain, where $\mathbf{H}_{i_r,i_t}$ are diagonal channel matrices and $\mathbf{A}$ is the GFDM modulation matrix in the frequency domain.

OFDM and GFDM interference structure. Fig. 5.1 compares the frequency domain channel structure of an example 2×2 OFDM and GFDM system. Apparently, the OFDM channel matrix is equivalent to a block-diagonal system with blocks of size 2×2, and each block corresponds to a single subcarrier. Hence, all subcarriers are decoupled and can be treated separately. This property makes CP-OFDM attractive for MIMO applications, since it diagonalizes the channel and does only yield IAI at the receiver.

In contrast, the GFDM channel structure is very different. The orthogonality is missing, and M symbols on each subcarrier interfer with each other due to channel ISI. Furthermore, adjacent subcarriers interfer due to the overlapping subcarriers, creating ICI. Eventually, as in every MIMO system, IAI occurs from signals of different antennas. The system suffers from three-dimensional interference (ISI, ICI, IAI) and cannot be straightforwardly decoupled into separate, smaller systems.

Role of self-interference. At first glance, the self-interference does not appear beneficial for detection. However, the opposite can be the case. Self-interference has a very different character than pure noise: It contains information about the transmitted signal. Hence, one can understand self-interference as an additional constraint at the symbol level, which provides one more error correction criterion for optimal detection and can yield a performance gain. However, in order to harvest this gain, the interference needs to be accurately resolved, which can only be achieved by non-linear receivers, which do not treat interference as additional noise (as purely linear receivers would do).

A similar principle is intuitively known for conventional MIMO-OFDM systems. Though LMMSE receivers perform optimal for single-antenna systems, in the MIMO case they by far do not reach the optimal performance. Instead, non-linear receivers employing sphere-decoders [AF16, SB10] or SIC [BC12] can be employed to harvest the gain from the interference, which comes in the shape of increased slope in the bit error rate curves. As a counter-example, consider an artificial MIMO-OFDM system, where the channel matrix is always diagonal (i.e. there is no IAI). Such system is IAI-free and hence orthogonal, but the well-known MIMO gains that stem from the cross-talk between the antennas will not occur.

Hence, the existence of self-interference in a system is a double-edged sword: If a receiver algorithm is able to accurately resolve it, a boost in detection performance is achieved, compared to an orthogonal system. However, in case the interference cannot be resolved, a performance degradation compared to orthogonal systems is observed. To achieve an optimal detection performance, the detection of all transmit symbols needs to be done in a joint manner. Apparently, since $\mathbf{H}$ can become very large, the algorithm complexity is a severe issue for the optimal detection in GFDM. Hence, besides designing high-performance receiver algorithms for GFDM, it is always important to keep its complexity in mind. Fortunately, for GFDM the interference is subcarrier-localized, meaning that only adjacent carriers interfer with each other, which leads to a banded structure of $\mathbf{H}$. We will see later on, how this structure allows powerful detection algorithms with affordable complexity.

5.1 The Linear Model as a Lattice Transform

In Chapter 3 in the context of TFA, the transmit data vector $\vec{d}$ was treated as a continuous variable, that could take any value from $\mathbb{C}^N$. However in reality, this is not true, since the elements $\vec{d}$ are discrete constellation points. With linear detection, the assumption of continuous values for $\vec{d}$ is kept for equalization, which causes a performance loss. Instead, one can take advantage of the fact that $\vec{d}$ only takes discrete values and consequently, $\mathbf{H}\vec{d}$ also only takes a finite number of different values. In fact, $\mathbf{H}\vec{d}$ in (5.1) forms a subset of a lattice.

Definition of a lattice. Let $\mathbf{H}$ be a full-rank $N \times N$ matrix[1]. The lattice $\mathcal{L}_H$ is defined as the set

$$\mathcal{L}_H = \{\mathbf{H}\vec{d} \mid \vec{d} \in \mathbb{Z}^N + j\mathbb{Z}^N\}. \tag{5.3}$$

A lattice is a set of regularly positioned discrete points in N-dimensional space and $\mathbf{H}$ is called the basis of the lattice. Essentially, the lattice is spanned by all integer linear combinations of the column vectors of $\mathbf{H}$.

Lattices occur in a wide range of mathematical and engineering topics, such as cryptography [Pei14], compression [KDMB02], crystallography [Kit04], and, apparently, digital communications [WSJM11]. A more detailed treatment of lattices and their properties is given in e.g. [CS99].

Channel matrix as the lattice basis. Consider the $\mathcal{J}$-QAM constellation where both the real and imaginary component takes the values $\{-2s+1, -2s+3, -2s+5, \ldots, 2s-1\}$ [2] with $s = \sqrt{\mathcal{J}}$ and $\mathcal{J} = 2^\mu$. We can find two numbers $s \in \mathbb{R}, o \in \mathbb{C}$ such that $\vec{z} = s\vec{d} + o\vec{1} \subset \mathbb{Z}^N + j\mathbb{Z}^N$. Accordingly, the received signal $\vec{y'}$ with

$$\vec{y'} = s\vec{y} + o\mathbf{H}\vec{1} = s\mathbf{H}\vec{d} + \mathbf{H}o\vec{1} + s\vec{w} = \mathbf{H}\vec{z} + s\vec{w} \tag{5.4}$$

consists of points of the lattice with basis $\mathbf{H}$ which are corrupted by AWGN with noise variance $s^2\sigma^2$. Here, s and o serve as (channel-independent) constants to shift the receive points onto the integer lattice with origin $\vec{0}$. Then, the optimal MIMO detection (2.16) in the uncoded case is equivalent to finding the closest point $\mathbf{H}\vec{z}$ of a lattice for a given point $\vec{y'}$. This problem has been shown to be NP-hard [AEVZ02], i.e. no exact algorithm exists that achieves polynomial runtime in any case. However, approximations exist, such as the Schnorr-Euchner enumeration [SE94] which is practically applied in the sphere decoder [SB10, AF16].

In an orthogonal lattice[3], which corresponds to an orthogonal transmission, each component of the N-dimensional data vector $\vec{d}$ is encoded within one dimension of the N-dimensional receive signal space. Hence, ML detection can be easily accomplished. At the downside, if one dimension of the signal space is severely attenuated due to e.g. fading, the data on this dimension is most likely lost. On the other hand, non-orthogonal signalling (i.e. non-orthogonal lattice bases) does not reserve one dimension for one component of $\vec{d}$ but allocates multiple components of $\vec{d}$ onto multiple dimensions of the received signal, creating interference on the one hand, but mitigating deep fades on the other hand.

An important measure for the error probability in the uncoded case is the minimum distance $d_{\min}$ between two adjacent lattice points. Intuitively, if the magnitude of the noise realization for a given received point is smaller than $d_{\min}/2$, the detected point will

[1] If $\mathbf{H}$ is tall, there exists a unitary matrix $\mathbf{U}$ such that $\mathbf{UH}$ has size $N \times N$ without changing the statistical properties of the system.

[2] The constellation diagram can be scaled to have unit energy.

[3] Orthogonal lattices have an orthogonal basis matrix $\mathbf{H}$, i.e. $\mathbf{H}^H\mathbf{H} = \mathrm{diag}(\vec{v})$ where $\vec{v}$ describes the gains in each dimension. The columns $\vec{h}_i$ of $\mathbf{H}$ are orthogonal, i.e. $\vec{h}_i^H\vec{h}_j = \vec{v}_i\delta_{ij}$. As an example, OFDM is orthogonal when the channel is a static multipath channel.

always be correct. If the noise is stronger, detection errors can occur. Due to the linear structure of the lattice, finding $d_{\min}$ is equivalent to finding the shortest vector in a lattice. Unfortunately, this problem is also NP-hard and no analytic solution exists. Nevertheless, $d_{\min}$ can be calculated numerically for small system sizes.

In the coded case, not all combinations of constellation points are allowed. Hence, there will be holes in the lattice, i.e. some points in the lattice are not valid, since they do not correspond to valid codewords. Even though also in this case $d_{\min}$ dictates the error performance, its numerical calculation is more complex since codewords are generally very long. Furthermore, what makes this significantly harder if not unsolvable than in the uncoded case is the fact that usually there is no linear mapping from the payload bits to the transmitted signal, as the bit-to-QAM mapping is a non-linear operation. Therefore, for the following derivation, we resort to the minimum distance in the uncoded case.

Minimum distance of GFDM and OFDM. In the previous section, we have seen that interference can in fact be beneficial for the decoding process. We want to illustrate this observation with the analysis of the probability distribution of the minimum distance $p(d_{\min})$ of a single-antenna OFDM, SC-FDMA and GFDM system. Consider a linear modulation system with frequency domain modulation matrix $\mathbf{M}$ and a diagonal channel in the frequency domain, i.e. a CP is used to diagonalize the channel. The channel is assumed to be Rayleigh fading with a given PDP $\vec{P}$ with normalization $\sum_i P_i = 1$. Hence, a realization of the channel impulse response is given by

$$\vec{h} = \mathrm{diag}(\sqrt{\vec{P}})\vec{n}, \tag{5.5}$$

where $\vec{n} \sim \mathcal{CN}(0, \mathbf{I})$ describes the Rayleigh fading. Then, the noise-free received signal $\vec{Y}$ in the frequency domain is given by

$$\vec{Y} = (\sqrt{N}\mathbf{F}_N \mathrm{diag}(\sqrt{\vec{P}})\vec{n}) \circ \mathbf{M}\vec{d}. \tag{5.6}$$

Consider a system that uses only the first GFDM subcarrier. For an equivalent CP-OFDM system, we have $\mathbf{M} = (\mathbf{I}_M \quad \mathbf{0}_{M\times N-M})^T$, for SC-FDMA we have $\mathbf{M} = (\mathbf{F}_M \quad \mathbf{0}_{M\times N-M})$ and for GFDM we find $\mathbf{M} = \mathbf{F}_N\mathbf{A}$, and $\mathbf{A}$ equals the columns of the GFDM modulation matrix that correspond to the first subcarrier. Note that GFDM with the Dirichlet filter reduces to SC-FDMA. We can determine $p(d_{\min})$ over different fading realizations for each system and for different power delay profiles. The minimum distance is given as the shortest vector in the lattice by

$$d_{\min} = \min\{\|(\mathbf{F}_N \mathrm{diag}(\sqrt{\vec{P}})\vec{n}) \circ \mathbf{M}\vec{d}\| | \vec{d} \in \mathbb{Z}^M + j\mathbb{Z}^M \setminus \{\vec{0}\}\}. \tag{5.7}$$

In the OFDM case, where $\mathbf{M} = \mathbf{I}$, $p(d_{\min})$ follows the distribution of the minimum of M correlated Rayleigh random variables. For uncorrelated Rayleigh variables, this problem is trivially solved [Lee16], but the approach is not easily generalizable to correlated variables. However, numeric approximations of the distribution is straight-forwardly possible. For SC-FDMA and GFDM, no closed-form solution for $p(d_{\min})$ can be found, since no analytic expression for $d_{\min}$ is available. Still, the distribution can be estimated numerically.

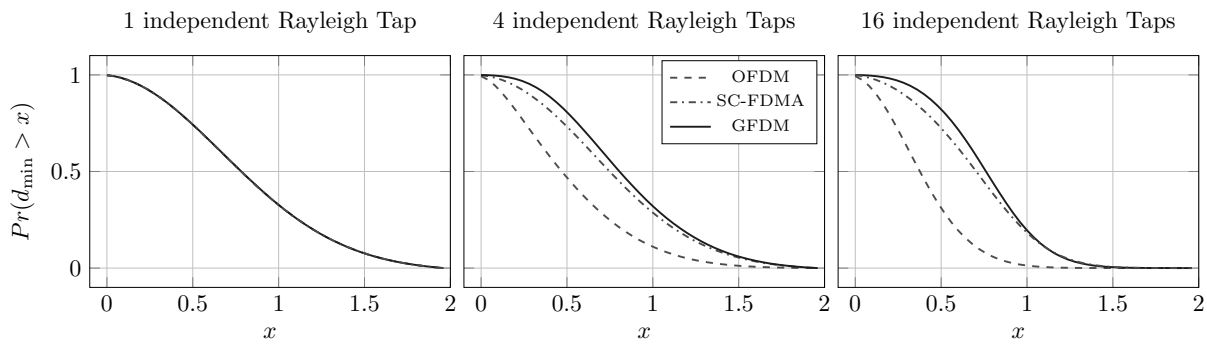

Figure 5.2: Simulation of minimum distance of OFDM, SC-FDMA and GFDM for $N = 16, M = 4$. GFDM uses a RC filter with $\alpha = 1$.

Fig. 5.2 shows the numerically obtained probability densities of $d_{\min}$ for OFDM, SC-FDMA and GFDM for a flat fading and two frequency selective channels. In the flat fading channel[4], we can observe that $p(d_{\min})$ is independent of the modulation matrix. Explaining the equality of SC-FDMA and OFDM is straightforward, since both OFDM and SC-FDMA use a unitary $\mathbf{M}$ which does not change the energy of any transmit vector, i.e. $\|\mathbf{M}\vec{d}\|^2 = \|\vec{d}\|^2$ for all $\vec{d}$ and hence $\|(\mathbf{F}_N \mathrm{diag}(\vec{P})\vec{n}) \circ \mathbf{M}\vec{d}\|^2 = \|(\mathbf{F}_N \mathrm{diag}(\vec{P})\vec{n}) \circ \vec{d}\|$ for a flat channel, i.e. $\vec{P} = \vec{e}_0$, where $\vec{e}_0$ is the first column of the identity matrix.

However, for GFDM $\mathbf{M}$ is not unitary. But, one can show that[5]

$$\min_{\vec{d} \in \mathcal{S}^M \setminus \vec{0}} \|\mathbf{M}\vec{d}\|^2 = \min_{\vec{d} \in \mathcal{S}^M \setminus \vec{0}} \|\vec{d}\|^2$$

and hence the same distribution of $d_{\min}$ as for OFDM is obtained.

In the case of a frequency-selective channel, the situation changes. Now, the channel is not flat, i.e. the channel frequency bins become less correlated, when the PDP becomes longer. In this case, $p(d_{\min})$ for OFDM concentrates around smaller values. Intuitively, we can explain this for the extreme case of $\vec{P} = \frac{1}{\sqrt{N}}\vec{1}$, i.e. all frequency bins are uncorrelated. Then, for the OFDM case the PDF for $d_{\min}$ is given by the distribution of the minimum of M uncorrelated Rayleigh random variables. Certainly, this distribution is more concentrated around smaller values than the distribution of a single Rayleigh variable.

This problem of the reduced $d_{\min}$ for OFDM is created by the fact that in OFDM each frequency bin can be modulated independently, i.e. it can happen that one carrier is severely faded, yielding a small $d_{\min}$. In contrast, both GFDM and SC-FDMA do not allow independent modulation of each frequency bin, due to their modulation matrix $\mathbf{M}$. Intuitively, both systems spread the data over multiple frequency bins, exploiting frequency diversity. Figure 5.3 illustrates this behaviour, where we compare $d_{\min}$ for GFDM and OFDM for a fixed channel realization. The channel realization is deeply faded around the 35th OFDM subcarrier, hence leading to a small $d_{\min}$ for OFDM. In this case, frequency-spreading waveforms such as SC-FDMA or GFDM are more robust against these fades.

[4] The flat fading channel can be seen as a corner case, where the frequency bins are random variables that have 100% correlation, i.e. are all equal.

[5] Intuitively, the minimum energy is obtained, when only one subsymbol is active. Since $\|\vec{g}\|^2 = 1$ the result follows.

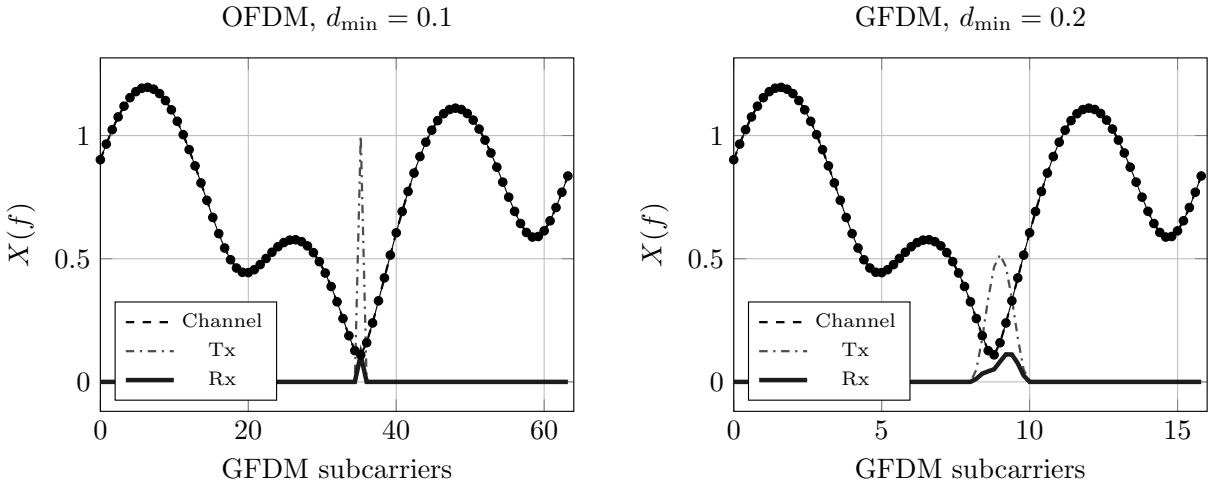

Figure 5.3: Example of $d_{\min}$ for OFDM and GFDM for the same channel realization. $N = 64, M = 4, K = 16$, GFDM uses an RC filter with rolloff $\alpha = 1$. Both systems transmit with unit energy, but OFDM concentrates all energy into one frequency bin, which can happen to be deeply faded. In contrast, GFDM uses wider subcarriers and uses more frequency bins for a single subcarrier. Accordingly, it can harvest frequency diversity and therefore does not equally suffer from the deep fade.

We want to conclude this section by emphasizing that the performed investigations only hold for the uncoded case, i.e. each data point is independent from all others. In the coded case, the situation is different, since already the channel code can exploit diversity that stems from the frequency-selectivity of the channel. Nevertheless, the present investigation shows that the modulation format itself can lead to additional exploitation of frequency diversity and therefore opens the potential to outperform plain OFDM, especially when short code words or high code rate are used and the code diversity is hence limited.

5.2 Successive Interference Cancellation for GFDM

The technique of SIC is well known in diverse detection algorithms, ranging from multi-user detection [WQK+14] to channel estimation [KLF07] or MIMO detection [TV05]. In this section, we introduce a SIC algorithm for MIMO-GFDM detection that uses a sphere-decoder [AF16]to detect each layer. The proposed algorithm greatly outperforms optimal OFDM detectors in the uncoded case, which we can explain by the increased $d_{\min}$ of GFDM as shown in the previous section. However, subsequent analysis of coded performance reveals an inferior performance due to the error propagation of the SIC technique. As such, these findings are a prominent example that basing conclusions on simulation with uncoded transmissions can be very misleading.

In the following, we first introduce the basic algorithm and point out methods to improve its performance. Subsequently, we analyze uncoded and coded performance and give reasons of the great discrepancy between the coded and uncoded performance. This section is based on the author's work in [MGZF15, MZF16b].

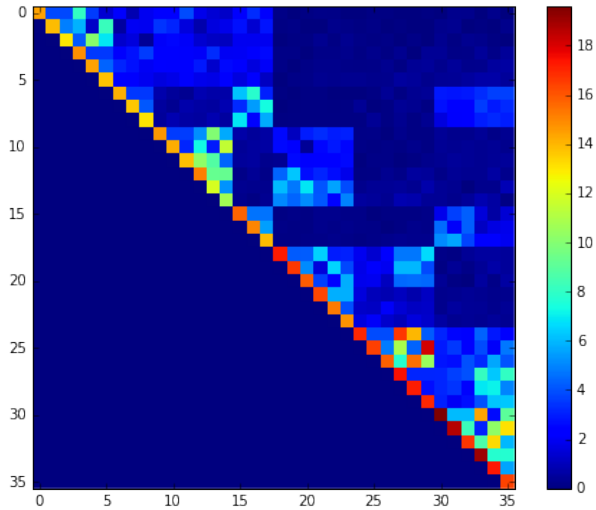

Figure 5.4: Example $\mathbf{R}$ after QR decomposition of equivalent GFDM channel in (5.8). 2×2 MIMO-GFDM system with $K = 6, M = 3, \alpha = 1$. Clearly, the interference is structured in blocks, with the strongest interference appearing along the triangular blocks on the diagonal.

5.2.1 Basic Algorithm Description

The proposed SIC method relies on the sorted MMSE QR decomposition (MMSE-SQRD) [WBKK03] of the equivalent channel matrix, given by

$$\begin{bmatrix} \mathbf{H} \\ \sigma \mathbf{I} \end{bmatrix} = \begin{bmatrix} \mathbf{Q}_1 \\ \mathbf{Q}_2 \end{bmatrix} \mathbf{R}\mathbf{P}^T, \tag{5.8}$$

where the unitary permutation matrix $\mathbf{P}$ denotes the column sorting of $\mathbf{H}$ and $\mathbf{R}$ is upper triangular. Here, $\mathbf{P}$ is designed such that the lowest layers of $\mathbf{R}$ have the largest SNR[WBKK03]. Then, the received signal $\vec{y}$ in (5.2) is multiplied by $\mathbf{Q}_1$, yielding

$$\tilde{y} = \mathbf{R}\tilde{d} + \tilde{w}, \tag{5.9}$$

where $\tilde{d} = \mathbf{P}^T \vec{d}$ and $\tilde{w}$ denotes noise plus remaining interference, since $\mathbf{Q}_1$ is not exactly unitary [WBKK03]. Fig. 5.4 shows an example $\mathbf{R}$ matrix for a 2×2 MIMO-GFDM system. As can be seen, the interference (i.e. the off-diagonal elements of $\mathbf{R}$) is concentrated along the main diagonal. Furthermore, it appears that the interference occurs in blocks of size $M \times M$. However, the interference is structured in a way, that no complete decoupling between parts of the equation system can be achieved.

Optimally, a sphere-decoder could run on the triangular equation system (5.9). However, even though the complexity of modern sphere decoders has been greatly reduced [SB10, AF16], the huge size $N_T N_{on} \times N_T N_{on}$ of (5.9) prohibits a practical application of the sphere decoder to (5.9). Therefore, we have designed an algorithm that takes into account the special structure of $\mathbf{R}$. Given a layer size S, the proposal combines S-dimensional sphere-decoding with SIC between the detected layers [MZF16b, MGZF15]. The idea is that the sphere-decoder completely resolves the interference between the $S \times S$ blocks on the diagonal of $\mathbf{R}$, and the SIC removes this interference from the other layers. With $S = 1$, this algorithm reduces to standard V-BLAST SIC detection [WFGV98] as a corner

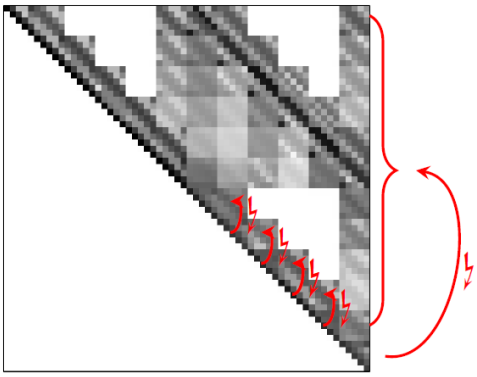

while length($\tilde{y}$)>0 **do**

$\vec{\lambda}_S = \mathrm{SD}(\tilde{y}_S, \mathbf{R}_{S,S}, \sigma^2)$ ▷ Detect last S streams using sphere-decoding. (1)

$\hat{\vec{d}} = \vec{\mathcal{M}}(\vec{\lambda}_S > 0)$ ▷ Hard-decision LLR to QAM mapping. (2)

$\tilde{y} \leftarrow \tilde{y} - \mathbf{R}_{:,S}\hat{\vec{d}}$ ▷ Cancel interference from this layer to upper layers. (3)

$\tilde{y} \leftarrow \tilde{y}_{\bar{S}}$, $\mathbf{R} \leftarrow \mathbf{R}_{\bar{S},\bar{S}}$ ▷ Reduce system size, go to next $M \times M$ layer. (4)

end while.

Figure 5.5: Detection algorithm from [MGZF15]. The subscripts $S, \bar{S}, :$ denote the last S, all but the last S, and all elements of the subscripted object, respectively.

case. On the other hand, when $S = N_T N_{on}$, the system consists only of a single layer, and hence equals the application of the sphere-decoder to the entire system at once.

Fig. 5.5 shows the pseudo-code of the proposed algorithm, that was originally published in the author's publication [MGZF15]. The algorithm starts in step (1) by performing a soft-out sphere decoder (SD) [AF16] operation, estimating the LLR $\vec{\lambda}_S$ of the last μS bits in the system. In step (2) $\vec{\mathcal{M}}(\vec{\lambda}_S > 0)$ maps the detected bits to the closest constellation point (i.e. hard decision) and the cancellation signal is obtained by remodulating the detected constellation symbols via $\mathbf{R}_{:,S}$. Step (3) removes the detected symbols from the received signal and in step (4) the algorithm moves to the next group of S QAM symbols. The algorithm proceeds until all groups have been processed. Eventually, the estimated LLRs are sent to the channel decoder to produce an estimate of the transmitted code word or undergo hard-decision for uncoded evaluation.

5.2.2 Overcoming Error Propagation

As a SIC technique, the proposed algorithm suffers from error propagation [TV05], as erroneously detecting a lower layer impairs detection of upper layers by assuming a wrong cancellation signal. Moreover, as only groups of symbols are detected jointly, not all relations between all symbols are resolved, reducing the diversity of the system. Therefore, two techniques aiming at improving on these problems have been developed and will be described below.

Soft-SIC. The mapping operation in step (2) of Fig. 5.5 considers hard decision of the cancellation signal based on the LLR output of the SD. However, as the LLRs povide information on both the constellation symbol and its accuracy, an improved cancellation

Initialization $\vec{W} = \sigma^2 \vec{1}$
while length($\tilde{y}$)>0 **do**
  $\vec{\lambda}_S = \mathrm{SD}(\tilde{y}_S, \mathbf{R}_{S,S}, \vec{W}_S)$ ▷ Detect last S streams. (1)
  $\vec{\hat{d}}, \vec{\sigma} = \vec{M}(\vec{\lambda}_S)$ ▷ Estimate constellation symbols. (2)
  $\tilde{y} \leftarrow \tilde{y} - \mathbf{R}_{:,S}\vec{\hat{d}}$ ▷ Cancel interference. (3)
  $\vec{W} \leftarrow \vec{W} + \mathrm{diag}(\mathbf{R}_{:,S}\mathrm{diag}(\vec{\sigma})\mathbf{R}_{:,S}^H)$ ▷ Update Noise (4)
  $\tilde{y}, \mathbf{R}, \vec{W} \leftarrow \tilde{y}_{\bar{S}}, \mathbf{R}_{\bar{S},\bar{S}}, \vec{W}_{\bar{S}}$ ▷ Reduce system size. (5)
end while.

Figure 5.6: Soft-SIC demapping algorithm.

signal can be calculated. Furthermore, considering the reliability information from the LLRs, the noise level of the upper layers can be adapted accordingly, as outlined in Fig. 5.6. Let $\lambda_{i,b}$ and $P[b_{i,b} = 1] = \frac{\exp(\lambda_{i,b})}{1+\exp(\lambda_{i,b})}$ be the LLR and probability for the bth bit of the ith QAM symbol in $\hat{\vec{d}}$. Then, considering the bit-to-symbol mapping, $P[\hat{d}_i = s]$ is straightforwardly given for all $s \in \mathcal{S}$ as the product of the bit probabilities. Mean $\bar{d}_i$ and variance σ_i^2 of the ith QAM symbol in $\hat{\vec{d}}$ are given by

$$\bar{d}_i = \sum_{s\in\mathcal{S}} P[\hat{d}_i = s]s \qquad \text{and } \sigma_i^2 = \sum_{s\in\mathcal{S}} P[\hat{d}_i = s]|s - \bar{d}_i|^2. \tag{5.10}$$

Then, the cancellation signal is calculated from the mean $\bar{d}$ of the estimated symbols in step (2) and (3) of Fig. 5.6. Additionally, the uncertainty of the symbols propagates to the upper layers by

$$\mathrm{Cov}[\mathbf{R}_{:,S}(\vec{\hat{d}} - \vec{d})] = \mathbf{R}_{:,S}\mathrm{diag}(\vec{\sigma})\mathbf{R}_{:,S}^H. \tag{5.11}$$

By assuming the errors are uncorrelated, the diagonal of (5.11) needs to be considered as extra noise for the following layers, as done in step (4) of Fig. 5.6. This technique allows the SD to provide more accurate LLR values for higher layers.

K-Best Decoding. The previously proposed algorithm has the fundamental limitation that only a subset of all symbols is jointly detected. Decisions on a lower layer are fixed and will not change when new information from the upper layers is available. Understanding the solution of (5.9) as a tree search, the proposed algorithm divides the tree into layers of depth S. Then, it searches through a single layer, and chooses the best path for this layer as the starting point for the search on the next layer. This principle is equal to the K-best sphere decoding algorithm [GN06], but only keeping the best path (i.e. $K_p = 1$)[6]. Hence, the proposal can be extended to keep a higher number of best paths in the search history, such that the decision on one layer is not final, but can be influenced by higher layers.

The proposed algorithm is shown in Fig. 5.7. The set $\mathcal{L}$ contains all LLR candidate vectors used to calculate the cancellation signal (2). For each of these candidates the SD

[6] To distinguish the number of kept paths from the number of subcarriers of the system, we denote the number of paths by K_p.

Initialization: $\mathcal{L} = \{\}$ ▷ (1)
for $n = \frac{TN_{\text{on}}}{S} - 1$ downto 0 **do**
  $\mathcal{L}' \leftarrow \{\}$
  for all $\vec{\lambda} \in \mathcal{L}$ **do**
    $\hat{\vec{d}} = \vec{M}(\vec{\lambda} > 0)$
    $\tilde{y}' = \tilde{y} - \mathbf{R}_{:,nS:\text{end}}\hat{\vec{d}}$ ▷ (2)
    $\vec{\lambda}_S = \text{SD}(\tilde{y}'_{nS:(n+1)S}, \mathbf{R}_{nS:(n+1)S,nS:(n+1)S})$ ▷ (3)
    Flip unreliable bits in $\vec{\lambda}_S$ and add $[\vec{\lambda}\ \vec{\lambda}_S]$ to $\mathcal{L}'$ ▷ (4)
  end for.
  Reduce $\mathcal{L}'$ based on $d(\tilde{y}_{nS:end}, \mathbf{R}_{nS:\text{end},nS:\text{end}}, \vec{\lambda})$ ▷ (5)
  $\mathcal{L} \leftarrow \mathcal{L}'$
end for.
Keep best element of $\mathcal{L}$.

Figure 5.7: K-best demapping algorithm

is run (3) and its output is added to a new candidate list $\mathcal{L}'$ (4). Furthermore, the sign of the small LLR values, i.e. unreliable bits, in $\vec{\lambda}_S$ are flipped and the resulting LLR vectors are also considered as candidates in $\mathcal{L}'$. After all candidates have been generated, the K candidates with the smallest distance of the received signal to the estimated signal, given by

$$d(\vec{y}, \mathbf{R}, \vec{\lambda}) = \|\vec{y} - \mathbf{R}\vec{\mathcal{M}}(\vec{\lambda} > 0)\|^2, \tag{5.12}$$

are retained in $\mathcal{L}'$ (5). Eventually, the best candidate vector in $\mathcal{L}$ is the final output of the demapping algorithm.

5.2.3 Simulation results

The described demapping algorithm has been evaluated by Monte-Carlo simulations with system parameters from Tab. 5.1. According to the results obtained in Sec. 5.1 wider filters improve frequency diversity and minimum distance. Therefore, two different filter types were investigated. First, a filter with RC spectrum with rolloff $\alpha = 1.0$ was considered. Alternatively, a filter with a RC time-domain function with rolloff $\alpha = 0.1$ [GMM+15] was used, which creates a frequency response which is significantly wider than one subcarrier.

For the channel code, a rate 5/6 WiMax LDPC code was chosen, since it performs well in non-iterative receivers and the GFDM block size was adapted to contain a full LDPC code word of 1344 bits [MZF16b]. The sum product algorithm (SPA) is used for decoding. GFDM was configured according to GFDM type-II, such that an OFDM system which occupies the same bandwidth and time resource is used for benchmarking the system. The OFDM demapping process involved a soft-out SD operation for each subcarrier and is hence optimal for non-iterative receivers. The channel is modeled as a block-fading Rayleigh multipath channel as defined in Sec. 2.2 with the PDP given in Tab. 5.1. In the simulation, we analyzed the performance under three different PDPs. Moreover, perfect CSI and synchronization was assumed at the receiver and the LLR output of the SD was clipped at ± 10.

Table 5.1: System parameters used for the simulation.

	Parameter	Symbol	Value
GFDM	# subsymbols, # subcarriers	M, K	7, 32
	# allocated subcarriers	$\lvert\mathcal{K}\rvert$	16
	Prototype filter 1	$g[n]$	RC FD, $\alpha = 1.0$
	Prototype filter 2	$g[n]$	RC TD, $\alpha = 0.1$
	Group size for joint detection	S	$7 = M$
OFDM	Block length	N	$224 = MK$
	# allocated subcarriers		$112 = M\lvert\mathcal{K}\rvert$
General	CP length	N_{CP}	32
	Bit-mapping	$\mathcal{S}$	64-QAM, gray
	# transmit, receive antennas	T, R	2×2
Channel PDP	Channel 1: Exponential PDP	L_1	12 Taps
	Channel 2: Exponential PDP	L_2	16 Taps
	Channel 3: Uniform PDP	L_3	32 Taps
LDPC Code	Code word length		1344 bits
	Coding Rate		5/6
	Decoding Algorithm		SPA

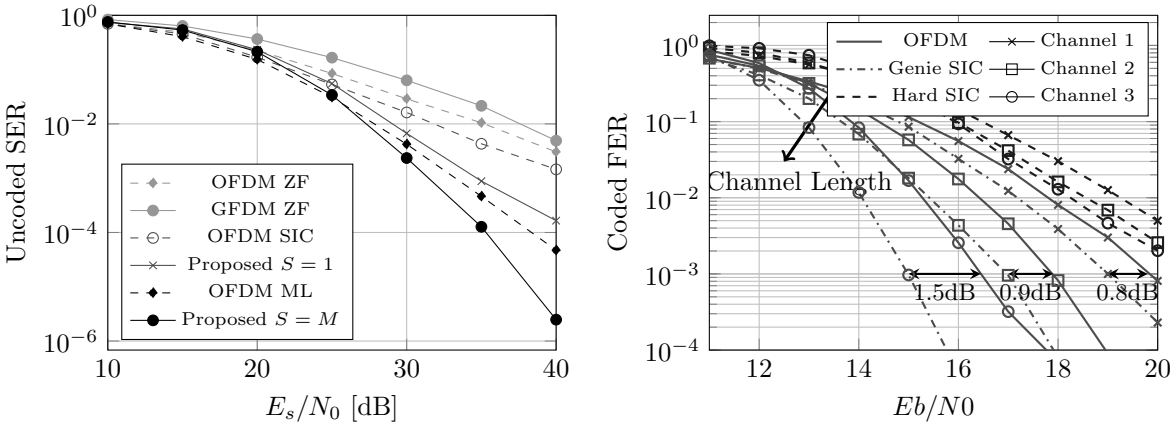

(a) Uncoded performance in Channel 2. **(b)** Coded FER in different channels.

Figure 5.8: Uncoded and coded performance of the proposed algorithm using Hard-SIC with the system configuration from Tab. 5.1 and a RC filter with rolloff $\alpha = 1$.

Uncoded Performance. Fig. 5.8a shows the performance of the proposed algorithm using Hard-SIC in the uncoded case. There, the performance of ZF equalization, pure SIC (i.e. $S = 1$) and the block-wise SD in combination with SIC (i.e. $S = M$) are compared with the respective OFDM performances. As can be seen, with the linear ZF receiver, the 3-dimensional interference of GFDM implies a noise enhancement of roughly $2.5dB$ compared OFDM system which is only impaired by IAI. In contrast, comparing the ML solution of OFDM using a sphere-decoder per OFDM subcarrier with the performance achieved by the proposed MIMO-GFDM detector with $S = M$, we observe a far superior performance of GFDM over OFDM. In fact, GFDM outperforms OFDM by 3dB for an (uncoded) SER of $10^{\cdot -4}$.

We can readily explain the superiority of GFDM with the observed distribution of

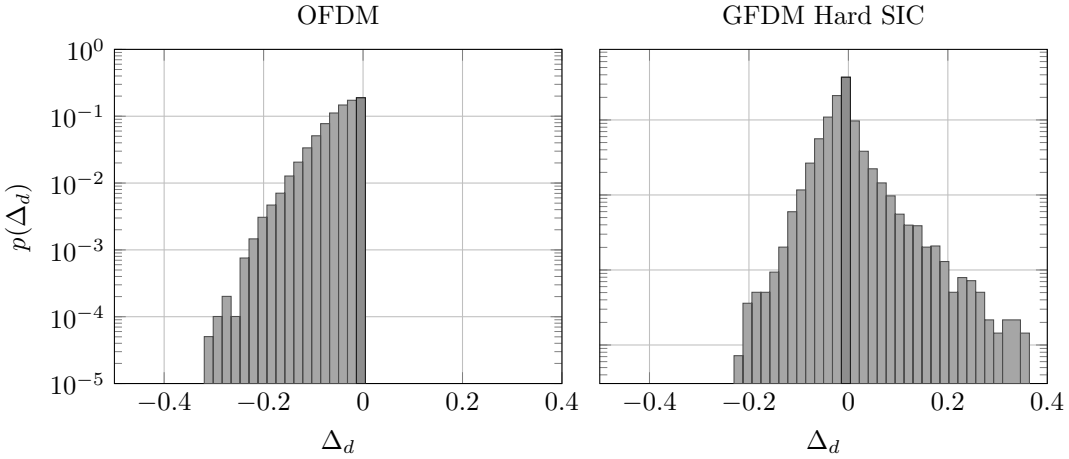

Figure 5.9: Histograms of distance difference for Channel 1 and $E_b/N_0 = 15$dB. The bin for $\Delta_d = 0$ has been marked in blue.

the minimum distance of GFDM and OFDM from Sec. 5.1. and Fig. 5.2. Since the minimum distance limits the achievable performance for a given noise variance, a system that achieves a larger $d_{\min}$ on average will perform superior. On the other hand, $d_{\min}$ does not alone influence the performance. As can be seen, for lower E_S/N_0, OFDM outperforms GFDM in Fig. 5.8a. We can explain this by the error propagation of the SIC method for GFDM, i.e. if a detection error is made in the lower layers, it will propagate to upper layers and impede their detection. Therefore, we again see the two-sidedness of self-interference: If the receiver can accurately resolve the interference (i.e. make correct decisions at the lower layers), performance improves. If it cannot resolve it (e.g. in the lower SNR regions), the self-interference acts similar to additional noise and degrades performance compared to an orthogonal system.

Hard SIC Coded Performance. Encouraged by the promising results in the uncoded transmission from Fig. 5.8a, simulations including soft-out channel decoding were performed. Fig. 5.8b shows the achieved decoding performance in terms of coded FER for the proposed algorithm with $S = M$ in comparison to OFDM. Additionally, the curve labeled *Genie SIC* can be understood as a lower bound on the FER showing the potential of the demapping process without error propagation, i.e. the interference cancellation was assumed to be always correct. As shown, the Hard-SIC proposal achieves poor performance in the coded case compared to the OFDM system. The evaluation has been carried out for different channel conditions. Though the performance of GFDM increases with frequency selectivity, the gap to the OFDM system grows, since the OFDM system harvests frequency diversity through the LDPC code. On the other hand, the Genie SIC curves reveal an increasing potential of the algorithm, if the error propagation could be mitigated.

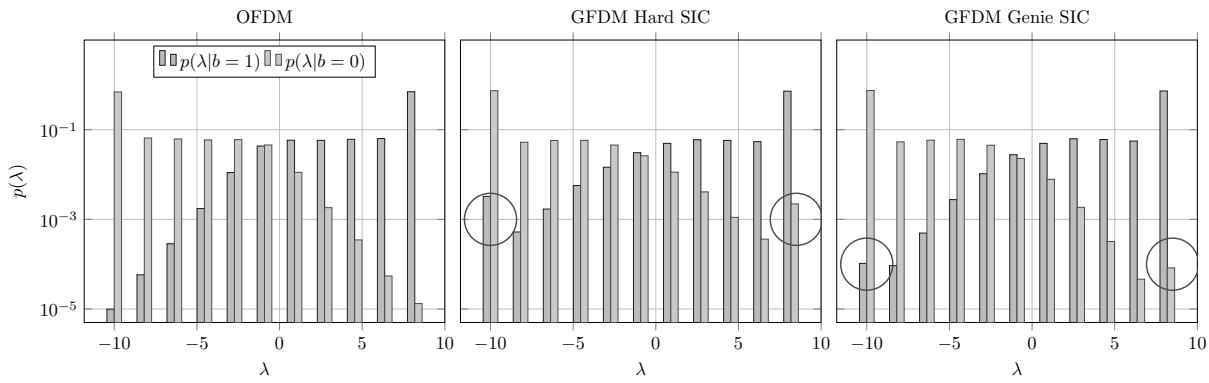

Figure 5.10: Histograms of LLR at demapper output at $E_b/N_0 = 15$dB in Channel 1.

Analysis of Error Propagation. To analyze the error propagation characteristics, we evaluate the metric Δ_d for GFDM and OFDM in the uncoded case, wich is given by

$$\Delta_d = \|\vec{y} - \tilde{\mathbf{H}}\vec{\mathcal{M}}(\vec{\lambda} > 0)\| - \|\vec{y} - \tilde{\mathbf{H}}\vec{d}\|. \tag{5.13}$$

In words, Δ_d equal the difference between two characteristic eucledean distances in the signal space. First, the distance of the received signal to the estimated signal $\|\vec{y} - \tilde{\mathbf{H}}\vec{\mathcal{M}}(\vec{\lambda} > 0)\|$, i.e. the decision made by the demapper, is considered. Second, the distance of the received signal to the transmitted signal $\|\vec{y} - \tilde{\mathbf{H}}\vec{d}\|$, i.e. to the correct decision, is used. Hence, if the decision of the demapper is correct, i.e. $\vec{\mathcal{M}}(\vec{\lambda} > 0) = \vec{d}$, then $\Delta_d = 0$[7]. $\Delta_d < 0$ implies the demapper found a bit combination that is closer to the received signal than the actually transmitted signal. In this case, we know that the ML decision would be an erroneous decision, since there exists an erroneous decision that is closer to the received signal than the correct decision. On the other hand, $\Delta_d > 0$ implies that the demapper could not find the ML solution, as we know that $\tilde{\mathbf{H}}\vec{d}$ is closer to the received signal than the decision made by the demapper.

The histogram for Δ_d was obtained by measuring Δ_d for different channel and noise realizations and calculating the relative frequencies of each bin. The result is shown in Fig. 5.9. As shown, the OFDM demapper always finds the ML solution to (5.1), since $\Delta_d \leq 0$. For GFDM, a significant histogram part relates to $\Delta_d > 0$, indicating that the ML solution was not found. Hence, the coded performance is inferior. But, being in line with Fig. 5.8a, comparing the bin values of both histograms at $\Delta_d = 0$ (blue bar) shows a better uncoded FER of GFDM than OFDM, as the ratio of exactly correct decisions ($\Delta_d = 0$) for GFDM is higher than for OFDM.

In addition, Fig. 5.10 compares the histograms of the demapper LLR output for OFDM and GFDM, where GFDM employs either Hard SIC or Genie SIC. In the plots, $p(\lambda|b = 1)$ describes the histogram of the LLRs that belong to bits with value $b = 1$. Comparing the histogram shape for LLRs with correct sign, no difference can be inferred between OFDM and GFDM. However, looking at LLR with wrong sign, the histogram shapes for GFDM

[7] Practically, this implication can be considered to be an equivalence relation, as it is very unlikely that an erroneous decision will yield an exact match in the distances due to the high dimensionality and randomness of the noise

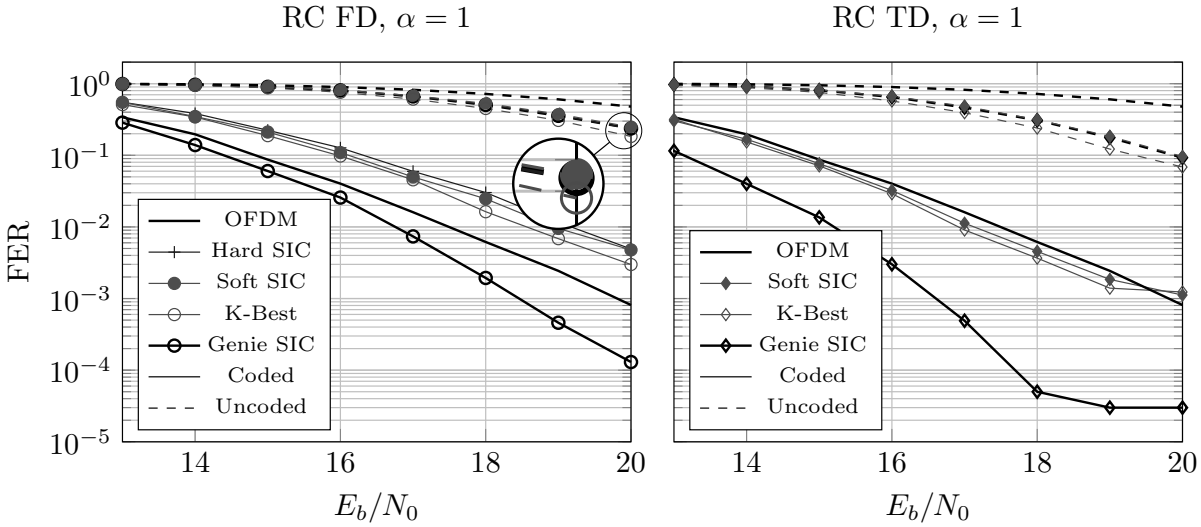

Figure 5.11: FER comparison for the proposed demappers in Channel 1.

and OFDM differ strongly (marked with circles in Fig. 5.10). For GFDM Hard SIC a large amount of LLRs with wrong sign have high magnitudes compared to OFDM. These wrong LLRs can outrule LLRs with correct sign but small magnitude in the decoding process and hence the FER is severely degraded. By intuition, the large LLRs with wrong sign exist mostly due to the error propagation of the SIC. However, the histogram for GFDM Genie SIC, where no error propagation can occur, reveals, that still more high-magnitude wrong-sign LLRs compared to OFDM occur. These exist because only groups of S symbols are jointly detected. Hence, we can infer a significant loss by not jointly tackling ISI, ICI and IAI between all symbols. On the other hand, a full joint detection is computationally infeasible with the present algorithm proposal.

Soft-SIC and K-Best Performance. Finally, Fig. 5.11 shows the FER of the proposals to reduce the effect of error propagation in the system. Again, the OFDM curve serves as a reference. Looking at the uncoded detection performance, Soft SIC, Hard SIC and Genie SIC all achieve the same FER, significantly outperforming OFDM. Remarkably, the K-best detection with 16 candidates achieves even better performance than the Genie SIC, which is explainable by the larger search tree for the detection.

For the coded FER, Soft SIC and K-Best detection improve the decoding performance by $0.2dB$ and $0.5dB$, respectively. in this sense, we believe the massively increased complexity of the K-best detector is not worth the implementation effort. Furthermore, the gap to the OFDM system is not closed when using the filter with RC spectrum (RC FD). Employing a filter with RC impulse response (RC TD) [GMM+15] improves the performance by $\approx 1.8dB$. The wider bandwidth yields stronger ICI, hence linear receivers would yield poorer performance, as was shown in Sec. 2.4.3 for single-antenna systems and in the author's work [MZF16a] for MIMO systems. However, in principle a wider bandwidth yields larger frequency diversity which is explained in Sec. 5.1, which can be harvested by non-linear receivers. For the proposed receiver algorithm, the performance gain can be explained by the fact that for high SNR, already the cancellation signal calculation based

on the uncoded symbols partially correctly cancels the interference and leads to higher diversity. Employing the RC TD filter exhibits an error floor which is because only S symbols are jointly detected. This is even more influential for the RC TD case, since due to higher ICI more symbols overlap in the frequency domain and hence the information loss of jointly detecting only few symbols becomes more significant.

Comparing the Genie SIC curves with the achievable curves of Hard SIC, Soft SIC and K-best shows a great potential if the error propagation could be further mitigated. However, with the restriction of a non-iterative receiver structure, the cancellation signal calculation can only rely on the constellation constraint of the transmitted signal and no coding constraint can be incorporated. This makes it virtually impossible to generate the correct cancellation signal reliably. Moreover, considering groups of only S symbols is not optimal and especially impairs performance with wide-bandwidth filters. On the other hand, employing an iterative receiver structure quickly becomes impractical with the present algorithm, since the successive application of the SD implies both a large latency and computationaly complexity for each iteration. In the following section, we propose a different method for the soft-in soft-out (SISO) demapping of the MIMO-GFDM signal, which is more appropriate for iterative detection.

5.3 Summary

In this chapter, we have derived the linear model for MIMO-GFDM transmission and analyzed the minimum distance of a GFDM and OFDM modulation in the context of the lattice structure of digital modulation. We have found that due to the self-interference and hence frequency-spreading of GFDM the distribution of the minimum distance of GFDM over all channel realizations is shifted towards larger values, compared to OFDM. Therefore, we concluded a larger capacity for GFDM-modulated signals compared to the orthogonal signalling.

Based on this observation, we have proposed and analyzed an algorithm for detection of spatially multiplexed GFDM streams and compared its performance against state-of-the-art MIMO-OFDM receivers. Namely, we have analyzed a non-iterative detection algorithm that based on the combination of sphere-decoding with SIC which aims at achieving the ML performance in the uncoded case. We showed that the proposal significantly outperforms optimal OFDM detection in the uncoded case, however the inherent error propagation of the SIC component degraded coded performance, rendering the approach dull for practical applications. Particularly, our findings emphasize the necessity of analyzing coded performance, since extrapolating results from uncoded performance simulations can be very misleading. Driven by our findings, we conclude that the constellation constraint alone is not sufficient to reliably resolve the self-interference of the non-orthogonal system. Accordingly, in the following chapter we will present and analyze an iterative detection algorithm that aims to achieve the coded ML performance.

Chapter 6

Iterative Detection for Spatially Multiplexed GFDM

As was shown in the previous chapter, relying solely on the constellation constraint for resolving the self-interference does not yield acceptable performance compared to an orthogonal system. Therefore, in this chapter we propose an iterative receiver algorithm for MIMO-GFDM that incorporates the coding constraint into the demapping operation. In Sec. 2.3 the concept of iterative detection has already been mentioned. Briefly, the idea is to provide a-priori information about the probability of different constellation symbols from the decoder to the demapper. The theory that evolves around iterative receiver structures is vast and is actively researched in both classical works [Ber93, Bri01] as well as in timely literature [YH15]. In this thesis, we focus on the application of iterative receiver algorithms for MIMO-GFDM detection and only shortly describe the necessary basics of iterative detection.

6.1 Iterative MIMO Detection

An optimal receiver algorithm in terms of the ML criterion finds the codeword that achieves the minimum distance to the received signal according to (2.16). However, in a reasonable code the huge amount of possible codewords inhibits a brute-force solution to (2.16). Instead, as was shown in Sec. 2.3, the processing of a received signal is split into two blocks, namely the demapper and the decoder. In a non-iterative receiver, the received signal is first processed by the demapper to create an initial guess on the transmitted codeword, which is subsequently improved by the channel decoder. The idea of iterative detection is to understand the combination of the coding and the constellation constraint as a serially concatenated code [BDMP98], which can be efficiently decoded by alternately decoding both codes and exchanging information between them. Therefore, we feed back the information from the channel decoder into the demapper to refine the constellation constraint (Fig. 6.1). This way, a loop between demapper and decoder is obtained, which should optimally converge to the global optimum of (2.16).

Two general theoretical tools exist in the literature that are used to analyze the convergence performance and criteria of iterative decoding. First, one could model the decoding

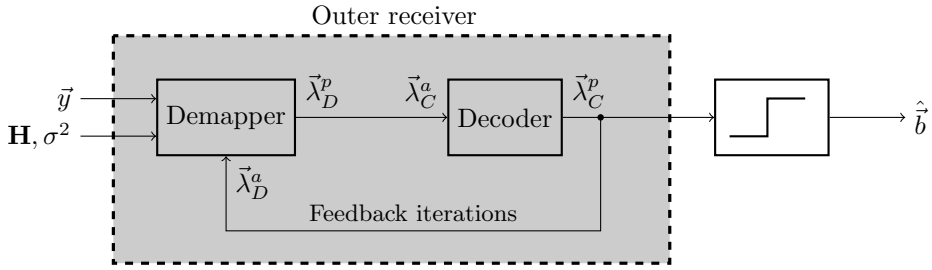

Figure 6.1: Schematic representation of an iterative receiver with SISO demapper and SISO decoder. Note that this generic diagram does not consider the difference between extrinsic and intrinsic information and assumes that the required measures are calculated within the demapper and decoder blocks.

process as a discrete-time nonlinear dynamic system, as was shown in [Ric00b]. Second, density evolution can be used for the analysis, as was e.g. shown in [RU00, RU01]. However, the applicability of these tools is often limited to simple cases to be analytically tractable. To get insights into more complex systems, the extrinsic information transfer (EXIT) chart analysis aims to track the density evolution by a one-dimensional parameter [tB99b]. However, the accuracy of these methods degrades for short code words or more complex systems. As such, very few general results are available to predict and analyze the convergence behaviour. Rather, most insights base on empirical successes of different algorithms. In this work, we used the one-dimensiomal EXIT chart to get some insights into the convergence behaviour of the proposed algorithm.

The central components for iterative detection are the soft-in soft-out (SISO) demapper and SISO channel decoder. Both blocks receive soft-information about the probability of certain bits from a previous processing step and return soft-information about these bits that has been improved by either the constellation (the *SISO demapper*) or the code constraint (the *SISO decoder*). Apparently, the SISO demapper needs to be adapted to the signal modulation, whereas the SISO decoder needs to be adapted to the channel code. Hence in the following, we focus on the design of a SISO demapper for the MIMO-GFDM system and use state-of-the-art channel decoding algorithms for the SISO channel decoder.

6.2 Iterative MMSE-PIC Detection for MIMO-GFDM

The SISO demapping using linear MMSE estimation has been initially proposed in [WV99] which exhibited a very high complexity as it required a matrix inversion for each element in $\vec{d}$. In this subsection, we present the principles of MMSE-PIC demapping as a classic interference cancellation scheme. Consider the linear model $\vec{y} = \mathbf{H}\vec{d} + \vec{w}$. We model $\vec{d}$ as a Gaussian random variable with a known mean $\vec{\mu}_d^a$ and variance Σ_d^a.[1] In the framework of parallel interference cancellation (PIC) of [WV99], the detection focuses on the nth element d_n of $\vec{d}$ and assumes all other elements of $\vec{d}$, denoted by $\vec{d}_{\backslash n}$, are interfering terms.

[1] Knowledge of mean and variance of $\vec{d}$ is commonly obtained from the SISO channel decoder.

This leads to a reformulation of the linear model to

$$\vec{y} = \vec{h}_n d_n + \mathbf{H}_{\backslash n}\vec{d}_{\backslash n} + \vec{w}, \tag{6.1}$$

where $\vec{h}_n$ denotes the nth column of $\mathbf{H}$, and $\mathbf{H}_{\backslash n}$ equals $\mathbf{H}$ without the nth column. Then, the PIC yields the signal $\vec{y}_n$ given by

$$\vec{y}_n = \vec{y} - \mathbf{H}_{\backslash n}[\vec{\mu}_d^a]_{\backslash n} = \vec{h}_n d_n + \underbrace{\mathbf{H}_{\backslash n}(\vec{d}_{\backslash n} - [\vec{\mu}_d^a]_{\backslash n}) + \vec{w}}_{\tilde{w}}, \tag{6.2}$$

where $[\vec{\mu}_d^a]_{\backslash n}$ denotes $\vec{\mu}_d^a$ without the nth element and $\tilde{w}$ models noise-plus-interference with variance $\mathbf{H}\Sigma_d^a\mathbf{H}^H + \sigma^2\mathbf{I}$. Based on (6.2), an LMMSE estimation for d_n is performed, which apparently requires an $N \times N$ matrix inversion for each element of $\vec{d}$ as has been proposed in [WV99]. Later on, [SFS11] and [ALA14] reduced the complexity to require only a single $N_{on} \times N_{on}$ matrix inversion. In [MZF16a], we have shown that this process is equivalent to a single LMMSE estimation with a-priori knowledge on $\vec{d}$. This finding allows to perform the MMSE-PIC demapping for MIMO-GFDM with low complexity based on sparse matrix factorizations. However, before we can dive into the details of the proposed technique, we need to introduce an unbiased relative of the common LMMSE estimator, which will be used in the proposed demapper.

6.2.1 Component-wise conditionally unbiased (CWCU) LMMSE estimation

We denote with Θ_x the (conventional) LMMSE estimator which calculates an estimate of $\vec{x}$ from the measurement $\vec{y}$ based on the linear model $\vec{y} = \mathbf{H}\vec{x} + \vec{w}$, where we have a-priori knowledge on $\vec{x}$ and $\vec{w}$ as

$$\vec{x} \sim \mathcal{CN}(\vec{\mu}_x^a, \Sigma_x^a) \qquad \vec{w} \sim \mathcal{CN}(\vec{0}, \Sigma_w^a). \tag{6.3}$$

Let (η_x^p, Λ_x^p) denote the LMMSE estimate and error variance of this estimate for $\vec{x}$ and denote the LMMSE estimation operation by

$$(\vec{\eta}_x^p, \Lambda_x^p) = \Theta_x[\vec{y} = \mathbf{H}\vec{x} + \vec{w}, \mathcal{CN}(\vec{\mu}_x^a, \Sigma_x^a), \mathcal{CN}(\vec{0}, \Sigma_w^a)]. \tag{6.4}$$

Here, the first, second and third arguments to Θ_x are the linear model with known $\vec{y}$ and $\mathbf{H}$, the a-priori information on $\vec{x}$ and the a-priori information on the noise $\vec{n}$, respectively. Then, Θ_x generates the LMMSE estimate and error covariance matrix by the common equations for the LMMSE estimation:

$$\vec{\eta}_x^p = \vec{\mu}_x^a + \Sigma_x^a\mathbf{H}^H(\mathbf{H}\Sigma_x^a\mathbf{H}^H + \Sigma_w^a)^{-1}(\vec{y} - \mathbf{H}\vec{\mu}_x^a) \tag{6.5}$$

$$\Lambda_x^p = \Sigma_x^a - \Sigma_x^a\mathbf{H}^H(\mathbf{H}\Sigma_x^a\mathbf{H}^H + \Sigma_w^a)^{-1}\mathbf{H}^H\Sigma_x^a. \tag{6.6}$$

This estimation is conditionally biased [Kay93] since $E[\vec{\eta}_x^p|\vec{x}] \neq \vec{x}$. This is due to the fact that the effective channel matrix after filtering, i.e. $\Sigma_x^a\mathbf{H}^H(\mathbf{H}\Sigma_x^a\mathbf{H}^H + \Sigma_w^a)^{-1}\mathbf{H}$, does not have a unit diagonal.

In the following we summarize equations for an unbiased LMMSE estimator, namely the component-wise conditionally unbiased (CWCU) LMMSE estimator [HL15, HLH17]. We let (μ_x^p, Σ_x^p) denote the CWCU LMMSE estimate and error variance of this estimate for $\vec{x}$ and denote the CWCU LMMSE estimation operation by

$$(\vec{\mu}_x^p, \Sigma_x^p) = \Phi_x[\vec{y} = \mathbf{H}\vec{x} + \vec{n}, \mathcal{CN}(\vec{\mu}_x^a, \Sigma_x^a), \mathcal{CN}(\vec{0}, \Sigma_w^a)] \tag{6.7}$$

$$\text{where } \vec{\mu}_x^p = \vec{\mu}_x^a + \frac{\mathbf{H}^H(\mathbf{H}\Sigma_x^a\mathbf{H}^H + \Sigma_w)^{-1}(\vec{y} - \mathbf{H}\vec{\mu}_x^a)}{\text{diag}[\mathbf{H}^H(\mathbf{H}\Sigma_x^a\mathbf{H}^H + \Sigma_w^a)^{-1}\mathbf{H}]} \tag{6.8}$$

$$\text{and diag}(\Sigma_x^p) = \frac{\vec{1}}{\text{diag}[\mathbf{H}^H(\mathbf{H}\Sigma_x^a\mathbf{H}^H + \Sigma_w^a)^{-1}\mathbf{H}]} - \text{diag}[\Sigma_x^a]. \tag{6.9}$$

For the CWCU estimator, we only provide a simple form for the diagonal elements of the a-posteri covariance matrix Σ_x^p of $\vec{x}$. We can ignore off-diagonal elements since considering the diagonal of the covariance is sufficient in the present analysis. However, in general this does not mean that the CWCU estimation provides uncorrelated estimates. More details about CWCU estimation, including the exact expression for the error covariance matrix Σ_x^p can be found in [HLH17].

6.2.2 SISO LMMSE Demapping

Based on the derivations of Wang [WV99], Studer [SFS11] and Auras [ALA14], we showed in [MZF16a] that the core operation of the minimum mean squared error with parallel interference cancellation (MMSE-PIC) demapper is equivalent to a simple CWCU LMMSE estimation that takes a-priori information from the channel decoder into account. The details of this derivation are presented in [MZF16a] and are omitted in the present work. Instead, only the final expressions are shown. The overall SISO demapping operation can be split into 3 steps:

1. *Soft-modulating the LLR from the channel decoder to soft QAM constellation symbols.* Let $b_{s,b} \in \{0, 1\}$ be the bth bit of the sth constellation symbol and let its a-priori information be encoded in the LLR value $\lambda_{s,b}^A$ with $Pr[b_{s,b} = 1] = \frac{\exp(\Lambda_{s,b}^A)}{1+\exp(\lambda_{s,b}^A)}$. Then, mean and variance of the a-priori constellation symbols are given by

$$\begin{aligned}(\vec{\mu}_d^a)_s &= \sum_{d\in\mathcal{S}} Pr[d_s = d]d = \sum_{d\in\mathcal{S}}\prod_b Pr[b_{s,b} = \mathcal{M}_b^{-1}(d)]d \\ (\Sigma_d^a)_{ss} &= \sum_{d\in\mathcal{S}} Pr[d_s = d]\|d - (\vec{\mu}_d^a)_s\|^2,\end{aligned} \tag{6.10}$$

   where $Pr[d_s = d]$ is calculated from the product of the corresponding $Pr[b_{s,b} = \mathcal{M}_b^{-1}(d)]$ and the inverse QAM-to-bit mapping $\mathcal{M}_b^{-1}(d)$ yields the bth bit of the complex constellation symbol d. In the initial iteration no channel decoder feedback is available and hence $\vec{\mu}_d^a = 0$ and $\Sigma_d^a = \mathbf{I}$.

2. *Refining the constellation symbols* by performing CWCU LMMSE estimation with the received signal

$$(\vec{\mu}_d^p, \Sigma_d^p) = \Phi_d[\vec{y} = \mathbf{H}\vec{d} + \vec{w}, \mathcal{CN}(\vec{\mu}_d^a, \Sigma_d^a), \mathcal{CN}(\vec{0}, \sigma^2\mathbf{I})]. \tag{6.11}$$

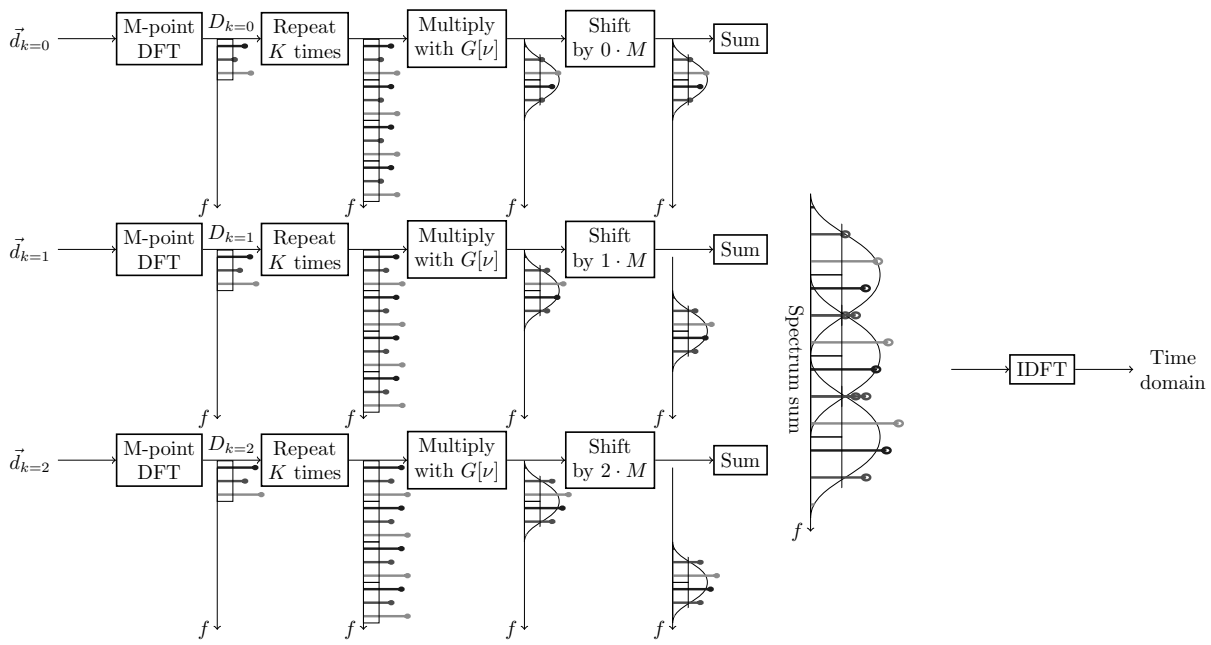

Figure 6.2: Interference structure of data in frequency domain. After the M-point DFT on subcarrier k, the data is repeated K times, windowed by $G[\nu]$ and shifted by kM to the corresponding subcarrier frequency. Eventually, the signals from all carriers are summed to yield the overall frequency domain transmit signal.

3. *Demapping the constellation symbols to distinct bit probabilities* using the common soft-out QAM demapper (2.25) from Sec. 2.3. Afterwards, the estimated LLRs are sent to the channel decoder to estimate the transmitted code word.

6.2.3 Factorization of the channel matrix

In [MZF16a], we presented a method to perform the SISO MMSE-PIC demapping operation by exploiting the band-diagonal structure of the equivalent channel that achieved a complexity order $\mathcal{O}(K_{on}M^3N_T^3)$, i.e. the respective complexity grew linear with the number of allocated subcarriers, but was cubic with the number of subsymbols in the GFDM block. For an equivalent OFDM system, the complexity would be $\mathcal{O}(KMN_T^3)$, since for each of the KM subcarriers, an $N_T \times N_T$ full matrix inversion needs to be performed. Hence, it is desirable to further reduce the complexity of the MMSE-PIC demapping for MIMO-GFDM systems. Moreover, the OFDM solution can be easily parallelized since each carrier can be treated independently, whereas the GFDM solution treats the entire system (6.11) at once, making high-level parallelism difficult to achieve. This can lead to an increased latency in the demodulation when implemented in real-time. In the following, we will derive an algorithm that approximates the operation in (6.11) with a complexity of order that is linear in K and quasi-linear in M and which supports high-level parallelism.

General principle. The basic idea of the complexity reduction is based on the fact that the linear MMSE demapper assumes that both its input and its output are continuous, Gaussian random variables with some known distribution. Hence, for the LMMSE

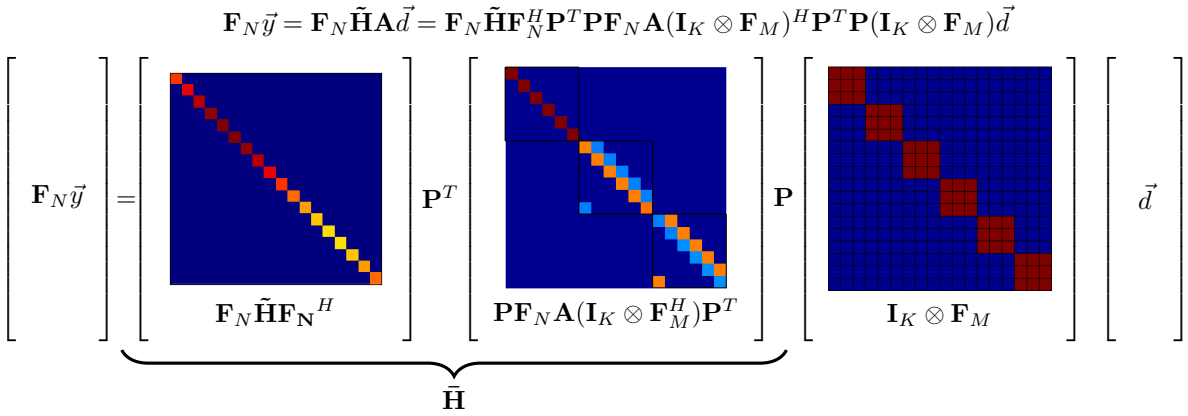

Figure 6.3: Factorized equation system in the noiseless case with $\mathbf{A}_f = \mathbf{F}_N\mathbf{A}(\mathbf{I}_K \otimes \mathbf{F}_M^H)$ for $K = 6, M = 3, \alpha = 1$. The unitary matrix $\mathbf{P}$ is defined as the $N \times N$ permutation matrix that fulfills $\text{vec}(\mathbf{X}^T) = \mathbf{P}\text{vec}(\mathbf{X})$ for all $K \times M$ matrices $\mathbf{X}$.

demapper, it does not matter, if the estimate is actually discrete (i.e. discrete constellation symbols) or not. Since a unitary transform $\mathbf{U}$ transforms i.i.d. Gaussians $\vec{d}$ into i.i.d. Gaussians $\vec{D}$, the LMMSE estimation can be separated into the estimation of $\mathbf{D}$ with subsequent transformation of $\vec{D}$ to $\vec{d}$ via the adjoint of $\mathbf{U}$. If it turns out that the estimation of $\vec{D}$ is easier to accomplish than directly estimating $\vec{d}$, a complexity reduction can be achieved[2].

Interference structure in DFT-spread data domain. To understand how this idea can be applied to the present system, we have to understand the interference structure of GFDM in the DFT-spread data domain. Consider the frequency domain transmitter implementation (2.37), which is illustrated in Fig. 6.2. As is shown, only subsets of the DFT-spread symbols $\{\mathbf{F}_M\vec{d}_k\}_k$ interfer with each other, depicted with different colors (i.e. only bins of the same color interfer). Hence, each color corresponds to a separate equation system. Moreover, since the frequency bins overlap only from adjacent carriers, these equation systems exhibit a bidiagonal structure. For frequency bins in the center of the carriers, the corresponding equation system even becomes diagonal, since depending on the filter rolloff, not all bins overlap. A subsequent multipath channel does not alter this structure since it becomes diagonal in the frequency domain. Fig. 6.3 illustrates the structure of the linear system when $\mathbf{A}$ is factorized according to this proposal.

Extension to MIMO-GFDM. The previous system factorization has been described in the context of single-antenna systems. The extension to the MIMO case is straight-

[2] Given that the operation $\mathbf{U}^H\vec{D}$ can be calculated efficiently

forward, by transforming (5.2) into the frequency domain and writing

$$(\mathbf{I}_{N_R} \otimes \mathbf{F}_N)\vec{y} = \begin{pmatrix} \mathbf{H}_{11} & \dots & \mathbf{H}_{1N_T} \\ \vdots & \ddots & \vdots \\ \mathbf{H}_{N_R1} & \dots & \mathbf{H}_{N_RN_T} \end{pmatrix} (\mathbf{I}_T \otimes \mathbf{F}_N\mathbf{A})\vec{d} + \vec{w} \tag{6.12}$$

$$= \underbrace{\begin{pmatrix} \mathbf{H}_{11} & \dots & \mathbf{H}_{1N_T} \\ \vdots & \ddots & \vdots \\ \mathbf{H}_{N_R1} & \dots & \mathbf{H}_{N_RN_T} \end{pmatrix} (\mathbf{I}_T \otimes \mathbf{A}_f)}_{\tilde{\mathbf{H}}} \vec{D} + \vec{w} = \bar{\mathbf{H}}\vec{D} + \vec{w}, \tag{6.13}$$

with $\vec{D} = (\mathbf{I}_{N_T} \otimes (\mathbf{F}_M \otimes \mathbf{I}_K))\vec{d}$ being the DFT-spread data, i.e. the M-point DFT of the constellation points on each carrier. Then, $\bar{\mathbf{H}}$ in (6.13) is equivalent to $\bar{\mathbf{H}}$ in Fig. 6.3, however each non-zero element of $\bar{\mathbf{H}}$ in Fig. 6.3 would be replaced by a $N_R \times N_T$ non-zero matrix due to the inter-antenna interference.

Three-step LMMSE estimation. We are now ready to formulate the LMMSE estimation based on the factorized system. The ultimate goal is to obtain the CWCU estimate of $\vec{d}$, given by

$$(\vec{\mu}_d^p, \Sigma_d^p) = \Phi_d[\vec{y} = \mathbf{H}\vec{d} + \vec{w}, \mathcal{CN}(\vec{\mu}_d^a, \Sigma_d^a), \mathcal{CN}(\vec{0}, \sigma^2\mathbf{I})], \tag{6.14}$$

which can be achieved with complexity $\mathcal{O}(KM^3N_T^3)$ by directly solving (6.14) as shown in Sec. 2.4.3 and [MZF16a]. However, instead of directly estimating $(\vec{\mu}_d^p, \Sigma_d^p)$ in (6.14), we resort to the DFT-spread data $\vec{D} = \mathbf{U}\vec{d}$ with $\mathbf{U} = \mathbf{I}_{N_T} \otimes (\mathbf{F}_M \otimes \mathbf{I}_K)$ (cf. (6.13)). Accordingly, the a-priori mean $\vec{\mu}_D^a$ and covariance Σ_D^a of $\vec{D}$ are given by

$$\vec{\mu}_D^a = \mathbf{U}\vec{\mu}_d^a, \qquad \Sigma_D^a = \mathbf{U}\Sigma_d^a\mathbf{U}^H. \tag{6.15}$$

We can now get the CWCU estimate of $\vec{D}$ from

$$(\vec{\mu}_D^p, \Sigma_D^p) = \Phi_D[\vec{y} = \bar{\mathbf{H}}\vec{D} + \vec{w}, \mathcal{CN}(\vec{\mu}_D^a, \Sigma_D^a), \mathcal{CN}(\vec{0}, \sigma^2\mathbf{I}], \tag{6.16}$$

Under the constraint that Σ_D^a is a diagonal matrix and due to the GFDM interference structure in Fig. 6.3, the equation system in (6.16) decays into M band-diagonal systems each of size N_TK_{on} where the (one-sided) bandwidth is N_T. Furthermore, we can show that with a diagonal Σ_D^a we have (proof see appendix)

$$(\eta_d^p, \Lambda_d^p) = \Theta_d[\vec{\mu}_D^p = \mathbf{U}\vec{d} + \vec{w}, \mathcal{CN}(\vec{\mu}_d^a, \Sigma_d^a), \mathcal{CN}(\vec{0}, \Sigma_D^p)], \tag{6.17}$$

i.e. the (biased) a-posteriori LMMSE estimate of $\vec{d}$ can be calculated from the CWCU a-posteriori LMMSE estimate of $\vec{D}$ with the linear model $\vec{\mu}_D^p = \mathbf{U}\vec{d} + \vec{\eta}$, where $\vec{\eta}$ contains the uncertainty of the a-posteriori $\vec{D}$. By analogy, the final, a-posteriori CWCU estimate for $\vec{d}$ can be calculated by

$$(\vec{\mu}_d^p, \Sigma_d^p) = \Phi_d[\vec{\mu}_D^p = \mathbf{U}\vec{d} + \vec{\eta}, \mathcal{CN}(\vec{\mu}_d^a, \Sigma_d^a), \mathcal{CN}(\vec{0}, \Sigma_D^p)]. \tag{6.18}$$

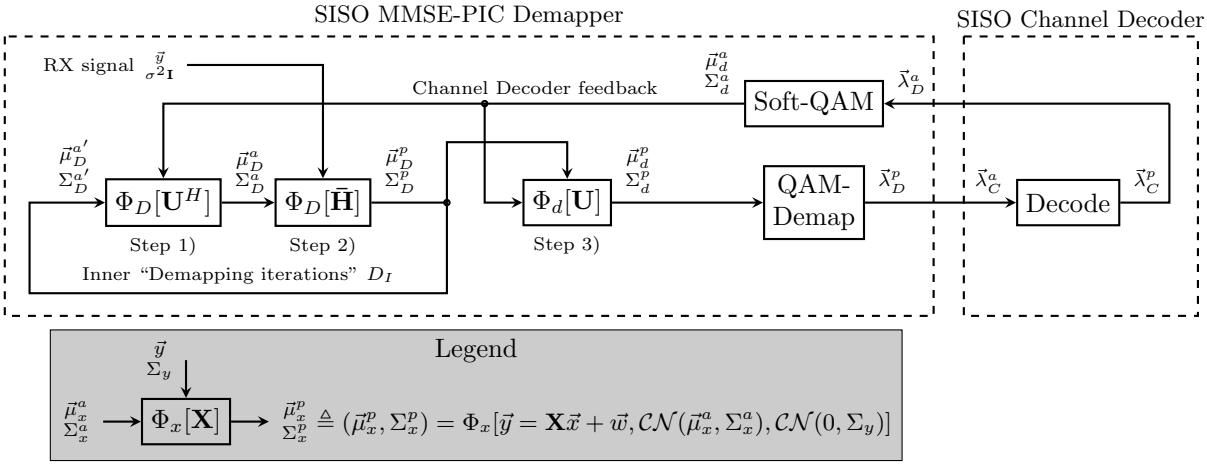

Figure 6.4: Block diagram of the 3-step MMSE estimation process in combination with channel decoder. Using the information from the channel decoder, $(\vec{\mu}_d^a, \Sigma_d^a)$ is generated by soft-modulating the respective a-posteriori LLRs as in (6.10). Then, this information is used to acquire $(\vec{\mu}_D^a, \Sigma_D^a)$ in step 1) which is in turn used to gain improved knowledge $(\vec{\mu}_D^p, \Sigma_D^p)$ in step 2). Finally, this information is transformed to $(\vec{\mu}_d^p, \Sigma_d^p)$ in step 3) and forwarded to the Soft QAM demapper and the channel decoder, closing the iteration loop.

The above derivation assumes that the covariance matrix Σ_D^a is diagonal, which requires the variances of Σ_d^a to be equal on one subcarrier. Naturally, this constraint is violated after feedback information from the channel decoder is incorporated into the demapping process. In this case, by analogy to the estimation of $(\vec{\mu}_d^p, \Sigma_d^p)$ from $(\vec{\mu}_D^p, \Sigma_D^p)$ in (6.18), we can perform CWCU LMMSE estimation of $(\vec{\mu}_D^a, \Sigma_D^a)$ from the a-priori knowledge $(\vec{\mu}_d^a, \Sigma_d^a)$, given by

$$(\vec{\mu}_D^a, \Sigma_D^a) = \Phi_D[\vec{\mu}_d^a = \mathbf{U}^H \vec{D} + \vec{\eta}, \mathcal{CN}(\vec{\mu}_D^{a'}, \Sigma_D^{a'}), \mathcal{CN}(\vec{0}, \Sigma_d^a)]. \tag{6.19}$$

Here, $(\vec{\mu}_D^{a'}, \Sigma_D^{a'})$ is some a-priori knowledge on the distribution of $\vec{D}$. In the simplest case we can use $(\vec{\mu}_D^{a'}, \Sigma_D^{a'}) = (\vec{0}, \mathbf{I})$. Accordingly, we can split the overall SISO LMMSE demapping detection process into 3 steps, which are also illustrated in Fig. 6.4:

1. Calculate $(\vec{\mu}_D^a, \Sigma_D^a)$ as the CWCU LMMSE estimate of $\vec{D}$ from the model $\vec{\mu}_d^a = \mathbf{U}^H D + \vec{\eta}$, $\vec{\eta} \sim \mathcal{CN}(\vec{0}, \Sigma_d^a)$ and $(\vec{\mu}_D^{a'}, \Sigma_D^{a'})$.

2. Calculate $(\vec{\mu}_D^p, \Sigma_D^p)$ as the CWCU LMMSE estimate of $\vec{D}$ from the received signal $\vec{y} = \bar{\mathbf{H}}\vec{D} + \vec{w}$ and $(\vec{\mu}_D^a, \Sigma_D^a)$.

3. Calculate $(\vec{\mu}_d^p, \Sigma_d^p)$ as the CWCU LMMSE estimate of $\vec{d}$ from the model $\vec{\mu}_D^p = \mathbf{U}\vec{d} + \vec{\eta}$, $\vec{\eta} \sim \mathcal{CN}(\vec{0}, \Sigma_D^p)$ and $(\vec{\mu}_d^a, \Sigma_d^a)$.

We want to emphasize that, despite this treatment focuses on the application to GFDM, the proposed 3-step estimation technique to first estimate DFT-spread data symbols can readily be employed for other non-orthogonal waveforms with localized ICI which obey the linear model (5.1) as e.g. FBMC or CB-FMT. For the case of no a-priori knowledge, this has been demonstrated in [ZMMF17]. The present extension of transforming

a-priori knowledge from the time to the frequency domain and vice versa can be straightforwardly applied to other waveforms.

Note, that in case of $\mathbf{U}^H\Sigma_d^a\mathbf{U}$ being diagonal, the CWCU LMMSE estimate of $(\vec{\mu}_D^a, \Sigma_D^a)$ in (6.19) and the direct transform from time to frequency in (6.15) are equivalent. However, in case of Σ_D^a not being diagonal, the LMMSE estimation process tends to produce less correlated estimates, compared to the operation in (6.15) and hence provides more decoupled values to step 2). Nevertheless, the final LMMSE estimate of $\vec{d}$ will not be exact due to ignored correlation between frequency-domain data $\vec{D}$. In order to mitigate this problem, it is possible to perform D_I inner demapping iterations between steps 1) and 2), where the output $(\vec{\mu}_D^p, \Sigma_D^p)$ of step 2) can serve as a-priori knowledge $(\vec{\mu}_D^{a'}, \Sigma_D^{a'})$ for step 1) (see Fig. 6.4). This way, the estimation performance can be improved, at the cost of increased complexity. The obtained simulation results will be presented below in Sec. 6.3.

6.2.4 Low-Complexity Approximation

We have separated the estimation process into smaller steps of decoupled linear equation systems. Therefore, the possibility for high-level parallelism in the implementation is already achieved. On the other hand, the solution of the equation systems can still require high computational efforts, which we investigate in the following section.

Steps 1) and 3): Transforming frequency to time-domain data and vice versa. Initially, in (6.19) in step 1) a CWCU LMMSE estimation of the frequency domain data based on the time-domain data is to be calculated by

$$\begin{aligned}\vec{\mu}_D^a &= \vec{\mu}_D^{a'} + \frac{(\Sigma_D^{a'} + \mathbf{U}\Sigma_d^a\mathbf{U}^H)^{-1}(\mathbf{U}\vec{\mu}_d^a - \vec{\mu}_D^{a'})}{\operatorname{diag}((\Sigma_D^{a'} + \mathbf{U}\Sigma_d^a\mathbf{U}^H)^{-1})},\\ \Sigma_D^a &= \frac{1}{\operatorname{diag}((\Sigma_D^{a'} + \mathbf{U}\Sigma_d^a\mathbf{U}^H)^{-1})} - \Sigma_D^{a'}.\end{aligned} \tag{6.20}$$

Note that since $\mathbf{U} = \mathbf{I}_{N_T} \otimes \mathbf{F}_M \otimes \mathbf{I}_{K_{on}}$, (6.20) can be decoupled into $N_T K_{on}$ smaller systems of size $M \times M$ with coefficient matrices $\{\mathbf{X}_{ki_t}\}_{k=0,\ldots,K_{on}-1;i_t=0,\ldots,N_T-1}$ given by

$$\mathbf{X}_{ki_t} = \Sigma_{D,ki_t}^{a'} + \mathbf{F}_M\Sigma_{d,ki_t}^a\mathbf{F}_M^H = \Sigma_{D,ki_t}^{a'} + \operatorname{circ}\left(\tfrac{1}{\sqrt{M}}\mathbf{F}_M\operatorname{diag}(\Sigma_{d,ki_t}^a)\right). \tag{6.21}$$

In (6.21), the index $(\cdot)_{ki_t}$ denotes to select the M elements that correspond to the kth subcarrier from the i_tth transmit antenna. Calculating the numerator in (6.20) requires to solve $\mathbf{X}_{ki_t}^{-1}\vec{b}$ for the right-hand side $\vec{b} = \mathbf{U}\vec{\mu}_d^a - \vec{\mu}_D^{a'}$, whereas the denominator requires knowledge of $\operatorname{diag}(\mathbf{X}_{ki_t}^{-1})$. Even though $\mathbf{X}_{ki_t}$ is a highly structured matrix by being the sum of a positive definite diagonal and circulant matrix $\mathbf{\Gamma} + \mathbf{\Delta}$, no specific solvers for these kinds of systems exist in the literature. Most closely, in [HN05] an algorithm for systems of the form $(\mathbf{\Gamma} + j\mathbf{\Delta})$ is presented, where $\mathbf{\Gamma}$ has eigenvalues with positive real part and $\mathbf{\Delta}$ is real-valued. Hence, in order to not be bound to the $\mathcal{O}(M^3)$ complexity of brute-force matrix inversion, we resort to approximate methods.

Let us first consider $\operatorname{diag}(\mathbf{X}_{ki_t}^{-1})$. As shown in the following, we can approximate $\operatorname{diag}(\mathbf{X}_{ki_t}^{-1})$ by

$$\operatorname{diag}(\mathbf{X}_{ki_t}^{-1}) \approx \operatorname{diag}((\Sigma_{D,ki_t}^{a'} + \tfrac{1}{M}\operatorname{tr}(\Sigma_{d,ki_t}^a)\mathbf{I})^{-1}) \tag{6.22}$$

from the observation that the diagonal of $\mathbf{X}_{ki_t}$ is larger than its off-diagonal elements. Assume the elements $\sigma^2_{d,i}$ of the a-priori covariance Σ^a_{d,ki_t} are i.i.d. random variables that are distributed according to some distribution. Since $\sigma^2_{d,i} \in (0,1]$, they clearly have non-zero mean and we can model

$$\sigma^2_{d,i} = \bar{\sigma}^2_d + r_i \tag{6.23}$$

$$r_i \sim \mathcal{D}(\sigma^2_r), \tag{6.24}$$

where $\bar{\sigma}^2_d$ is the mean of the a-priori variance information of $\vec{d}$ and r_i follows a distribution with zero mean and variance σ^2_r. Note that due to the boundedness of $\sigma^2_{d,i} \in (0,1]$, we have $\sigma^2_r \leq r^2_{\max}$ with $r_{\max} = \min(\bar{\sigma}^2_d, 1-\bar{\sigma}^2_d)$, which corresponds to a degenerate distribution $p(r) = \frac{1}{2}(\delta(r - r_{\max}) + \delta(r + r_{\max}))$ of maximum variance. Now, considering the system matrix $\mathbf{X}_{ki_t}$, the expected value of the first column $\vec{c}_1$ of the circulant part is given by

$$\bar{\vec{c}}_1 = E[\vec{c}_1] = \tfrac{1}{\sqrt{M}}\mathbf{F}_M E[\mathrm{diag}(\Sigma^a_{d,ki_t})] = \bar{\sigma}^2_d \vec{e}_1, \tag{6.25}$$

where $\vec{e}_1$ is the first column of an $M \times M$ identity matrix. Furthermore, the variance on each element of $\vec{c}_1$ is given by

$$E[(\vec{c}_1 - \bar{\vec{c}}_1)(\vec{c}_1 - \bar{\vec{c}}_1)^H] = \frac{\sigma^2_r}{M}\mathbf{I}. \tag{6.26}$$

Hence, on average $\vec{c}_1$ equals $\bar{\sigma}^2_d \vec{e}_1$ and each element varies with standard deviation $\frac{\sigma_r}{\sqrt{M}} < \frac{\bar{\sigma}^2_d}{\sqrt{M}}$, which is smaller than the average power of the first element of $\vec{c}_1$. Eventually, we can conclude that the diagonal of $\mathbf{X}_{ki_t}$ is larger than its off-diagonal elements and the expression in (6.22) approximately holds, where we have estimated the true mean $\bar{\sigma}^2_d$ from the elements of Σ^a_{d,ki_t} by $\bar{\sigma}^2_d \approx \frac{\mathrm{tr}(\Sigma^a_{d,ki_t})}{M}$. This approximation in (6.22) improves with increasing M.

Considering the solution to $\mathbf{X}^{-1}_{ki_t}\vec{b} = (\mathbf{\Gamma} + \mathbf{\Delta})^{-1}\vec{b}$, we note that multiplying with a diagonal matrix is trivial and for a circulant matrix it can be done with quasilinear complexity via the DFT. Accordingly, we can employ the iterative conjugate gradient (CGD) method [GL96], which converges quickly to the exact solution.

Tab. 6.1 outlines the process for solving the system $(\Sigma^{a'}_{D,ki_t} + \mathbf{F}_M \Sigma^a_{d,ki_t}\mathbf{F}^H_M)^{-1}(\mathbf{F}\vec{\mu}^a_{d,ki_t} - \vec{\mu}^{a'}_{D,ki_t})$ of step 1) with the CGD method and summarizes the required number of operations for each step. As the CGD method requires an initial starting point for the iterations, we use the approximate inverse in (6.22) to calculate an initial solution. The same algorithm can also be used for step 3) of the LMMSE estimation process by replacing the corresponding variables. Note that in the last iteration, only the first two steps of the loop are necessary, since the remaining steps yield values for the following iteration. We finally note that all $N_T K_{on}$ small $M \times M$ systems are independent and can be solved in parallel, making it suitable for a parallelized implementation.

Table 6.1: Algorithm description of the Conjugate Gradient Method for LMMSE steps 1) and 3). DFT denotes the operation count for an M-point DFT, i.e. $M \log M$ complex operations, which is quasilinear in M.

Calculation	Add.	Mult.	Div.	DFT	Remarks
$\vec{b} = \mathbf{F}_M \vec{\mu}^a_{d,ki_t} - \vec{\mu}^{a'}_{D,ki_t}$	M			1	Calculating the RHS of the system
$\vec{x}_0 = (\Sigma^{a'}_{D,ki_t} + \frac{\mathrm{tr}(\Sigma^a_{d,ki_t})}{M}\mathbf{I})^{-1}\vec{b}$	$2M-1$	0	$M+1$	0	Initial guess of the solution
$\vec{r}_0 = \vec{b} - (\Sigma^{a'}_{D,ki_t} + \mathbf{F}_M \Sigma^a_{d,ki_t} \mathbf{F}^H_M)\vec{x}_0$	$2M$	$2M$	0	2	
$\vec{p}_0 = \vec{r}_0, k = 0$					
Repeat					
$\alpha_k = \frac{\vec{r}^H_k \vec{r}_k}{\vec{p}^H_k (\Sigma^{a'}_{D,ki_t} + \mathbf{F}_M \Sigma^a_{d,ki_t} \mathbf{F}^H_M)\vec{p}_k}$	$4M-2$	$4M$	1	2	
$\vec{x}_{k+1} = \vec{x}_k + \alpha_k \vec{p}_k$	M	M	0	0	Refined solution, break at $k = K_{Max} - 1$
$\vec{r}_{k+1} = \vec{r}_k - \alpha_k (\Sigma^{a'}_{D,ki_t} + \mathbf{F}_M \Sigma^a_{d,ki_t} \mathbf{F}^H_M)\vec{p}_k$	M	M	0	0	reuse value of α_k calculation
$\beta_k = \frac{\vec{r}^H_{k+1}\vec{r}_{k+1}}{\vec{r}^H_k \vec{r}_k}$	$M-1$	M	1	0	reuse nominator from α_k calculation
$\vec{p}_{k+1} = \vec{r}_{k+1} + \beta_k \vec{p}_k$	M	M	0	0	
$k = k+1$					
Overall count $K_{Max} = 1$	$10M-3$	$7M$	$M+2$	5	
Overall count $K_{Max} = 2$	$18M-6$	$15M$	$M+4$	7	
Overall count $K_{Max} = 5$	$42M-15$	$39M$	$M+10$	13	

Step 2): LMMSE estimation for frequency domain data. According to the results in [MZF16a], the LMMSE estimation process for step 2) can be reformulated to

$$\begin{aligned} \vec{\mu}^p_D &= \vec{\mu}^a_D + \frac{(\bar{\mathbf{H}}^H \bar{\mathbf{H}} \Sigma^a_D + \sigma^2 \mathbf{I})^{-1}(\bar{\mathbf{H}}^H \vec{y} - \bar{\mathbf{H}}^H \bar{\mathbf{H}} \vec{\mu}^a_D)}{\mathrm{diag}((\bar{\mathbf{H}} \bar{\mathbf{H}}^H \Sigma^a_D + \sigma^2 \mathbf{I})^{-1} \bar{\mathbf{H}}^H \bar{\mathbf{H}})} \\ \Sigma^p_D &= \frac{1}{\mathrm{diag}((\bar{\mathbf{H}}^H \bar{\mathbf{H}} \Sigma^a_D + \sigma^2 \mathbf{I})^{-1} \bar{\mathbf{H}}^H \bar{\mathbf{H}})} - \Sigma^a_D. \end{aligned} \tag{6.27}$$

As shown in [ZMMF17], the equation system in (6.27) is equivalent to M systems of size $N_T K_{on}$ each, where each equation system is governed by a band-diagonal matrix with (single-sided) bandwidth $B = N_T$. However, this only exactly holds if Σ^a_D is a diagonal matrix, which is the case when no decoder feedback was incorporated into the demapping operation. In any other case, we can approximate the solution by ignoring the off-diagonal elements of Σ^a_D and still consider the systems separately. Then, following the derivation from Sec. 2.4.3 for a band-diagonal system, we can perform the estimation with complexity $\mathcal{O}(K_{on} N_R N_T^2)$ for each of the M systems. Since the systems are decoupled, all systems can be solved in parallel, creating no extra penalty on the overall latency.

Overall Complexity. Let us denote with $\mathcal{O}(F_N)$ the arithmetic complexity for performing an N-point FFT, which can be approximated by $\mathcal{O}(F_N) \approx \mathcal{O}(N \log N)$. Considering the straight-forward implementation of the SISO MMSE-PIC demapping operation for OFDM with symbol length MK where MK_{on} subcarriers are allocated, the order of

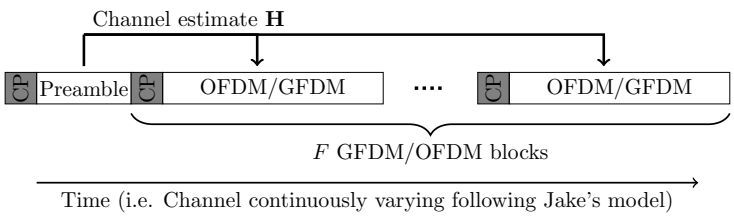

Figure 6.5: Frame structure.

complexity in terms of arithmetic operations can be estimated by

$$C_{\text{OFDM}} = N_R \mathcal{O}(F_{KM}) + IMK_{on}\mathcal{O}(N_R N_T^2), \tag{6.28}$$

where I denotes the number of MMSE-PIC iterations. There, the first term corresponds to the transformation of the received time-domain signal into the frequency domain, and the second term describes the complexity of the MK_{on} LMMSE inversions of the $N_R \times N_T$ channel matrix of each subcarrier for each iteration. Now, considering the arithmetic complexity for GFDM with K_{on} allocated subcarriers, we end up with

$$C_{\text{GFDM}} = N_R \mathcal{O}(F_{KM}) + I(N_T K_{on}\mathcal{O}(F_M) + M\mathcal{O}(K_{on} N_R N_T^2) + N_T K_{on}\mathcal{O}(F_M)). \tag{6.29}$$

Again, the first terms corresponds to the transformation of the received time-domain signal to the frequency domain. The second, third and fourth term correspond to steps 1), 2) and 3) of the MMSE-PIC demapping for each iteration, respectively. In overall, we find

$$C_{\text{OFDM}} = N_R \mathcal{O}(F_{MK}) + IMK_{on}\mathcal{O}(N_R N_T^2) \tag{6.30}$$

$$C_{\text{GFDM}} = N_R \mathcal{O}(F_{MK}) + IM\mathcal{O}(K_{on} N_R N_T^2) + 2IN_T K_{on}\mathcal{O}(F_M), \tag{6.31}$$

showing that the proposed algorithm for GFDM has only a quasilinear overhead in number of symbols and streams compared to OFDM and in total both systems exhibit the similar order of complexity in terms of big-O notation. Compared to the solution provided in [MZF16a], where the complete system using $\mathbf{H}$ was solved at once, the current proposal offers linear complexity in the number of subcarriers K_{on} and quasilinear complexity $O(M \log M)$ in the number of subsymbols M which is a significant gain compared to the cubic complexity in M when directly solving the banded system with the algorithm from Sec. 2.4.3. Furthermore, by splitting the estimation process into 3 sequential steps, with each step consisting of independent equation systems, potential for high-level pipelining and parallelization of a practical implementation is readily available.

6.3 Simulation results

In this section we present performance simulation results of the proposed algorithms using a 4×4 MIMO system under practical LTE EVA and ETU channel models defined by 3GPP (cf. Tab 2.1) exhibiting continuous time-variance according to Jakes model and maximum delay spread of 2.5μs and 5μs, respectively.

Table 6.2: GFDM and OFDM configuration used in the simulation.

Parameter	Symbol	GFDM	OFDM
# Available Subcarriers	K	128	1536
# Allocated Subcarriers	K_{on}	3 or 24	$12 \cdot \{3, 24\}$
# Subsymbols	M	12	1
# Allocated Subsymbols	M_{on}	12	1
# Tx, Rx antennas	T, R	4	4
Prototype filter	$g[n]$	RC	Rect
Filter rolloff	α	0 or 1	-
CP length	-	4.7μs (EVA channel); 16.7μs (ETU channel)	
Time-Window	-	RC window, 16 samples ramp up	
Modulation and coding	-	{(16-QAM, $r = 1/2$),(64-QAM, $r = 3/4$)}	
Channel Model	3GPP EVA, ETU; $f_d = \{0, 30, 100\}$Hz, Jake's Model Fading		
CSI	Perfect CSI or Imperfect CSI: Channel MSE = SNR+3dB		
LDPC Code	WiMax LDPC with SPA log-MAP decoder		
Convolutional Code	$\{1, 133/171\}_8$ RSCC with BCJR log-MAP decoder		
# GFDM/OFDM blocks per frame	F	LDPC: 8; Conv.: 7	
GFDM/OFDM Frame length	T_{Frame}	LDPC: 666μs; Conv: 583μs	

System configuration. Tab. 6.2 shows the simulation parameters that have been adopted in the present simulation. The GFDM parameters are derived from an OFDM LTE system with 15MHz bandwidth with sampling frequency of 23.04MHz, obeying the GFDM Type-II configuration (cf. Sec. 2.4.1). We have made GFDM and OFDM blocks of equal length and 12 subsymbols are contained in one GFDM block. Hence, one GFDM subcarrier has the bandwidth of one LTE physical resource block (PRB). Additionally, to be in line with commonly applied OOB reduction methods, we have added a raised cosine time-window of consisting of 16 ramp-up and ramp-down samples to each OFDM and GFDM block, to emulate a windowed-GFDM [MMGF14] or windowed-OFDM [ZSW+15] scheme. The frame structure of the adopted scheme is shown in Fig. 6.5, where F GFDM or OFDM blocks are preceded by a single preamble, that is used for channel estimation and synchronization. We assume ideal synchronization, i.e. no carrier frequency offset (CFO) and symbol timing offset (STO) are present. The channel was implemented using Jake's model with a given Doppler spread (cf. Sec. 2.2), i.e. the channel was time-variant. However, the CSI for the receiver was obtained only from the preamble and assumed to be constant during the full frame. We have performed simulations with perfect and imperfect CSI where we emulate the channel estimation by supplying erroneous CSI to the demapping unit. Assuming an LMMSE channel estimation unit has knowledge of the PDP, the channel estimate is given by adding random noise of variance depending on the SNR to the correct impulse response, i.e. $\vec{h} = \hat{\vec{h}} + \vec{n}_h$ where $\hat{\vec{h}}$ is the obtained CSI and $\vec{h}$ is the average impulse response during the preamble. Further, $\vec{n}_h \sim \mathcal{CN}(\vec{0}, \sigma_h^2 \mathbf{I})$ is the channel estimation error. The SNR is defined as $\frac{1}{\sigma^2} = \mu r \frac{E_b}{N_0}$ and for imperfect CSI we have $\sigma_h^2 = \sigma^2/2$. For perfect CSI, we set $\sigma_h^2 = 0$.

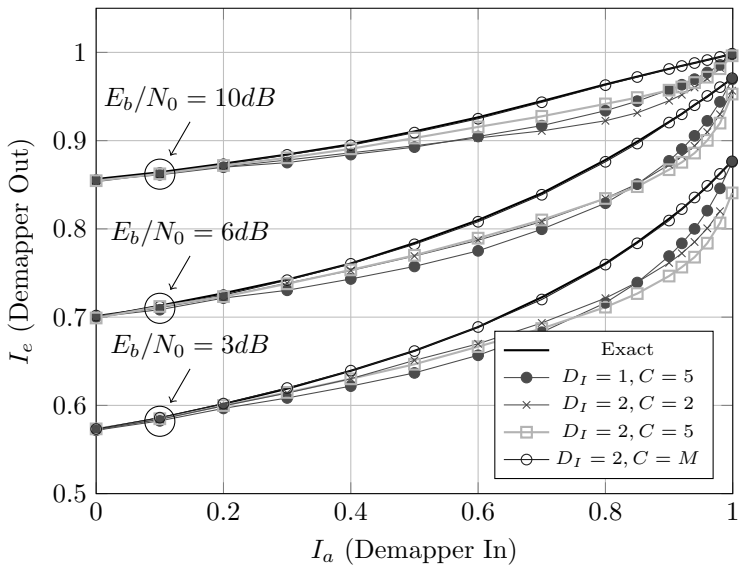

Figure 6.6: Information transfer characteristics for GFDM with the proposed 3-step SISO LMMSE demapping algorithm, compared to the exact solution in (6.14). 16-QAM, $\alpha = 1, K_{on} = 3$.

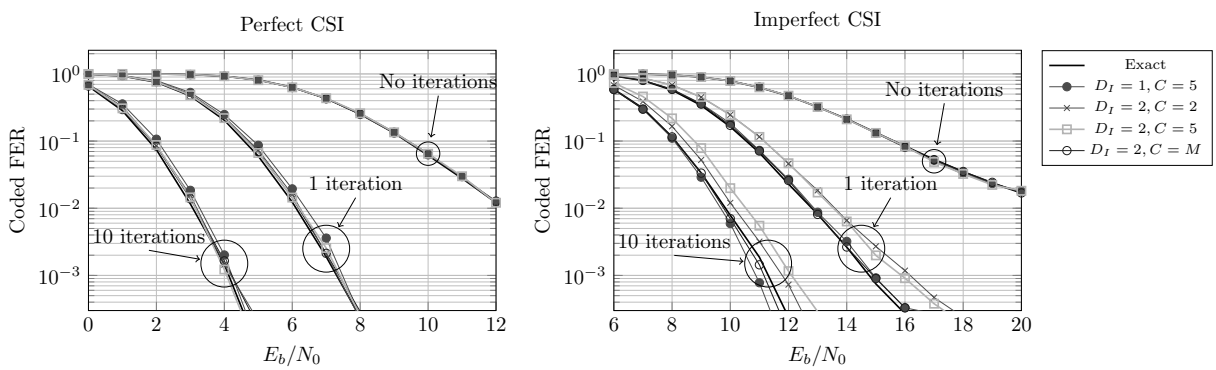

Figure 6.7: Coded FER performance of GFDM with the approximate solution with DFT-spread detection and internal demapper iterations compared to the exact solution in (6.14). ETU power delay profile with $f_D = 30$Hz; 16-QAM $r = 0.5, \alpha = 1, K_{on} = 3$, convolutional code.

6.3.1 Approximation accuracy

Fig. 6.6 and 6.7 compare the performance of the approximate solution of the LMMSE estimation process by doing the estimation in the symbol's frequency domain against the exact detection from (6.14). Fig. 6.6 shows the measured information transfer curves, whereas Fig. 6.7 presents the obtained FER performance with perfect and imperfect CSI. All information transfer curves start in the same point, and the FER performance of all schemes is equal with no iterations, confirming that the 3-step estimation process is exact when no a-priori knowledge is available in the system.

When decoder feedback is available, with perfect CSI the performance of the approximate method is only slightly worse than the exact solution. A very different result occurs for the more realistic case of imperfect CSI as a performance difference of almost 1.5dB at a FER of 10^{-3} can be observed. In particular, performing no extra demapping iterations ($D_I = 1$) and using the approximate CGD method with $C = 5$ CGD iterations

even outperforms the exact MMSE-PIC SISO demapper in terms of FER. We can explain this behaviour by the fact that the exact MMSE-PIC demapper does not consider imperfect CSI, but only considers the noise term in the calculation of a-posteriori LLR. As such, the exact SISO demapper tends to be over-confident with imperfect CSI and the iterative receiver might get stuck in a local minimum and does not necessarily reach the optimum solution. In contrast, the approximate method with $D_I = 1, C = 5$ introduces approximation errors into the system, which occur as extra noise at the demapper. This extra noise can reduce the over-confidence and hence aids in reaching a more optimal solution. The parametrization $D_I = 2, C = M$ yields a performance close to the exact solution, showing that this configuration approximates the exact MMSE-PIC demapping accurately. On the other hand, the parametrizations $D_I = 2, C = \{2 \text{ or } 5\}$ perform $\approx$ 1dB worse than the exact SISO MMSE-PIC demapping. To conclude, we find that performing internal demapping operations ($D_I > 1$) in combination with an exact solution of (6.20) yields a performance that is close to the direct solution of (6.14). In contrast, for imperfect CSI the parametrization $D_I = 1, C = 5$ even outperforms the direct solution of (6.14) in terms of FER at lower complexity. With perfect CSI, there is only a marginal difference between all investigated parametrizations. Hence, in the following evaluations, we employ the parametrization $D_I = 1, C = 5$ for both perfect and imperfect CSI.

6.3.2 MMSE-PIC demapper information transfer

Fig. 6.8 shows the information transfer chart of the SISO MMSE-PIC demapper for GFDM and OFDM in a block-fading ETU channel. The curves of OFDM and GFDM intersect and the intersection moves to the left with increasing SNR, exhibiting potential that iterative GFDM schemes can outperform iterative OFDM schemes. Interestingly, for $E_b/N_0 =$ 15dB, even the starting point of the GFDM curve is above the OFDM curve, indicating that already a non-iterative GFDM LMMSE receiver can outperform OFDM for the present parametrization.

6.3.3 Channel decoder information transfer

Additionally, Fig. 6.8 presents the information transfer chart for the BCJR decoder of the employed $\{1, 133/171\}_8$ recursive systematic CC (RSCC) and the sum product algorithm (SPA) decoder of the WiMax LDPC code that can be used for forward error correction (FEC). For the SPA, the characteristic for different SPA iteration counts are shown. As shown, the SPA performance improves with more iterations, and accordingly we chose to use 100 iterations for the subsequent FER performance measurements. Comparing the shape of channel decoder and demapper curves, it becomes apparent why an LDPC channel code does not perform well with the iterative demapper. Compared to the CC, the curve for the LDPC code exhibits a higher I_a input threshold, before its output I_e gains a significant amount of information. Hence, with little input information, the performance of the LDPC code is worse than the CC. Consequently, when only a small amount of information can be inferred from the received signal, the iterations are more likely to get stuck when using the LDPC code. Additionally, in existing literature it has been

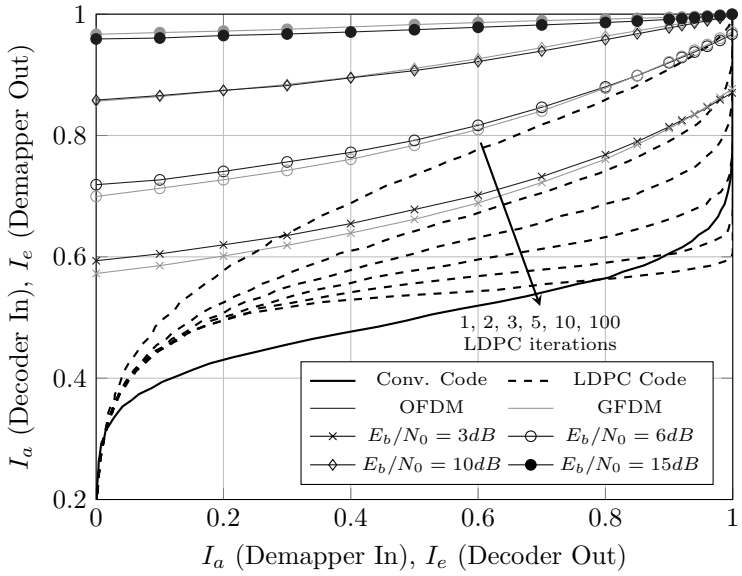

Figure 6.8: Information transfer chart of the SISO demapper and SISO channel decoders in block-fading ETU channel with perfect CSI with code rate $r = \frac{1}{2}$ and $\alpha = 1$, $K_{on} = 3$. GFDM employs the direct solution of (6.14).

shown [SB10] that the CC decoder exhibits a better energy consumption-performance tradeoff compared to more powerful channel codes when employed in iterative receiver structures. In fact, the combination of the MIMO constellation constraint and the CC can be considered as a serially concatenated code [BMDP97], which can, in contrast to a single CC, result in compelling FER performance [BDMP98]. Hence, for the upcoming FER performance simulations, we expect the CC to outperform the LDPC code in an iterative receiver context. On the other hand, with no iterations, the LDPC code is expected to outperform the CC due to its steeper EXIT curve, once the initial input I_a threshold is exceeded.

6.3.4 Decoding performance of different channel codes

Fig. 6.9 shows the performance of the LMMSE and MMSE-PIC receivers with CC and LDPC channel codes for block-fading and time-varying EVA channels with perfect and imperfect CSI. As qualitatively derived from Fig. 6.8, for a non-iterative LMMSE detector, the LDPC code outperforms the CC by approximately 4dB for a FER of 10^{-2} in the block-fading case for perfect CSI. On the contrary, with the MMSE-PIC detector, the CC performs better after convergence, outperforming the LDPC code by 1.5dB for a FER of 10^{-2}. In total, for block-fading channels a gain of 5dB is achieved for MMSE-PIC detection with CCs compared to non-iterative detection employing LDPC codes. The gain increases when the Doppler spread of the channel increases. Similar observations can be done for the case of imperfect CSI, where all curves are shifted approximately 7dB to the right. We have obtained similar relations between LDPC and CCs before and after convergence for different code rates, power delay profiles and doppler spreads and perfect and imperfect CSI (not shown). Accordingly, in the subsequent figures we focus on the LDPC code for

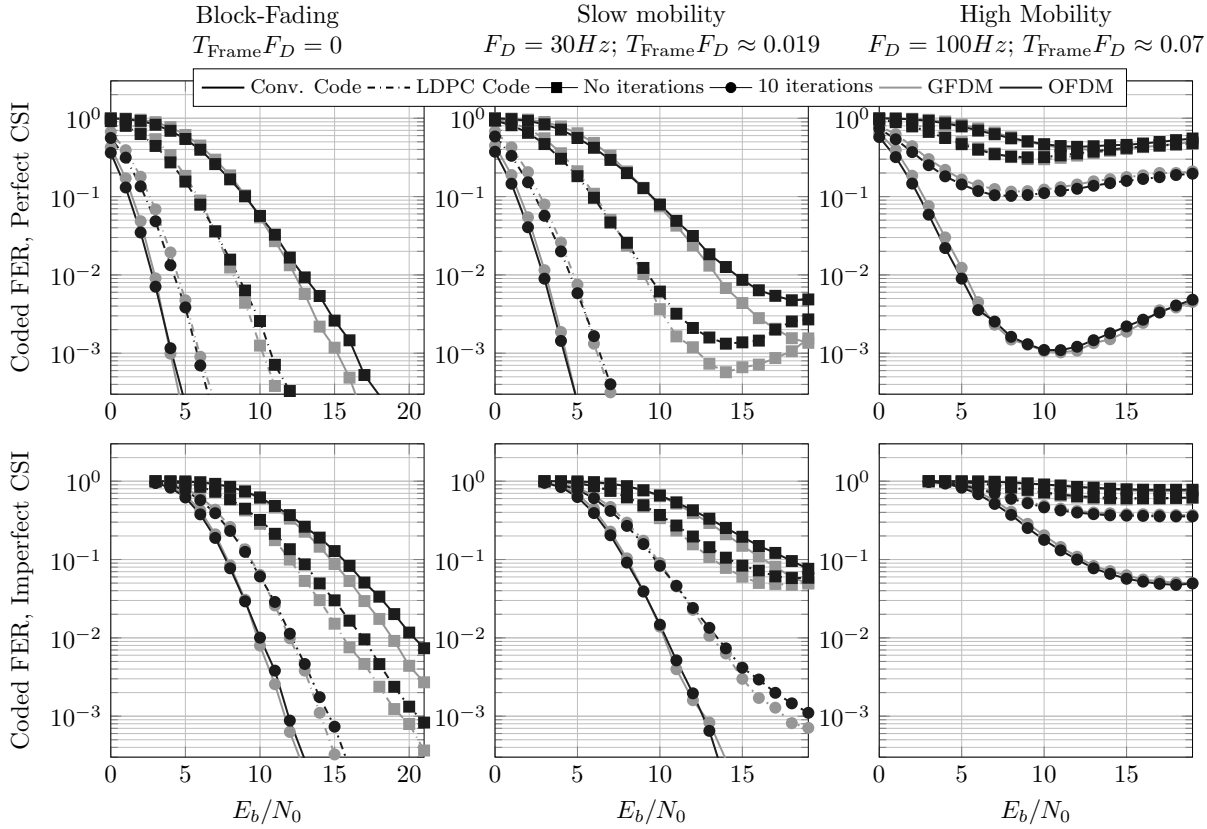

Figure 6.9: Performance of convolutional and LDPC channel codes with and without MMSE-PIC iterations. Here, the channel exhibits an EVA power delay profile, assuming both perfect and imperfect CSI. $r = \frac{1}{2}, \alpha = 1, K_{on} = 3$.

the non-iterative receiver, whereas we employ CCs for the iterative receiver.

When comparing the performance of GFDM and OFDM in Fig. 6.9, we find that for the non-iterative case, GFDM shows a steeper slope in the FER curve, eventually crossing the OFDM curve, which can again be explained with the findings from Fig. 6.8. Accordingly, GFDM outperforms OFDM by roughly 0.8dB at FER=10^{-3} in the block-fading case for perfect CSI. For imperfect CSI we can observe a greater robustness of GFDM against imperfect CSI and GFDM outperforms OFDM by 1dB at FER=10^{-3}. With $f_D = 30$Hz, the effect is emphasized and also the error floor for GFDM due to the time-variant channel is reduced. When $f_D = 100$Hz, the channel varies too quickly and the CSI soon becomes outdated such that reliable detection with the employed frame structure and channel estimation is not feasible. Even, for SNR>10dB, the FER increases with SNR. We can explain this behaviour with the MMSE-PIC demapper being too confident due to the low noise variance since it does not consider the time-variance of the channel. This leads to poor information sent to the channel decoder, which eventually degrades FER performance.

6.3.5 Convergence behaviour

Fig. 6.10 compares the convergence of the iterative receivers for GFDM and OFDM in an

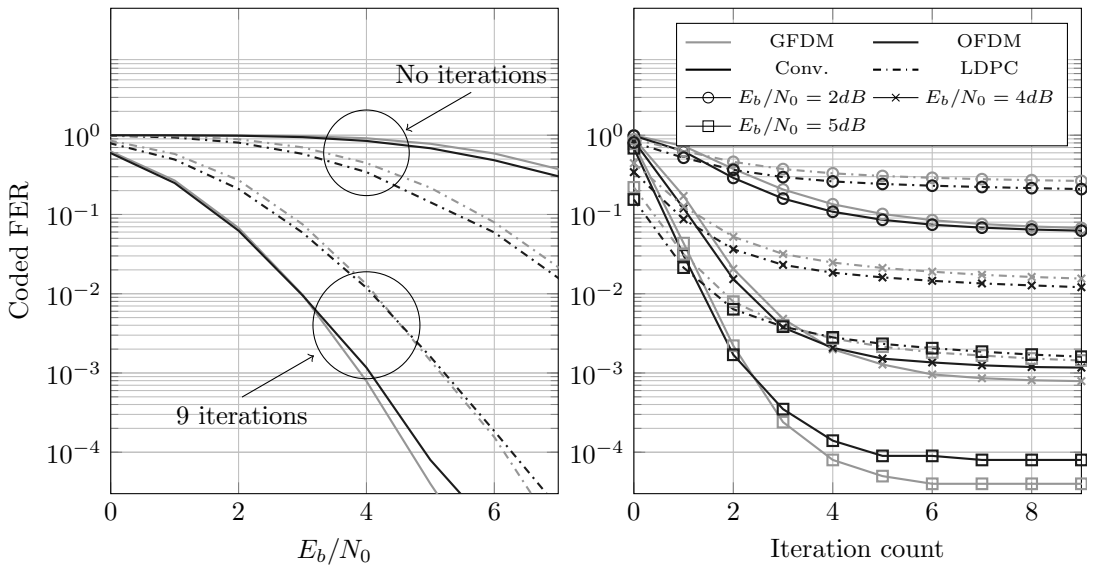

Figure 6.10: Convergence behaviour of GFDM and OFDM. Code rate $r = 0.5, \alpha = 1, K_{on} = 3$, ETU power delay profile, block-fading channel with perfect CSI.

ETU block fading channel, using CC and LDPC codes. With no iterations, the LDPC code outperforms the CC, however its gain during iterations is below that of the CC, eventually performing inferior than a CC. In addition, it is shown that for few iterations (<3), OFDM performs superior than GFDM. Though, for more iterations, GFDM converges to a lower FER, ultimately outperforming OFDM after 4 iterations and converging at 8 iterations. These findings emphasize the necessity of an iterative receiver for GFDM in order to beneficially consider the additional ICI and ISI.

6.3.6 Power delay profile and subcarrier allocation

Fig. 6.11 compares the FER performance for a higher MCS, namely 64-QAM and $r = 3/4$, in block-fading EVA and ETU channels with perfect and imperfect CSI. Additionally, we have simulated a system with more allocated subcarriers, i.e. $K_{on} = 24$. To this end, we have extended the CC codeword to span all available resources. For the LDPC code, due to its limited configuration options, we have concatenated several LDPC code words of length 2016 bits and interleaved them over all subcarriers and subsymbols such that each codeword experiences the same frequency diversity.

First, comparing the ETU and EVA channels, we observe a steeper slope in the FER curves for the ETU channel. This can be straight-forwardly explained by the larger frequency diversity of the ETU channel. Additionally, comparing the curves for $K_{on} = 3$ with $K_{on} = 24$ we observe a steeper slope for the $K_{on} = 24$ curve. Again, this is explained by a bigger frequency diversity when a codeword can span more subcarriers. A fundamental difference between GFDM and OFDM can be observed when considering the non-iterative LMMSE receiver for $K_{on} = 24$: Despite GFDM was outperforming OFDM for $K_{on} = 3$, for $K_{on} = 24$ GFDM performs more than 2dB worse than OFDM and the slope of both curves is equal. We can explain this by the increased amount of self-interference in GFDM

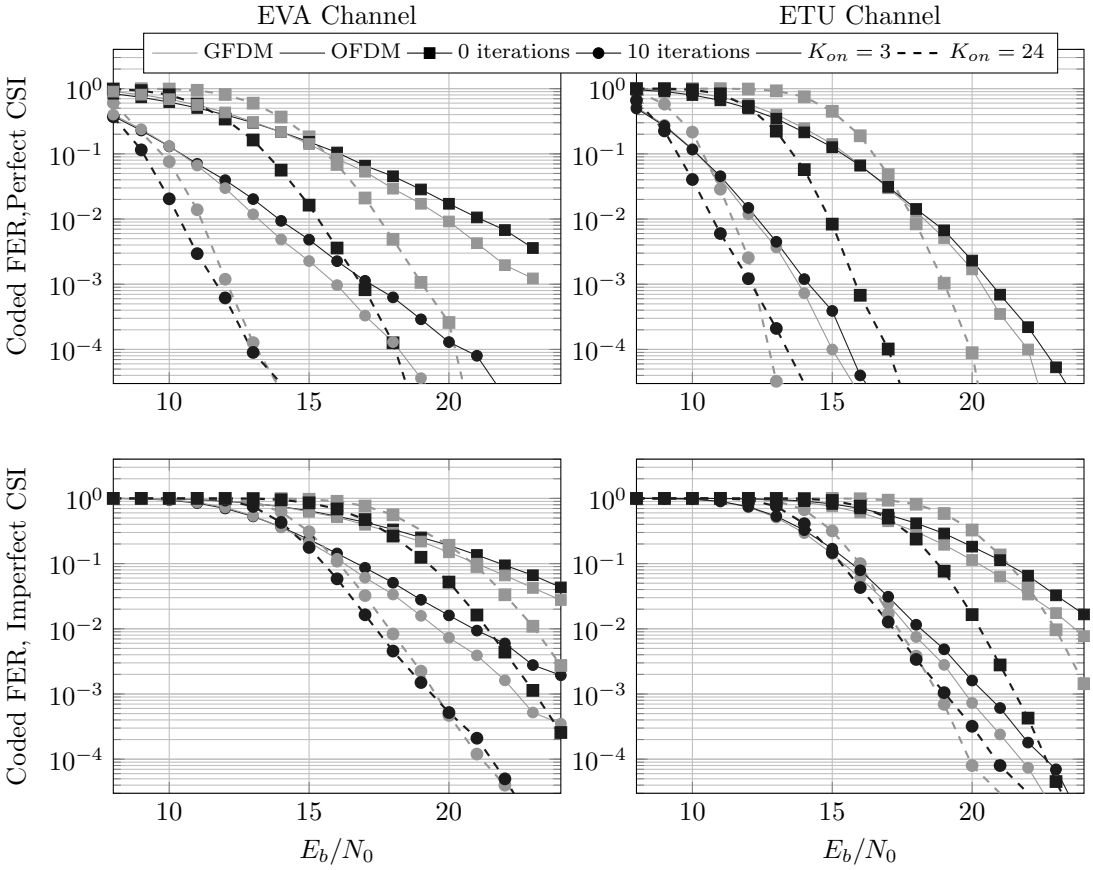

Figure 6.11: FER performance for 64QAM modulation, code rate $r = 3/4$ and $\alpha = 1$ for EVA and ETU block fading channels. The rate $3/4$ CC was obtained by puncturing the original half-rate code with the puncturing pattern $[1, 1, 0, 1, 1, 0]$.

when $K_{on} = 24$. In this case, the LMMSE equalizer cannot reliably resolve the interference and the performance degrades. In contrast, comparing the performance of the iterative schemes, we observe that for $K_{on} = 24$ GFDM shows a steeper slope in the FER curve compared to OFDM. This indicates that the iterative GFDM receiver can harvest more frequency diversity from the multipath channel due to the wider subcarriers. Eventually, in the ETU channel GFDM outperforms OFDM for FER=10^{-4} by 1dB for both perfect and imperfect CSI. In the EVA channel, OFDM performs superior than GFDM until FER=10^{-4}. Again, these findings are in line with our previous assumption that a non-iterative demapper that relies solely on the constellation constraint cannot exploit the full potential of non-orthogonal waveforms in frequency-selective channels.

6.3.7 Performance with different MCS

Fig. 6.12 presents a more detailed analysis of the coded FER performance of the iterative receiver under ETU channels with imperfect CSI, using a CC for FEC. From the figure, we can make several observations: First, in general we see that the curves for higher allocations are shifted to the left, compared to $K_{on} = 3$. We can readily explain this by both the increased code word length and the larger frequency diversity by the wider

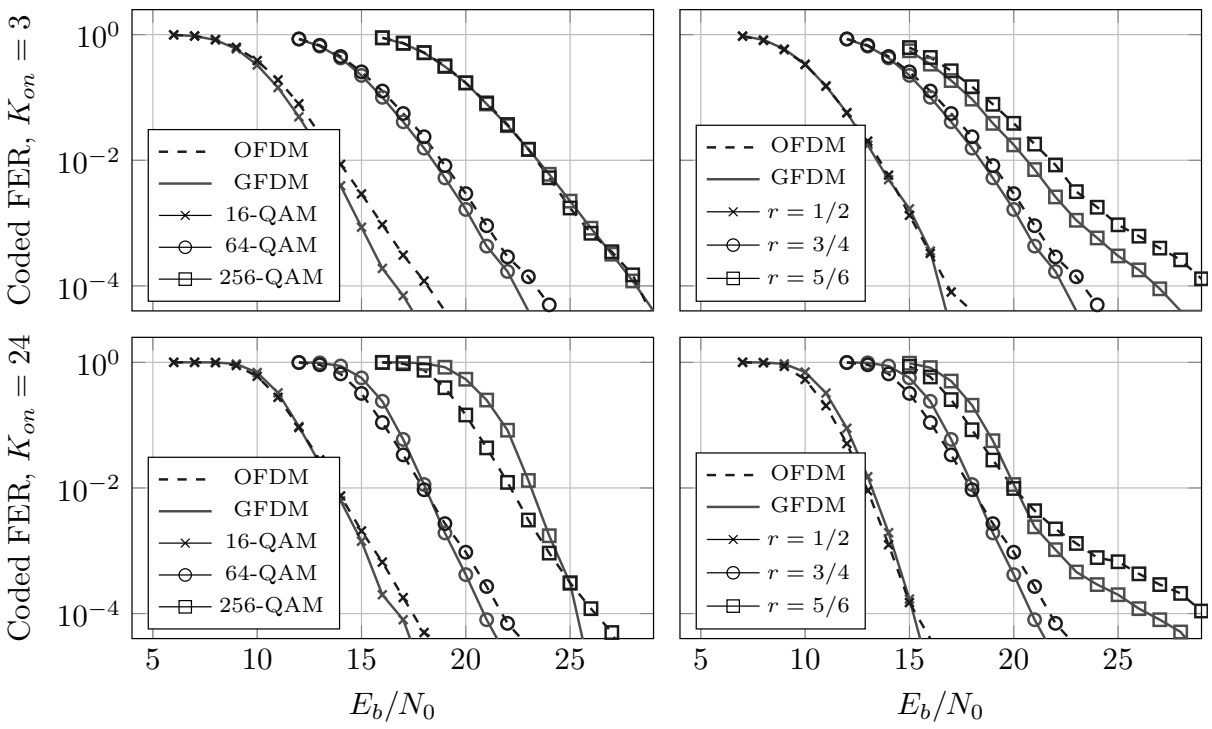

Figure 6.12: Performance of MMSE-PIC iterative receiver with different MCS. Results were simulated with block-fading ETU channels with imperfect CSI using a CC. The curves show the achieved FER after 10 iterations. The code rate for the left column was $r = 3/4$, the modulation for the right column was 64-QAM. The rate 5/6 CC was derived from the standard rate 1/2 CC by applying the puncturing pattern $[1, 1, 0, 1, 1, 0, 0, 1, 1, 0]$.

allocation. Moreover, the curves obtained with GFDM are steeper than the corresponding OFDM curves. We can explain this by both the increased frequency diversity of the GFDM waveform as well as the stronger constellation constraint of GFDM due to the self-interference, making the inner code more powerful. Second, comparing the result for different constellation sizes, we observe that GFDM suffers more from higher modulations, as the curves shift more to the right compared to the corresponding OFDM curves. We might explain this behaviour with the fact that with higher modulation orders, the constellation constraint when using Gray-mapping loses its strength. Hence, the negative aspect of self-interference (i.e. additional "noise") increases and the performance degrades. It needs to be investigated, whether this behaviour changes with a different QAM mapping strategy in future works[3]. Eventually, we can see that increasing the code rate yields favorable results for GFDM, as the gap between OFDM and GFDM increases. When the code rate increases, the outer CC becomes less powerful, making the inner code, i.e. the constellation constraint more important for the overall detection. Hence, we can observe the performance gains for GFDM. Note also, that an error floor might pop up for the rate 5/6 code, which can be due to the fact of imperfect CSI, and hence the equalizer does not yield perfect constellation symbols even for higher SNRs.

[3] As a sidenote, a different QAM mapping can also degrade GFDM performance, as the initial LMMSE estimate of the transmitted symbol will likely be worse, yielding a worse starting point for the iterative detection.

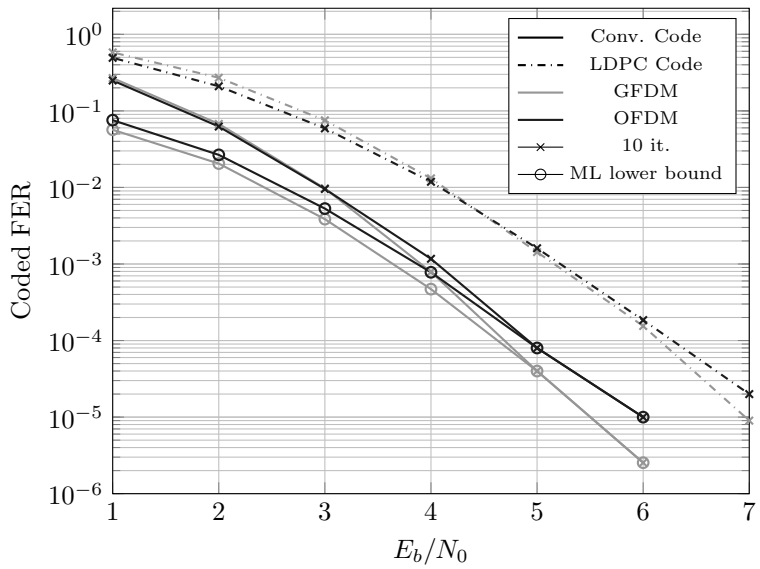

Figure 6.13: ML lower bound for the GFDM and OFDM. ETU power delay profile with static block-fading, $r = 0.5, \alpha = 1, K_{on} = 3$.

6.3.8 Achieving the ML detection performance

Considering the optimally achievable ML performance, Fig. 6.13 presents the obtained FER performance of the converged OFDM and GFDM demodulators along with an ML performance lower bound that was obtained with a genie-aided technique as in [ZMMF16]: Upon convergence of the detection, the distance d_R of the detected codeword to the received signal is compared to the distance d_T of the transmitted codeword to the received signal. If $d_R < d_T$, an optimal ML detector would also yield an error. If $d_R > d_T$, it is assumed that an optimal ML detector would have found the correct solution. This process overestimates the performance of the ML detector and hence yields a lower bound on ML decoding performance. The tightness of the bound becomes better, when the detection algorithm approaches the ML decoding performance [ZMM+16]. As is shown in Fig. 6.13, the MMSE-PIC detector approaches the ML bound for higher SNR when using the CC. The obtained results show that the proposed iterative detection algorithms achieve the optimal performance for the given signal structure when using a CC. Further, the ML bound for the GFDM system is roughly 0.5dB left to the OFDM ML bound, showing the benefits of frequency diversity and ICI for higher SNR. With an LDPC code, the ML bound could not be calculated with the proposed technique, since the obtained FER performance was still far away from the optimal ML performance. In particular, the lower bound estimate was FER>0, since for each erroneously detected frame we experienced $d_R > d_T$ in the LDPC coded case. Here, we again see the superiority of the CC compared to the LDPC code, as the CC reaches the optimally achievable performance in the considered iterative receiver due to its interaction with the SISO MMSE-PIC demapper. However, we expect the actual ML performance of the LDPC code to be better than that of the CC due to larger minimum distance of LDPC code in general [RL09].

6.4 Summary

In this chapter, we identified the combination of a channel code with subsequent MIMO-GFDM modulation as a serially concatenated code, which can be decoded in an iterative fashion. We showed that the technique of MMSE-PIC demapping can be formulated as a CWCU LMMSE estimation and proposed a receiver which is based on a LMMSE SISO demapper and SISO channel decoder. The proposal could harvest the foreseen frequency diversity and hence outperformed OFDM in realistic channel conditions. We analyzed the computational complexity of the proposed algorithm and researched means for a low-complexity implementation based on a sparse factorization of the system matrix. The proposal achieves a computational complexity similar to OFDM. Further, the factorization allows for high-level parallelism by decoupling the equation systems. We analyzed the detection performance with two different channel codes, namely CCs and LDPCs, and showed that the use of actually weaker CC is beneficial for iterative processing. With the analysis of the respective EXIT chart of the demapper and decoder and could eventually explain this observation.

When comparing the obtained performance of GFDM and OFDM, we observe that GFDM is especially beneficial in the high SNR region, which corresponds to very small FER in the range below $\approx 10^{-4}$. In this area, GFDM outperforms OFDM and hence yields a more reliable communication. Accordingly, we can suggest to use GFDM with the provided configuration in the scenario of URLLC, where the low-latency constraint does not allow retransmissions, but still high reliability is required.

Chapter 7

GFDM - A promising waveform?

Since the technique of GFDM was proposed in 2009 [FKB09], it has been pushed as a strong alternative for OFDM waveforms. Numerous research groups joined the GFDM research community, showing different results starting from theoretical results [LW16, BDM15, CSH17], to spectral characterization [GKCD16, HSL17], near-optimal MIMO detection [TWD+15], synchronization [LW16] and complexity reduction of transmitter and receiver [FMD15a, DT15]. However, in recent standardization works on 5G new radio (NR) [Nag17], filtered or windowed OFDM variants were chosen as the waveform for 5G. Hence, it remains the question how useful GFDM actually is, given the recent decisions from 3GPP.

In literature, evaluations on GFDM showed both superior [HSL17, GKCD16, DT15, ZMMF17, NZMF17, GBB+17, VBDH17] and inferior [AFRFB15, TWD+15, LQ15, LK17, GMP17, MZF16b] performance compared to OFDM. In early works [MLRF11] it was shown that GFDM can achieve a very narrow and well-confined spectrum compared to OFDM. Recently, also reliable results regarding coded performance in realistic channels became available. There, depending on the employed detection algorithm, GFDM waveforms sometimes outperformed OFDM. In total, the research community is not united, if and in which cases GFDM is a promising waveform. In this regard, the viability of GFDM and consequently is applicability to real-world problems is discussed below.

The selection of OFDM-variants for 5G is understandable. The main focus lied in the reduction of OOB emissions, where subband-filtering and windowing fulfill the envisioned spectrum masks for 5G to support asynchronous operation per subband. Other than that, the proven frame structure of 4G could be kept, with options to shorten the transmission time interval (TTI) length to fewer OFDM symbols for tackling low-latency applications. Moreover, 3GPP proposed to scale the numerology to shorter symbols and wider carriers to further support low-latency communication. To keep spectral efficiency, the CP would also be scaled. In total, filtered OFDM variants are envisioned to support foreseen 5G use cases reasonably well. However, the selected waveforms for NR are not without drawbacks, and GFDM can overcome some of these.

- Considering the spectrum mask and OOB emission, GFDM is fully able to compete or even outperform the NR proposal, see e.g. [ZMMF17] and Fig. 1.1. Moreover, subcarrier-wise filtering compared to subband filtering allows in principle a

greater flexibility regarding spectral allocations[1]. Subband-filtering of NR either introduces IBI in case of F-OFDM [AJM15] or noise-correlation in case of UF-OFDM [MDD+02], marginally reducing the capacity for high MCS. The proposed weighted overlap-and-add (WOLA) [ZMSR16, MZSR17] for OFDM overcomes this, however at the cost of slightly reduced spectral efficiency compared to CP-OFDM. In this regard, GFDM can be configured to use WOLA in combination with constant pilot symbols at the block boundary to further reduce OOB emission or reduce the necessary overhead of WOLA. This idea has been demonstrated in [NZMF17] to yield higher throughput compared to CP-OFDM in a WiFi setting.

- Scaling of the entire numerology for low-latency applications has two main consequences: First, by similarly scaling the CP to keep spectral efficiency, the maximum channel length is reduced. Hence, the scaling can only be done for smaller cells. Also, GFDM cannot overcome this problem, when considering a TTI length of one OFDM symbol. However, an additional effect of shorter symbols is an increased robustness to both CFO and Doppler spread, i.e. time-varying channels. A time-varying channel induces ICI into the OFDM-system, and the interference increases with the length of the OFDM symbol. Hence, in high-mobility scenarios short symbols are preferred. But, as mentioned before, short OFDM symbols limit spectral efficiency due to the required CP length. In contrast, GFDM being configured as Type I, can pack multiple short subsymbols into one GFDM symbol which is protected by a single CP, and can at the same time achieve both robustness against Doppler and less CP overhead.

- Eventually, a fundamental limitation of OFDM-variants is the transmission of QAM symbols over a single frequency bin. As was shown before, this limits the effective channel's minimum distance and hence can reduce capacity. In contrast, GFDM allows some frequency diversity at the symbol level with an additional rate-1 code due to ISI and ICI, enforced by the constellation constraint. Even though a decent channel code would overcome the minimum distance problem for OFDM, the constellation constraint can aid in the search for an optimal decision, eventually leading to larger capacities of the GFDM system.

These three discussed advantages can be directly mapped to use cases where GFDM can be considered a practical waveform candidate.

Specialized Mobile Radio (SMR) and Cognitive Radio (CR) Applications. SMR is a service operating in the VHF frequency band which takes fees for supporting private mobile communications, such as for communication among Taxi drivers or workers at a construction site [FCC17]. Technically, the service divides the available bandwidth into numerous very narrow channels with $10 - 20$kHz spectral distance. As each channel operates independent and asynchronous from neighboring channels, the Federal Communications Commission (FCC) enforces tight spectral masks on each channel. These masks

[1] However, more flexible allocations requires a larger control overhead to communicate the allocation to the receiver

ensure that one channel does not interfer with adjacent ones. As an example, emission Mask D [FCC13, Rule 90.210] enforces an OOB attenuation of 70dB at a distance of one channel bandwidth away from the channel's center frequency. Traditionally, ensuring these emission masks requires bulky and costly analog filters for either each used channel or a combination of one analog filter with a tunable oscillator.

In the scenario of a CR system, a primary, licensed user freely operates in a given frequency band. However, since the primary user might not always use all of its spectrum, there can be temporarily unused resources within the band, hence wasting capacity. The idea of CR is that a secondary, probably unlicensed, user exploits these vacant resources for communication. In this setting the secondary user should be transparent to the primary user and keep disturbances on the primary user to a minimum. The secondary user can achieve this by constantly scanning the licensed band for free spots and then allocating the according frequencies for its own transmission. Naturally, as the primary user can start reusing these frequencies at any time, the CR device needs to be able to quickly switch between allocated frequencies. Moreover, as the spectral holes can be very narrow, wide guard bands on the secondary user side would significantly reduce capacity. Hence, the CR device is required to tightly limit its OOB emission.

Obviously, both applications above require the signal to obey tight spectral masks per carrier. Moreover, the more flexibly frequencies can be allocated by a system, the more efficient is the CR system. Having a digital wideband modulation with narrow channel with tight digital masks would allow an SMR device to use less bulky RF equipment like analog filters and tunable mixers. As high-quality analog parts are more cost-intensive than silicon, a digital modulation can at the same time reduce costs and add flexibilty for SMR devices. Configuring GFDM for low OOB emission by using windowing and pilot guard symbols [MF16] in combination with narrow carriers directly fulfills these requirements, hence making it a suitable waveform for the described use cases.

Ultra-reliable low-latency communication (URLLC) . URLLC is, among eMBB and machine to machine (M2M) communication, an important aspect that 5G system and beyond have to fulfill. URLLC enables applications like tactile internet or real-time control over cellular links. Generally, high reliability can either be obtained by requesting retransmissions of lost packages or by reducing the probability of lost package in the first place. Obviously, relying on retransmission schemes is impossible for low-latency communications, as retransmissions require additional protocol overhead and multiple subsequent transmissions of the frame. Hence, URLLC needs to diminish frame loss probability in the first place.

To reduce frame loss probability, diversity schemes are applied. In particular, multi-connectivity is employed, where the same data is transmitted over several independent links from probably distant base stations to exploit large-scale spatial diversity. Assuming the links are independent, each new link reduces overall FER by the FER on the new link. Hence, a better FER on the point-to-point link reduces the number of required links, which in turn reduces cost and energy consumption of the radio, decreases protocol overhead of maintaining multiple links and increases overall cell capacity as packet redundancy is

reduced.

As was shown in this work, as well as in e.g. [ZMMF15, ZMMF17], near-optimal GFDM receivers outperform optimal OFDM receivers in high SNR regions, i.e. in the region that is suitable for ultra-reliable communication. Hence, employing iterative GFDM receivers leads to increased coverage, less power consumption or less required links for URLLC communications. Therefore, GFDM can be considered as a viable waveform for URLLC communications. However, it needs to be ensured that the increased complexity and processing latency of GFDM does not outweigh the advantage in the improved FER.

Vehicular Communication. Vehicular communication (V2X) is a challenging field for wireless communications. In this scenario, vehicles such as cars, trains or motorcycles communicate with each other or with fixed radios mounted at infrastructure, such as traffic lights, bridges or street lamps. Vehicles and infrastructure exchange both mission-critical and non-critical messages. For example, mission-critical security messages such as emergency brake information need to be reliably transmitted with lowest latency, drawing a link to URLLC in 5G. On the other hand, non-critical messages such as periodic location information or even entertainment data can afford packet loss or retransmissions, but require larger bandwidth, being more similar to the eMBB application in 5G.

Naturally, as vehicles move rapidly, the wireless channel between radios is highly time-variant including Doppler spread or even different Doppler shifts over different paths. Moreover, a rich-scattering urban environment can create highly frequency-selective channels [VBTV15]. In overall, these conditions render the wireless channel very challenging for reliable wireless transmission. In particular, the strong time-variance requires short symbols to combat Doppler-induced ICI, however at the same time the CP length is constrained by the channel length. In consequence, using an OFDM-based waveform strongly limits spectral efficiency. Moreover, strongly frequency-selective channels can incur deep fading of some OFDM carriers, which requires to rely on powerful channel codes to combat the fading. To this end, GFDM can be a viable alternative to OFDM, as it does not suffer from the (sub)symbol-length vs. CP-length tradeoff. Moreover, as mentioned before, GFDM offers a better FER in high SNR regions, making it more suitable for the URLLC aspect in V2X. As an example for the application of GFDM in V2X, the authors in [ZFF17] designed a GFDM system that outperformed CP-OFDM in challenging vehicular channel conditions in terms of throughput, FER and spectrum mask.

Summary. Given the observations in this work and related literature, GFDM cannot be considered as a general replacement for the simple and beautiful CP-OFDM waveform and its descendants. Rather, particularly where OFDM suffers from either spectral masks or challenging channel conditions, GFDM can indeed be a suitable replacement. To verify this assumption, real-world experiments with real-time implementation of the proposed algorithms are the consequent next steps.

Chapter 8

Conclusions and Future works

The main goal of this thesis was to analyze the applicability of generalized frequency division multiplexing (GFDM) within MIMO wireless communication systems in the context of waveform alternatives for the 5th generation of cellular networks. After having analyzed the GFDM system with methods from time-frequency analysis (TFA), we proposed two methods for achieving transmit diversity and spatial multiplexing gains for MIMO-GFDM systems and evaluated the receivers in multipath fading channels.

8.1 Summary of the results

In particular, the following results were obtained:

- ▷ We introduced the basic GFDM signal structure and linear receiver types. We described the configuration parameters for GFDM in relation to OFDM and defined two general GFDM configuration types: GFDM Type-I uses subsymbols that have equal length to one reference OFDM symbol. Hence, the block length of one GFDM symbol is longer than that of a reference OFDM system, yielding larger system latency on the one hand, but smaller CP overhead on the other hand. In GFDM Type-II, a GFDM block has equal length as a reference OFDM symbol, making the subsymbols shorter and subcarriers wider, which reduces the number of subcarriers and increases robustness against Doppler spreads.

- ▷ We compared the performance of linear GFDM receivers in the coded and uncoded case against a CP-OFDM system. We concluded that increased self-interference by means of higher rolloff reduces performance of these receivers. In addition, we concluded that linear GFDM receivers introduce post-equalization noise correlation, which reduces performance compared to the orthogonal OFDM system, when considering soft QAM demapping and channel coding.

- ▷ We introduced the linear system model of the equivalent MIMO-GFDM system. We showed that the system model is equivalent to a large-scale linear system with localized interference. Hence, the results from this thesis on MIMO detection for

GFDM can have impact on detection for massive MIMO under flat fading, single-carrier systems with intersymbol interference.

- ▷ We introduced the basics of the mathematical theory of time-frequency analysis (TFA) and Gabor analysis and identified the GFDM transmit signal as a critically sampled discrete Gabor expansion. This connection makes results from TFA directly applicable to the present investigations, yielding theoretical and practical insights into the design of GFDM. Moreover, we showed how multicarrier waveforms in general fit into the framework of TFA and explained their design in terms of results from TFA.

- ▷ Using methods of TFA and in particular the BLT, we showed under which circumstances the GFDM modulation matrix becomes singular. We concluded that an odd number of subcarriers or subsymbols is required when using standard pulse shaping filters. Based on Gabor analysis, this constraint was recently circumvented with more specific filter designs [NMZF17]. Moreover, we showed that the linear filter matrices for GFDM follow the structure of a Gabor transform matrix, allowing the filtering operation to be performed with low arithmetic complexity.

- ▷ By using the Zak-Transform methods we found closed-form solutions for the ZF and LMMSE filters in AWGN channels for GFDM and hence could give closed form expressions for the inverse of the GFDM modulation matrix.

- ▷ We designed and evaluated two detection algorithms for achieving transmit diversity with GFDM signals. We proposed TR-STC, which achieves full diversity gain with low-complexity STC combining. However, since TR-STC encodes two subsequent GFDM blocks, it requires that the wireless channel remains static for two blocks and increases the decoding latency. These drawbacks were mitigated by the proposal of encoding the GFDM data subsymbols with in one block and using a widely linear equalizer to jointly perform STC combining and GFDM demodulation.

- ▷ We benchmarked the proposed STC algorithms against the conventional OFDM STC and found GFDM to have a comparable performance to OFDM when using small rolloff factors. For stronger self-interference, the linear receivers performed poorly against OFDM. Again, the problem of information loss due to post-equalization noise correlation for the non-orthogonal systems became apparent, leading to the conclusion that linear receivers for non-orthogonal systems cannot compete with the OFDM system.

- ▷ We analyzed the minimum euclidean distance between the points in the lattice which is spanned by the modulated signals of OFDM and GFDM. We have found that the distribution of $d_{\min}$ over different fading realizations is favorable for systems with ICI, since they achieve frequency-diversity on the constellation constraint level.

- ▷ Accordingly, we proposed two non-linear receiver structures for spatially multiplexed GFDM streams that aim at reaching the optimal ML performance, which is dictated

by the minimum distance between codewords. The first proposal was based on a combination of sphere-decoding with successive interference cancellation (SIC) and achieved tremendous performance gains over OFDM in the uncoded case. Despite, in the more practical coded case the proposal proved itself to perform poorly due to the unavoidable error propagation of the SIC technique. On the other hand, requiring a joint non-linear detection in the ML sense was infeasible from a complexity point of view.

- ▷ We investigated the usage of both LDPC codes and CC as the channel code for the iterative receiver schemes and have found, that the less powerful CC performs superior to the powerful LDPC code in the context of iterative receivers. We could explain this observation by analyzing the respective information transfer curves of the channel decoders.

- ▷ We designed an iterative receiver algorithm to resolve the self-interference with the aid of the information gained from the channel decoding. We proposed an implementation that achieves complexity in the same order as an equivalent OFDM system and analyzed its performance under realistic channel conditions. We found that the proposal could outperform an equivalent OFDM receiver under certain system configurations. Moreover, we showed that the iterative scheme reaches the optimal ML performance for certain configurations.

In conclusion, this work presented a thorough analysis of diverse MIMO detection algorithms for GFDM and benchmarked its performance against the popular OFDM system. We saw that OFDM is a technology that is challenging to compete with. Its orthogonality easily allows optimal ML decoding which is not straightforward to obtain when self-interference is present due to the inherent explosion of complexity. On the other hand, we saw that the existence of self-interference increases the minimum distance of the received symbols, opening up the potential to outperform an optimal OFDM system, when ML decoding performance is achieved. However, we showed that ML decoding for non-orthogonal systems requires significantly more elaborate algorithms compared to the elegant and straight-forward solution for OFDM. Moreover, we showed that the commonly suspected increase in complexity for optimal detection algorithms for non-orthogonal waveforms can be overcome by exploiting the locality of the self-interference. As such, we could design near-optimal algorithms for GFDM with equal complexity compared to CP-OFDM that outperformed CP-OFDM in high SNR regions. At the same time, we preserved the flexibility of GFDM as the general model of multicarrier waveforms in terms of time-frequency analysis. Eventually, based on the present results and related literature, we proposed practical use cases for applying GFDM.

8.2 Open Research Topics

In addition to the aspects covered in this work, many topics that relate to MIMO detection for non-orthogonal waveforms remain open and can be addressed in future works.

- ▷ In this thesis we showed that the minimum distance of non-OFDM waveforms has an advantageous probability distribution compared to OFDM. However, these results only hold for the uncoded case. An analysis of the minimum distance concerning the coded case or information-theoretic treatment of the capacity of large-scale linear systems would be a consequent next step. In [ZMMF16] bounds for the capacity were obtained, but the calculation requires a significant amount of work and more elegant solutions could be available.

- ▷ In chapter 5, we proposed a combination of SIC and sphere-decoding to yield an algorithm that essentially performs the K-best sphere-decoding algorithm while only keeping the best path, which yielded poor performance. However, considering the structure of $\mathbf{R}$ in (5.9) and Fig. 5.4 it becomes apparent that the interference is highly structured and deterministic. Future works can design a dedicated sphere-decoding algorithm that exploits the structure of $\mathbf{R}$ to reduce complexity and make running a sphere-decoder on the full $\mathbf{R}$ matrix feasible. Moreover, the deterministic structure of $\mathbf{H}$ can be used to design dedicated QR decomposition algorithms to reduce complexity.

- ▷ Using lattice reduction (LR) algorithms [WSJM11] as a preprocessing step for MIMO detection was shown to significantly improve the performance of linear detection schemes. Considering that the receiver lattice of non-orthogonal waveforms is of very high dimension the performance of according LR-aided detection can become very different from the low-dimensional MIMO-OFDM or flat-fading systems and can open up another direction of research.

- ▷ In this work, we exclusively used Gray-mapping for bit-to-constellation mapping. Gray-mapping is optimal for non-iterative receiver schemes [CTB98], however with iterative receivers, gains for a non-Gray-mapping were obtained [CR01, LR98]. The mapping essentially influences the strength of the constellation constraint and research on the effect of the performance of iterative receivers for non-orthogonal waveforms could potentially show further gains.

- ▷ In [PSM06] it was shown that the inclusion of an additional rate-1 CC (an *accumulator*) can remove error floors and bend information transfer curves to a more favorable shape. Wether this technique also works within the framework of the proposed MMSE-PIC detection can be an interesting research direction.

- ▷ The present analysis was carried out under the assumption of ideal RF hardware. Especially with multicarrier waveforms that exhibit a high PAPR, it is mandatory to analyze performance under non-linear distortions of the power amplifiers or IQ impairments of non-ideal mixers and other analog pieces. In [SM15, SMMF14] research was initiated to find iterative algorithms to cancel the interference induced by non-linear distortions. However, theoretical and more deep insights are necessary.

- ▷ The proposed SISO demapper for the MMSE-PIC detector assumed a continuous Gaussian distribution of the constellation symbols due to complexity reasons. How-

ever, splitting the linear model $\vec{y} = \mathbf{H}\vec{d} + \vec{w}$ into $\vec{y} = \vec{h}_i d_i + \mathbf{H}_i \vec{d}_i + \vec{w}$ where $\vec{h}_i$ is the ith column of $\mathbf{H}$ and $\mathbf{H}_i, d_i, \vec{d}_i$ are $\mathbf{H}$ without the ith column, the ith element of $\vec{d}$ and $\vec{d}$ without the ith element, respectively, one can create a more accurate, non-linear, MMSE demapper by assuming the distribution of d_i as discrete but $\vec{d}_i$ to be Gaussian. This demapper can generate more accurate results for the LLRs and hence improve the detection performance. It can be promising to research the trade-off between the increased complexity and the obtained performance.

- ▷ With the advent or reinvention of machine-learning methods it becomes obvious to use artificial intelligence or machine learning to perform MIMO detection or channel decoding. Useful techniques can be e.g. neural networks or genetic algorithms to perform either demapping or channel decoding. These algorithms can be easily parallelized and hence can yield very low decoding latency with at the same time very promising performance.

- ▷ A crucial step in evaluating a new system is its implementation for real-time applications. Though already some steps for implementing GFDM were accomplished [DMG+15, DMG+16, DBD17] still a real-time spatial multiplexing implementation is not yet available. Also, thorough evaluations of implementations regarding latency and throughput is not available.

Appendix A

Proofs

A.1 Derivation of Widely Linear Estimator for STC-GFDM

Starting from (4.26), we calculate the autocorrelation matrix Γ of $\vec{Y}$, given by

$$\mathbf{\Gamma} = \mathrm{E}\big[\vec{Y}\vec{Y}^H\big] \tag{A.1}$$

$$= \begin{bmatrix}\mathbf{H}_1 & \mathbf{H}_2\mathbf{P}\end{bmatrix}\begin{bmatrix}\mathbf{H}_1^H \\ \mathbf{P}^H\mathbf{H}_2^H\end{bmatrix} + \sigma_w^2\mathbf{I}_{MK}. \tag{A.2}$$

Similarly, the pseudoautocorrelation $\mathbf{C}$ is given by

$$\mathbf{C} = \mathrm{E}\big[\vec{Y}\vec{Y}^T\big] \tag{A.3}$$

$$= \begin{bmatrix}\mathbf{H}_1 & \mathbf{HP}\end{bmatrix}\begin{bmatrix}\mathbf{P}^T\mathbf{H}^T \\ \mathbf{H}^T\end{bmatrix}. \tag{A.4}$$

Note that $\mathbf{PP}^H = \mathbf{PP}^T = \mathbf{I}$. Since $\mathbf{C} \neq \vec{0}$, $\vec{Y}$ is an improper (non-circular) process and WLE of $\vec{d}_s$ can improve the estimation performance. Compared to a linear estimator, a widely linear estimator jointly processes the received signal and its conjugate to estimate the transmitted data by

$$\hat{\vec{d}}_s = \begin{bmatrix}\mathbf{U} \\ \mathbf{V}\end{bmatrix}^H \begin{bmatrix}\vec{Y} \\ \vec{Y}^*\end{bmatrix}. \tag{A.5}$$

The filter coefficients $\mathbf{U}$ and $\mathbf{V}$ are chosen to minimize the mean squared error (MSE) between $\vec{d}_s$ and $\hat{\vec{d}}_s$ and are solutions to the linear system [PC95]

$$\underbrace{\begin{bmatrix}\mathbf{\Gamma} & \mathbf{C} \\ \mathbf{C}^* & \mathbf{\Gamma}^*\end{bmatrix}}_{\mathbf{F}}\begin{bmatrix}\mathbf{U} \\ \mathbf{V}\end{bmatrix} = \begin{bmatrix}\mathbf{\Phi} \\ \mathbf{\Theta}^*\end{bmatrix}, \tag{A.6}$$

where

$$\mathbf{\Phi} = E\big[\vec{Y}\vec{d}_s^H\big] = \hat{\mathbf{H}}_1 \tag{A.7}$$

and

$$\mathbf{\Theta} = E\left[\vec{Y}\vec{d}_s^T\right] = \hat{\mathbf{H}}_2\mathbf{P}. \tag{A.8}$$

The solution of (A.6) is given by

$$\begin{aligned} \mathbf{U} &= \mathbf{S}^{-1}\left(\mathbf{\Phi} - \mathbf{C}\mathbf{\Gamma}^{-1*}\mathbf{\Theta}^*\right) \\ \mathbf{V} &= \mathbf{S}^{-1*}(\mathbf{\Theta}^* - \mathbf{C}^*\mathbf{\Gamma}^{-1}\mathbf{\Phi}), \end{aligned} \tag{A.9}$$

where $\mathbf{S} = \mathbf{\Gamma} - \mathbf{C}\mathbf{\Gamma}^{-1*}\mathbf{C}^*$ is the Schur complement of $\mathbf{\Gamma}^*$ in $\mathbf{F}$.

Since $\mathbf{H}_i$ is a tall matrix, $\mathbf{\Gamma}$ becomes singular when $\sigma_w \to 0$ and hence a ZF estimation cannot be directly derived. Instead, the system model (4.26) for the widely linear estimation problem is reformulated to a linear estimation problem of double size according to

$$\underbrace{\begin{bmatrix} \vec{Y} \\ \vec{Y}^* \end{bmatrix}}_{\vec{Y}_a^{(j)}} = \mathbf{H}_{\text{eq}} \underbrace{\begin{bmatrix} \vec{d}_s \\ \vec{d}_s^* \end{bmatrix}}_{\vec{d}_a} + \underbrace{\begin{bmatrix} \vec{w} \\ \vec{w}^* \end{bmatrix}}_{\vec{w}_a}, \tag{A.10}$$

where

$$\mathbf{H}_{\text{eq}} = \begin{bmatrix} \mathbf{H}_1 & \hat{\mathbf{H}}_2\mathbf{P} \\ \mathbf{H}_2^*\mathbf{P} & \hat{\mathbf{H}}_1^* \end{bmatrix}. \tag{A.11}$$

The LMMSE estimator for $\vec{d}_a$ in (A.10) is given by

$$\hat{\vec{d}}_{a,\text{MMSE}}^{(j)} = \underbrace{{\mathbf{H}_{\text{eq}}}^H(\mathbf{H}_{\text{eq}}{\mathbf{H}_{\text{eq}}}^H + \sigma_w^2\mathbf{I})^{-1}}_{\mathbf{B}_{\text{MMSE}}}\vec{Y}_a. \tag{A.12}$$

Direct calculation shows that $\mathbf{H}_{\text{eq}}{\mathbf{H}_{\text{eq}}}^H + \sigma_w^2\mathbf{I} = \mathbf{F}$ from (A.6) and hence (A.12) is equivalent to (A.5) and (A.6). Writing the LMMSE estimator in (A.12) to its alternate form [Kay93] results in

$$\hat{\vec{d}}_{a,\text{MMSE}} = (\mathbf{H}_{\text{eq}}{}^H\mathbf{H}_{\text{eq}} + \sigma_w^2\mathbf{I})^{-1}\mathbf{H}_{\text{eq}}{}^H\vec{Y}_a. \tag{A.13}$$

A.2 Uncoded Symbol Error Rate of TRSTC

An approximation of the TR-STC-GFDM SER performance under a frequency-selective fading channel can be derived from an upper bound of symbol error probability for orthogonal maximum ratio combiner [BB99, Ch. 13], but considering the NEF of GFDM. The approximation is given by

$$Pr(\text{Symbol Error}) \approx 4\beta \sum_{i=0}^{JL-1} \binom{JL-1+i}{i} \left(\frac{1+\eta}{2}\right)^i, \tag{A.14}$$

where

$$\beta = \left(\frac{\sqrt{\mathcal{J}}-1}{\sqrt{\mathcal{J}}}\right)\left(\frac{1-\epsilon}{2}\right)^{JL}, \tag{A.15}$$

$$\epsilon = \sqrt{\frac{\frac{3\sigma_e^2}{\mathcal{J}-1}\frac{E_s}{\xi_0 N_0}}{2+\frac{3\sigma_e^2}{\mathcal{J}-1}\frac{E_s}{\xi_0 N_0}}}, \tag{A.16}$$

with E_S and N_0 denoting the average symbol energy and the noise power, respectively. $\mathcal{J}$ denotes the size of the digital constellation, L denotes the number of receive antennas and

$$\sigma_e^2 = \sum_n \mathrm{E}[|h_n|^2] = 1. \tag{A.17}$$

When considering the overhead of the CP of GFDM and OFDM in the effective noise calculation we have

$$\begin{aligned} \xi_{0,\mathrm{OFDM}} &= \tfrac{K+N_{CP}+N_{CS}}{K} \\ \xi_{0,\mathrm{GFDM}} &= \xi \cdot \tfrac{KM+N_{CP}+N_{CS}}{KM}, \end{aligned} \tag{A.18}$$

which shows that GFDM, depending on the NEF ξ from (2.46), can achieve higher spectral efficiency compared to OFDM. This is due to the fact that GFDM requires only one CP for M subsymbols, whereas OFDM uses one CP per OFDM symbol. As in [BB99], (A.14) becomes a tighter upper bound if $JL \geq 2$ and the channel frequency response is flat per subcarrier.

A.3 Proof of (6.17)

Starting from the biased LMMSE estimate of $\vec{D}$ from the received signal $\vec{y}$

$$\eta_D^p = \mu_D^a + \Sigma_D^a \bar{\mathbf{H}}^H(\bar{\mathbf{H}}\Sigma_D^a\bar{\mathbf{H}}^H + \sigma^2\mathbf{I})^{-1}(\vec{y} - \bar{\mathbf{H}}\vec{\mu}_D^a) \tag{A.19}$$

$$\Lambda_D^p = \Sigma_D^a - \Sigma_D^a\bar{\mathbf{H}}^H(\bar{\mathbf{H}}\Sigma_D^a\bar{\mathbf{H}}^H + \sigma^2\mathbf{I})^{-1}\bar{\mathbf{H}}\Sigma_D^a, \tag{A.20}$$

by assuming $\mathbf{H} = \bar{\mathbf{H}}\mathbf{U}^H$,$\vec{\mu}_d^a = \mathbf{U}^H\vec{\mu}_D^a$ and $\Sigma_d^a = \mathbf{U}^H\Sigma_D^a\mathbf{U}$ we calculate

$$\mathbf{U}^H\eta_D^p = \vec{\mu}_d^a + \Sigma_d^a\mathbf{H}^H(\mathbf{H}\Sigma_d^a\mathbf{H}^H + \sigma^2\mathbf{I})^{-1}(y - \mathbf{H}\vec{\mu}_d^a) = \eta_d^p, \tag{A.21}$$

$$\mathbf{U}^H\Lambda_D^p\mathbf{U} = \Sigma_d^a - \Sigma_d^a\mathbf{H}^H(\mathbf{H}\Sigma_d^a\mathbf{H}^H + \sigma^2\mathbf{I})^{-1}\mathbf{H} = \Lambda_d^p \tag{A.22}$$

Note that from (cf. (6.9))

$$(\Sigma_D^p + \Sigma_D^a)^{-1} = \mathrm{diag}(\bar{\mathbf{H}}^H(\bar{\mathbf{H}}\Sigma_D^a\bar{\mathbf{H}}^H + \sigma^2\mathbf{I})^{-1}\bar{\mathbf{H}}) \tag{A.23}$$

directly follows (cf. (6.8))

$$(\Sigma_D^p + \Sigma_D^a)^{-1}(\vec{\mu}_D^p - \vec{\mu}_D^a) = \bar{\mathbf{H}}^H(\bar{\mathbf{H}}\Sigma_D^a\bar{\mathbf{H}}^H + \sigma^2\mathbf{I})^{-1}(\vec{y} - \bar{\mathbf{H}}\vec{\mu}_D^a). \tag{A.24}$$

Now, by substituting (A.24) into (A.21) we end up with

$$\eta_d^p = \mathbf{U}^H\eta_D^p = \vec{\mu}_d^a + \mathbf{U}^H\Sigma_D^a(\Sigma_D^p + \Sigma_D^a)^{-1}(\vec{\mu}_D^p - \vec{\mu}_D^a) \tag{A.25}$$

$$= \vec{\mu}_d^a + \Sigma_d^a\mathbf{U}^H(\mathbf{U}\Sigma_d^a\mathbf{U}^H + \Sigma_D^p)^{-1}(\vec{\mu}_D^p - \mathbf{U}^H\vec{\mu}_d^a). \tag{A.26}$$

Similarly, by using (A.23) in (A.22) we get

$$\Lambda_d^p = \mathbf{U}^H \Lambda_D^p \mathbf{U} = \Sigma_d^a - \mathbf{U}^H \Sigma_D^a (\Sigma_D^p + \Sigma_D^a)^{-1} \Sigma_D^a \mathbf{U} \tag{A.27}$$

$$= \Sigma_d^a - \Sigma_d^a \mathbf{U}^H (\mathbf{U} \Sigma_d^a \mathbf{U}^H + \Sigma_D^p)^{-1} \mathbf{U}^H \Sigma_d^a \tag{A.28}$$

Now, comparing (A.26) and (A.28) with (6.17), the proof is finished.

Publications of the Author

Journal Publications & Book Chapters

[1] **Maximilian Matthe**, Luciano Leonel Mendes, and Gerhard Fettweis. Generalized Frequency Division Multiplexing in a Gabor Transform Setting. *IEEE Communications Letters*, 18(8):1379—-1382, 2014.

[2] **Maximilian Matthe**, Luciano Leonel Mendes, Ivan Gaspar, Nicola Michailow, Dan Zhang, and Gerhard Fettweis. Multi-user time-reversal STC-GFDMA for future wireless networks. *EURASIP Journal on Wireless Communications and Networking*, 2015(1):132, may 2015.

[3] **Maximilian Matthé**, Luciano Mendes, Nicola Michailow, Dan Zhang, and Gerhard Fettweis. Widely Linear Estimation for Space-Time-Coded GFDM in Low-Latency Applications. *IEEE Transactions on Communications*, 63(11):4501–4509, 2015.

[4] **Maximilian Matthé**, Luciano Leonel Mendes, Ivan Gaspar, Nicola Michailow, Dan Zhang, and Gerhard Fettweis. Precoded GFDM Transceiver with Low Complexity Time Domain Processing. *EURASIP Journal on Wireless Communications and Networking*, page 138, 2016.

[5] **Maximilian Matthé** and Gerhard Fettweis. Conjugate root offset-QAM for orthogonal multicarrier transmission. *EURASIP Journal on Advances in Signal Processing*, 2016(1):41, 2016.

[6] **Maximilian Matthé**, Dan Zhang, and Gerhard P. Fettweis. Low-Complexity MMSE-PIC Detection for MIMO-GFDM. *IEEE Transactions on Wireless Communications*, submitted, 2017.

[7] Dan Zhang, **Maximilian Matthé**, Luciano Leonel Mendes, and Gerhard Fettweis. Message Passing Algorithms for Upper and Lower Bounding the Coded Modulation Capacity in a Large-scale Linear System. *IEEE Signal Processing Letters*, 23(4):537–540, 2016.

[8] Nicola Michailow, **Maximilian Matthé**, Ivan Gaspar, A Navarro Caldevilla, Luciano Leonel Mendes, Andreas Festag, and Gerhard Fettweis. Generalized Frequency Division Multiplexing for 5th Generation Cellular Networks. *IEEE Transactions on Communications*, 62(9):3045–3061, 2014.

[9] Ivan Gaspar, **Maximilian Matthe**, Nicola Michailow, Luciano Mendes, Dan Zhang, and Gerhard Fettweis. Frequency-shift Offset-QAM for GFDM. *IEEE Communications Letters*, PP(99):1–1, 2015.

[10] Nicola Michailow, Luciano Mendes, **Maximilian Matthe**, Ivan Gaspar, Andreas Festag, and Gerhard Fettweis. Robust WHT-GFDM for the Next Generation of Wireless Networks. *IEEE Communications Letters*, 19(1):106–109, jan 2015.

[11] Dan Zhang, **Maximilian Matthe**, Luciano Leonel Mendes, and Gerhard P. Fettweis. A Study on the Link Level Performance of Advanced Multicarrier Waveforms under MIMO Wireless Communication Channels. *IEEE Transactions on Wireless Communications*, PP(99), 2017.

Conference Publications

[1] **Maximilian Matthé**, Nicola Michailow, Ivan Gaspar, and Gerhard Fettweis. Influence of Pulse Shaping on Bit Error Rate Performance and Out of Band Radiation of Generalized Frequency Division Multiplexing. In *ICC'14 - Workshop on 5G Technologies (ICC'14 WS - 5G)*, pages 43—-48, Sydney, Australia, 2014.

[2] **Maximilian Matthé**, Luciano Leonel Mendes, and Gerhard Fettweis. Space-Time Coding for Generalized Frequency Division Multiplexing. In *European Wireless 2014 (EW2014)*, Barcelona, Spain, 2014. IEEE.

[3] **Maximilian Matthé**, Luciano Leonel Mendes, and Gerhard P. Fettweis. Asynchronous Multi-User Uplink Transmission with Generalized Frequency Division Multiplexing. In *International Workshop on Advanced PHY and MAC Techniques for Super Dense Wireless Networks (IWSDN) in Conjunction with ICC*, 2015.

[4] **Maximilian Matthé**, Ivan Gaspar, Dan Zhang, and Gerhard Fettweis. Short Paper: Near-ML Detection for MIMO-GFDM. In *Proceedings IEEE 82nd Vehicular Technology Conference*, Boston, 2015.

[5] **Maximilian Matthé**, Ivan S Gaspar, and Gerhard Fettweis. Short Paper: Reduced Complexity Calculation of LMMSE Filter Coefficients. In *Proceedings IEEE 82nd Vehicular Technology Conference*, Boston, 2015.

[6] **Maximilian Matthé**, Dan Zhang, and Gerhard Fettweis. Iterative Detection using MMSE-PIC Demapping for MIMO-GFDM Systems. In *IEEE European Wireless (EW '16)*, 2016.

[7] **Maximilian Matthé**, Dan Zhang, Frank Schaich, Thorsten Wild, Rana Ahmed, and Gerhard P. Fettweis. A Reduced Complexity Time-Domain Transmitter for UF-OFDM. In *2016 IEEE 83rd Vehicular Technology Conference (VTC Spring)*, pages 1–5, Nanjing, China, 2016.

[8] **Maximilian Matthé**, Dan Zhang, and Gerhard P. Fettweis. Sphere-Decoding Aided SIC for MIMO-GFDM: Coded Performance Analysis. In *Wireless Communication Systems (ISWCS), 2016 International Symposium on*, pages 165–169, Poznan, 2016.

[9] Ivan Gaspar, Luciano Leonel Mendes, **Maximilian Matthé**, Nicola Michailow, and Gerhard Fettweis. LTE-compatible 5G PHY based on Generalized Frequency Division Multiplexing. In *Proceedings of the The Eleventh International Symposium on Wireless Communication Systems (ISWCS'14)*, 2014.

[10] Dan Zhang, **Maximilian Matthé**, Luciano Leonel Mendes, and Gerhard Fettweis. A Markov Chain Monte Carlo Algorithm for Near-Optimum Detection of MIMO-GFDM Signals. In *IEEE 26th International Symposium on Personal, Indoor and Mobile Radio Communications - (PIMRC '15)*, pages 281–286, 2015.

[11] Albrecht Wolf, **Maximilian Matthe**, and Gerhard Fettweis. Improved source correlation estimation in wireless sensor networks. In *2015 IEEE International Conference on Communication Workshop (ICCW)*, pages 2121–2126. IEEE, jun 2015.

[12] Gerhard Wunder, Martin Kasparick, Thorsten Wild, Frank Schaich, Yejian Chen, Marcin Dryjanski, Mateusz Buczkowski, Slawomir Pietrzyk, Nicola Michailow, **Maximilian Matthe**, Ivan Gaspar, Luciano Mendes, Andreas Festag, Gerhard Fettweis, Jean-Baptiste Dore, Nicolas Cassiau, Dimitri Ktenas, Vincent Berg, Bertalan Eged, and Peter Vago. 5GNOW: Intermediate frame structure and transceiver concepts. In *2014 IEEE Globecom Workshops (GC Wkshps)*, pages 565–570. IEEE, dec 2014.

[13] Shahab Ehsanfar, **Maximilian Matthé**, Dan Zhang, and Gerhard P. Fettweis. Theoretical Analysis and CRLB Evaluation for Pilot-aided Channel Estimation in GFDM. In *Proceedings of the IEEE Globecom 2016*, 2016.

[14] Shahab Ehsanfar, **Maximilian Matthe**, Dan Zhang, Gerhard Fettweis, and Ieee Fellow. A Study of Pilot-Aided Channel Estimation in MIMO-GFDM Systems. In *IEEE Workshop on Smart Antennas (IEEE WSA) '16*, pages 202—-209, 2016.

[15] Albrecht Wolf, **Maximilian Matthe**, Andreas Festag, and Gerhard Fettweis. Outage based power allocation for a lossy-forwarding relaying system. In *Computer Aided Modelling and Design of Communication Links and Networks (CAMAD), 2015 IEEE 20th International Workshop on*, pages 267—-272, 2015.

[16] Martin Danneberg, Nicola Michailow, Ivan Gaspar, **Maximilian Matthe**, Dan Zhang, Luciano Leonel Mendes, and Gerhard Fettweis. Implementation of a 2 by 2 MIMO-GFDM Transceiver for Robust 5G Networks. In *Proceedings of the Twelfth International Symposium on Wireless Communication Systems (ISWCS'15)*, Brussels, 2015.

Bibliography

[3GP17] 3GPP. 3GPP, 2017.

[AD01] N. Al-Dhahir. Single-carrier frequency-domain equalization for space-time block-coded transmissions over frequency-selective fading channels. *IEEE Communications Letters*, 5(7):304–306, jul 2001.

[AEVZ02] E. Agrell, T. Eriksson, A. Vardy, and K. Zeger. Closest point search in lattices. *IEEE Transactions on Information Theory*, 48(8):90–107, 2002.

[AF16] Esther P. Adeva and Gerhard P. Fettweis. Efficient Architecture for Soft-Input Soft-Output Sphere Detection With Perfect Node Enumeration. *IEEE Transactions on Very Large Scale Integration (VLSI) Systems*, pages 1–14, 2016.

[AFB11] Pooyan Amini and Behrouz Farhang-Boroujeny. Design and performance evaluation of filtered multitone (FMT) in doubly dispersive channels. *IEEE International Conference on Communications*, 2011.

[AFRFB15] Amir Aminjavaheri, Arman Farhang, Ahmad RezazadehReyhani, and Behrouz Farhang-Boroujeny. Impact of Timing and Frequency Offsets on Multicarrier Waveform Candidates for 5G. *arXiv:1505.00800 [cs, math]*, pages 178–183, 2015.

[AJM15] Javad Abdoli, Ming Jia, and Jianglei Ma. Filtered OFDM: A new waveform for future wireless systems. *IEEE Workshop on Signal Processing Advances in Wireless Communications, SPAWC*, 2015-Augus:66–70, 2015.

[AKR16] Changyoung An, Byeongjae Kim, and Heung-Gyoon Ryu. Design of W-OFDM and Nonlinear Performance Comparison for 5G Waveform. In *2016 International Conference on Information and Communication Technology Convergence (ICTC)*, pages 1006–1009, 2016.

[Ala98] S.M. Alamouti. A simple transmit diversity technique for wireless communications. *IEEE Journal on Selected Areas in Communications*, 16(8):1451–1458, 1998.

[ALA14] Dominik Auras, Rainer Leupers, and Gerd H. Ascheid. A novel reduced-complexity soft-input soft-output MMSE MIMO detector: Algorithm and efficient VLSI architecture. In *2014 IEEE International Conference on Communications, ICC 2014*, pages 4722–4728, 2014.

[ARÖ13] Jon B Anderson, Fredrik Rusek, and Viktor Öwall. Faster-than-Nyquist signaling. *Proceedings of the IEEE*, 101(8):1815–1816, 2013.

[Bal81] R Balian. Un principe d'incertitude fort en théorie du signal ou en mécanique quantique. *C.R. Acad. Sc. Paris*, 292:1357–1361, 1981.

[Bas98] Martin J. Bastiaans. *Gabor's expansion and the Zak transform for continuous-time and discrete-time signals*, volume 7 of *Wavelet Analysis and Its Applications*. Elsevier, 1998.

[BB99] Sergio Benedetto and Ezio Biglieri. Principles of Digital Transmission: With Wireless Applications. jul 1999.

[BBC+14] Paolo Banelli, Stefano Buzzi, Giulio Colavolpe, Andrea Modenini, Fredrik Rusek, and Alessandro Ugolini. Modulation formats and waveforms for 5G networks: Who will be the heir of OFDM?: An overview of alternative modulation schemes for improved spectral efficiency. *IEEE Signal Processing Magazine*, 31(6):80–93, 2014.

[BC12] Lin Bai and Jinho Choi. *Low Complexity MIMO Detection*. Springer US, 2012.

[BDM15] S K Bandari, A Drosopoulos, and V V Mani. Exact SER Expressions of GFDM in Nakagami-m and Rician fading channels. In *European Wireless 2015; 21th European Wireless Conference; Proceedings of*, pages 1–6, 2015.

[BDMP98] Sergio Benedetto, Dariush Divsalar, Guido Montorsi, and Fabrizio Pollara. Serial concatenation of interleaved codes: Performance analysis,design, and iterative decoding. *IEEE Transactions on Information Theory*, 44(3):909–926, 1998.

[Bel10] M Bellanger. FBMC physical layer: a primer. Technical report, PHYDYAS, 2010.

[Ber93] Claude Berrou. Near Shanon Limit error correctin coding and decoding Turbo Codes. In *Communications, 1993. ICC '93 Geneva. Technical Program, Conference Record, IEEE International Conference on*, 1993.

[BG96] Martin J. Bastiaans and Marc C.W. Geilen. On the discrete Gabor transform and the discrete Zak transform. *Signal Processing*, 49(3):151–166, mar 1996.

[BGZ75] H. Bacry, A. Grossmann, and J. Zak. Proof of completeness of lattice states in the k q representation. *Physical Review B*, 12(4):1118–1120, 1975.

[BH97] H. Bolcskei and F. Hlawatsch. Discrete Zak transforms, polyphase transforms, and applications. *IEEE Transactions on Signal Processing*, 45(4):851–866, apr 1997.

[BHW98] John J Benedetto, Christopher Heil, and David F Walnut. Gabor Systems and the Balian-Low Theorem. In Hans G. Feichtinger and Thomas Strohmer, editors, *Gabor Analysis and Algorithms*, chapter 2, pages 85–122. Birkhäuser, 1998.

[Bin90] John A C Bingham. Multicarrier Modulation for Data Transmission: An Idea Whose Time Has Come. *IEEE Communications Magazine*, 28(5):5–14, 1990.

[BKS07] C. Bekas, E. Kokiopoulou, and Y. Saad. An estimator for the diagonal of a matrix. *Applied Numerical Mathematics*, 57(11-12):1214–1229, 2007.

[BMDP97] S Benedetto, G Montorsi, D Divsalar, and F Pollara. Iterative Decoding of Serially Concatenated Codes with Interleavers and Comparison with Turbo Codes. *Proc.˜IEEE Global Telecommunications Conference*, pages 654–658, 1997.

[Böl03] Helmut Bölcskei. Orthogonal Frequency Division Multiplexing Based on Offset QAM. In Hans G. Feichtinger and Thomas Strohmer, editors, *Advances in Gabor Analysis*, pages 321—-352. Birkhäuser, 2003.

[Bre03] D. G. Brennan. Linear diversity combining techniques. *Proceedings of the IEEE*, 91(2):331–356, 2003.

[Bri01] Stephan Ten Brink. Convergence behavior of iteratively decoded parallel concatenated codes. *IEEE Transactions on Communications*, 49(10):1727–1737, 2001.

[Bru13] Luciano Leonel Mendes Bruno M Alves. Performance of GFDM over Frequency-Selective Channels -Invited Paper. *Telecomunicações*, 2013.

[BS08] I N Bronstein and K A Semendjajew. *Taschenbuch der Mathematik*. Harri Deutsch, 2008.

[CEÖ02] Giovanni Cherubini, Evangelos Eleftheriou, and Sedat Ölçer. Filtered multitone modulation for very high-speed digital subscriber lines. *IEEE Journal on Selected Areas in Communications*, 20(5):1016–1028, 2002.

[CGE03] Severine Catreux, Larry J. Greenstein, and Vinko Erceg. Some results and insights on the performance gains of MIMO systems. *IEEE Journal on Selected Areas in Communications*, 21(5):839–847, 2003.

[Cha66] R W Chang. Synthesis of Band-Limited Orthogonal Signals for Multichannel Data Transmission. *The Bell Systems Technical Journal*, 45(10):1775–1796, 1966.

[Chr03] Ole Christensen. *An Introduction To Frames And Riesz Bases*. Springer, 2003.

[CPN14] Marius Caus and Ana I. Perez-Neira. Multi-stream transmission for highly frequency selective channels in MIMO-FBMC/OQAM systems. *IEEE Transactions on Signal Processing*, 62(4):786–796, 2014.

[CR01] Aik Chindapol and James A Ritcey. Design , Analysis , and Performance Evaluation for BICM-ID with Square QAM Constellations in Rayleigh Fading Channels. *IEEE Journal on Selected Areas in Communications*, 19(5):944–957, 2001.

[CS99] John Conway and Neil J. A. Slone. *Sphere Packings, Lattices and Groups*. Springer US, New York, 1999.

[CSH17] Po Chih Chen, Borching Su, and Yenming Huang. Matrix Characterization for GFDM: Low Complexity MMSE Receivers and Optimal Filters. *IEEE Transactions on Signal Processing*, 65(18):4940–4955, 2017.

[CTB98] Giuseppe Caire, Giorgio Taricco, and Ezio Biglieri. Bit-Interleaved Coded Modulation. *IEEE Transactions on Information Theory*, 44(3):927–946, 1998.

[Dau90] I Daubechies. The wavelet transform, time-frequency localization and signal analysis. *Information Theory, IEEE Transactions on*, 36(5):961–1005, sep 1990.

[DBD17] Johannes Demel, Carsten Bockelmann, and Armin Dekorsy. Evaluation of a software defined GFDM implementation for industry 4.0 applications. In *Proceedings of the IEEE International Conference on Industrial Technology*, pages 1283–1288, 2017.

[DJJ91] Ingrid Daubechies, Stéphane Jaffard, and Jean-Lin Journé. A Simple Wilson Orthonormal Basis with Exponential Decay. *SIAM Journal on Mathematical Analysis*, 22(2):554–573, mar 1991.

[DMG+15] Martin Danneberg, Nicola Michailow, Ivan Gaspar, Maximilian Matthe, Dan Zhang, Luciano Leonel Mendes, and Gerhard Fettweis. Implementation of a 2 by 2 MIMO-GFDM Transceiver for Robust 5G Networks. In *Proceedings of the Twelfth International Symposium on Wireless Communication Systems (ISWCS'15)*, Brussels, 2015.

[DMG+16] Martin Danneberg, Nicola Michailow, Ivan Gaspar, Dan Zhang, and Gerhard Fettweis. Short Paper: Flexible GFDM implementation in FPGA with support to run-time reconfiguration. In *2015 IEEE 82nd Vehicular Technology Conference, VTC Fall 2015 - Proceedings*, pages 1–2, 2016.

[DT15] S S Das and S Tiwari. Discrete Fourier transform spreading-based generalised frequency division multiplexing. *IEEE Electronics Letters*, 51(10), 2015.

[Eri17] Ericsson. 5G systems - Enabling the Transformation of Industry and Society. Technical report, Ericsson, 2017.

[FB11] Behrouz Farhang-Boroujeny. OFDM Versus Filter Bank Multicarrier. *IEEE Signal Processing Magazine*, 28(3):92–112, may 2011.

[FBM15] Behrouz Farhang-Boroujeny and Hussein Moradi. Derivation of GFDM based on OFDM principles. In *2015 IEEE International Conference on Communications (ICC)*, pages 2680–2685. IEEE, jun 2015.

[FCC13] FCC. Part 90 - Private and Land Mobile Radio Service. Technical report, FCC, 2013.

[FCC17] FCC. Specialized Mobile Radio Service (SMR), 2017.

[Fet14] Gerhard P. Fettweis. The Tactile Internet: Applications and Challenges. *IEEE Vehicular Technology Magazine*, 9(1):64–70, mar 2014.

[FKB09] Gerhard Fettweis, Marco Krondorf, and Steffen Bittner. GFDM - Generalized Frequency Division Multiplexing. In *VTC Spring 2009 - IEEE 69th Vehicular Technology Conference*, pages 1–4. IEEE, apr 2009.

[FMD15a] Arman Farhang, Nicola Marchetti, and Linda E. Doyle. Low Complexity Modem Design for GFDM. *IEEE Transactions on Signal Processing*, PP(99):1–1, 2015.

[FMD15b] Arman Farhang, Nicola Marchetti, and Linda E. Doyle. Low Complexity Transceiver Design for GFDM. *ArXiv e-prints*, page 12, 2015.

[FMFM14] Arman Farhan, Nicola Marchetti, Fabricio Figueiredo, and Joao Paulo Miranada. Massive MIMO and Waveform Design for 5th Generation Wireless Communication Systems. *Proceedings of the 1st International Conference on 5G for Ubiquitous Connectivity*, pages 70–75, 2014.

[FS98] Hans Georg Feichtinger and Thomas Strohmer, editors. *Gabor Analysis and Algorithms: Theory and Applications*. Birkhäuser, 1998.

[FS02] Hans Georg Feichtinger and Thomas Strohmer, editors. *Advances in Gabor Analysis (Applied and Numerical Harmonic Analysis)*. Birkhäuser, 2002.

[Gab47] D. Gabor. Theory of communication. *J. IEE*, 93(26):429–457, 1947.

[GBB+17] Robin Gerzaguet, Nikolaos Bartzoudis, Leonardo Gomes Baltar, Vincent Berg, Jean-baptiste Doré, Dimitri Kténas, Oriol Font-bach, Xavier Mestre, Miquel Payaró, Michael Färber, and Kilian Roth. The 5G candidate waveform race : a comparison of complexity and performance. *EURASIP Journal on Wireless Communications and Networking*, 13, 2017.

[GKCD16] R Gerzaguet, D Kténas, N Cassiau, and J-B Doré. Comparative study of 5G waveform candidates for below 6GHz air interface. In *ETSI Workshop on Future Radio Technologies, Air Interfaces*, pages 1–9, 2016.

[GL96] Gene H. Golub and Charles F. Van Loan. *Matrix Computations*. John Hopkins University Press, 1996.

[GMM+15] Ivan Gaspar, Maximilian Matthe, Nicola Michailow, Luciano Mendes, Dan Zhang, and Gerhard Fettweis. Frequency-shift Offset-QAM for GFDM. *IEEE Communications Letters*, PP(99):1–1, 2015.

[GMP17] Danilo Gaspar, Luciano Mendes, and Tales Pimenta. GFDM BER under Synchronization Errors. *IEEE Communications Letters*, 21(8):1743–1746, 2017.

[GN06] Zhan Guo and Peter Nilsson. Algorithm and implementation of the K-best Sphere decoding for MIMO detection. *IEEE Journal on Selected Areas in Communications*, 24(3):491–503, 2006.

[GNN+13] I S Gaspar, Michailow N., A Navarro Caldevilla, E Ohlmer, S Krone, and G Fettweis. Low Complexity GFDM Receiver Based On Sparse Frequency Domain Processing. In *Vehicular Technology Conference, 2013. VTC Spring 2013, IEEE 77th*, 2013.

[GOS+02] W.H. Gerstacker, F. Obernosterer, R. Schober, A. Lehmann, A. Lampe, and P. Gunreben. Widely linear equalization for space-time block-coded transmission over fading ISI channels. In *Proceedings IEEE 56th Vehicular Technology Conference*, volume 1, pages 238–242. IEEE, 2002.

[Grö01] Karlheinz Gröchenig. *Foundations of Time-Frequency Analysis*. Birkhäuser, 2001.

[GWT+17] Peng Guan, Dan Wu, Tingjian Tian, Jianwei Zhou, Xi Zhang, Liang Gu, Anass Benjebbour, Masashi Iwabuchi, and Yoshihisa Kishiyama. 5G Field Trials - OFDM-based Waveforms and Mixed Numerologies. *IEEE Journal on Selected Areas in Communications*, PP(99), 2017.

[HL05] Sh Han and Jh Lee. An overview of peak-to-average power ratio reduction techniques for multicarrier transmission. *Wireless Communications, IEEE*, 12(2):56–65, 2005.

[HL15] Mario Huemer and Oliver Lang. On component-wise conditionally unbiased linear Bayesian estimation. *Conference Record - Asilomar Conference on Signals, Systems and Computers*, 2015-April:879–885, 2015.

[HLH17] Mario Huemer, Oliver Lang, and Christian Hofbauer. Component-wise conditionally unbiased widely linear MMSE estimation. *Signal Processing*, 133(October 2016):227–239, 2017.

[HN05] Man Kiu Ho and Michael K. Ng. Splitting iterations for circulant-plus-diagonal systems. *Numerical Linear Algebra with Applications*, 12(8):779–792, 2005.

[HSL17] Seungyul Han, Youngchul Sung, and Yong H. Lee. Filter Design for Generalized Frequency-Division Multiplexing. *IEEE Transactions on Signal Processing*, 65(7):1644–1659, 2017.

[HW89] Christopher Heil and David Walnut. Continuous and discrete wavelet transforms. *SIAM Review*, 31(4):628–666, 1989.

[IEE09] IEEE. 802.11n-2009 - IEEE Standard for Information technology– Local and metropolitan area networks– Specific requirements– Part 11: Wireless LAN Medium Access Control (MAC)and Physical Layer (PHY) Specifications Amendment 5: Enhancements for Higher Throughp. Technical report, IEEE, 2009.

[Jan88] A. J. E. M. Janssen. The Zak transform : a signal transform for sampled time-continuous signals. *Philips Journal of Research*, 43(1):23–69, 1988.

[Jan97] A J E M Janssen. From continuous to discrete {W}eyl-{H}eisenberg frames through sampling. *J. Fourier Anal. Appl.*, 3(5):583–596, 1997.

[Jan98] A. Janssen. The duality condition for Weyl-Heisenberg frames. In *Gabor analysis and algorithms*, pages 33–84. Birkhäuser, 1998.

[JKL+17] Hyoungju Ji, Younsun Kim, Juho Lee, Eko Onggosanusi, Younghan Nam, Jianzhong Zhang, Byungju Lee, and Byonghyo Shim. Overview of Full-Dimension MIMO in LTE-Advanced Pro. *IEEE Communications Magazine*, -(February):176–184, 2017.

[Kay93] S M Kay. *Fundamentals of Statistical Signal Processing: Estimation Theory*. Number v. 1 in Prentice Hall Signal Processing Series. Prentice Hall, 1993.

[KDMB02] Shohreh Kasaei, Mohamed Deriche, Senior Member, and Boualem Boashash. A Novel Fingerprint Image Compression Technique Using Wavelets Packets and Pyramid Lattice Vector Quantization. *IEEE Transactions on Image Processing*, 11(12):1365–1378, 2002.

[Kit04] Charles Kittel. *Introduction to Solid State Physics, 8th Edition*. Wiley, 8th editio edition, 2004.

[KLF07] Alexander Kocian, Ingmar Land, and Bernard H. Fleury. Joint Channel Estimation, Partial Successive Interference Cancellation, and Data Decoding for DS-CDMA Based on the SAGE Algorithm. *IEEE Transactions on Communications*, 55(6):1231—-1241, 2007.

[KWJM14] Martin Kasparick, Gerhard Wunder, Peter Jung, and Dick Maryopi. Biorthogonal Waveforms for 5G Random Access with Short Message Support, 2014.

[Lee16] Larry Leemis. Minimum of i.i.d. Rayleigh Variables. Technical report, College of William & Mary, Williamsburg, Virginia, 2016.

[LK17] Byungju Lim and Young Chai Ko. SIR Analysis of OFDM and GFDM Waveforms with Timing Offset, CFO and Phase Noise. *IEEE Transactions on Wireless Communications*, 16(10):6979–6990, 2017.

[LLJ+15] Long Bao Le, Vincent Lau, Eduard Jorswieck, Ngoc-Dung Dao, Afshin Haghighat, Dong In Kim, and Tho Le-Ngoc. Enabling 5G mobile wireless technologies. *EURASIP Journal on Wireless Communications and Networking*, 2015(1):218, 2015.

[LMLS14] Lu Lu, Student Member, Geoffrey Ye Li, and A Lee Swindlehurst. An Overview of Massive MIMO : Bene fi ts and Challenges. *Ieee Journal of Selected Topics in Signal Processing*, 8(5):742–758, 2014.

[LQ15] Mzabalazo Lupupa and Jian Qi. I/Q imbalance in generalized frequency division multiplexing under Weibull fading. In *IEEE International Symposium on Personal, Indoor and Mobile Radio Communications, PIMRC*, volume 2015-Decem, pages 471–476, 2015.

[LR98] Xiaodong Li and J.A. Ritcey. Bit-interleaved coded modulation with iterative decoding using soft feedback. *IEEE Electronics Letters*, 34(10):942–943, 1998.

[LS14] Hao Lin and Pierre Siohan. Multi-carrier modulation analysis and WCP-COQAM proposal. *EURASIP Journal on Advances in Signal Processing*, 2014(1):79, 2014.

[LW00] K.F. Lee and D.B. Williams. A space-frequency transmitter diversity technique for OFDM systems. *Globecom '00 - IEEE. Global Telecommunications Conference. Conference Record (Cat. No.00CH37137)*, 3:1473–1477, 2000.

[LW16] David W. Lin and Po Sen Wang. On the configuration-dependent singularity of GFDM pulse-shaping filter banks. *IEEE Communications Letters*, 20(10):1975–1978, 2016.

[Maz75] J E Mazo. Faster-than-Nyquist signaling. *The Bell Systems Technical Journal*, 54(8), 1975.

[MBH13] Gerald Matz, Helmut Bolcskei, and Franz Hlawatsch. Time-Frequency Foundations of Communications: Concepts and Tools. *IEEE Signal Processing Magazine*, 30(6):87–96, nov 2013.

[MDD+02] Bertrand Muquet, Marc De Courville, Pierre Duhamel, Georgios B. Giannakis, and Pierre Magniez. Turbo demodulation of zero-padded OFDM transmissions. *IEEE Transactions on Communications*, 50(11):1725–1728, 2002.

[MF16] Maximilian Matthé and Gerhard Fettweis. Conjugate root offset-QAM for orthogonal multicarrier transmission. *EURASIP Journal on Advances in Signal Processing*, 2016(1):41, 2016.

[MGF15] Maximilian Matthé, Ivan S Gaspar, and Gerhard Fettweis. Short Paper: Reduced Complexity Calculation of LMMSE Filter Coefficients. In *Proceedings IEEE 82nd Vehicular Technology Conference*, Boston, 2015.

[MGK+12] Nicola Michailow, Ivan Gaspar, Stefan Krone, Michael Lentmaier, and Gerhard Fettweis. Generalized frequency division multiplexing: Analysis of an alternative multi-carrier technique for next generation cellular systems. In *2012 International Symposium on Wireless Communication Systems (ISWCS)*, pages 171–175. IEEE, aug 2012.

[MGZF15] Maximilian Matthé, Ivan Gaspar, Dan Zhang, and Gerhard Fettweis. Short Paper: Near-ML Detection for MIMO-GFDM. In *Proceedings IEEE 82nd Vehicular Technology Conference*, Boston, 2015.

[MH11] Gerald Matz and Franz Hlawatsch. Fundamentals of time-varying communication channels. In *Wireless Communications Over Rapidly Time-Varying Channels*, pages 1–63. Academic Press, 2011.

[MKLF12] Nicola Michailow, Stefan Krone, Michael Lentmaier, and Gerhard Fettweis. Bit Error Rate Performance of Generalized Frequency Division Multiplexing. In *2012 IEEE Vehicular Technology Conference (VTC Fall)*, pages 1–5. IEEE, sep 2012.

[MLRF11] N Michailow, M Lentmaier, P Rost, and G Fettweis. Integration of a {GFDM} secondary system in an {OFDM} primary system. In *Future Network Mobile Summit (FutureNetw), 2011*, pages 1–8, 2011.

[MMF14a] Maximilian Matthe, Luciano Leonel Mendes, and Gerhard Fettweis. Generalized Frequency Division Multiplexing in a Gabor Transform Setting. *IEEE Communications Letters*, 18(8):1379—-1382, 2014.

[MMF14b] Maximilian Matthé, Luciano Leonel Mendes, and Gerhard Fettweis. Space-Time Coding for Generalized Frequency Division Multiplexing. In *European Wireless 2014 (EW2014)*, Barcelona, Spain, 2014. IEEE.

[MMG+14] Nicola Michailow, Maximilian Matthé, Ivan Gaspar, A Navarro Caldevilla, Luciano Leonel Mendes, Andreas Festag, and Gerhard Fettweis. Generalized Frequency Division Multiplexing for 5th Generation Cellular Networks. *IEEE Transactions on Communications*, 62(9):3045–3061, 2014.

[MMG+15] Maximilian Matthe, Luciano Leonel Mendes, Ivan Gaspar, Nicola Michailow, Dan Zhang, and Gerhard Fettweis. Multi-user time-reversal STC-GFDMA for future wireless networks. *EURASIP Journal on Wireless Communications and Networking*, 2015(1):132, may 2015.

[MMG+16] Maximilian Matthé, Luciano Leonel Mendes, Ivan Gaspar, Nicola Michailow, Dan Zhang, and Gerhard Fettweis. Precoded GFDM Transceiver with Low Complexity Time Domain Processing. *EURASIP Journal on Wireless Communications and Networking*, page 138, 2016.

[MMGF14] Maximilian Matthé, Nicola Michailow, Ivan Gaspar, and Gerhard Fettweis. Influence of Pulse Shaping on Bit Error Rate Performance and Out of Band Radiation of Generalized Frequency Division Multiplexing. In *ICC'14 - Workshop on 5G Technologies (ICC'14 WS - 5G)*, pages 43—-48, Sydney, Australia, 2014.

[MMM+15] Maximilian Matthé, Luciano Mendes, Nicola Michailow, Dan Zhang, and Gerhard Fettweis. Widely Linear Estimation for Space-Time-Coded GFDM in Low-Latency Applications. *IEEE Transactions on Communications*, 63(11):4501–4509, 2015.

[MZF16a] Maximilian Matthé, Dan Zhang, and Gerhard Fettweis. Iterative Detection using MMSE-PIC Demapping for MIMO-GFDM Systems. In *IEEE European Wireless (EW '16)*, 2016.

[MZF16b] Maximilian Matthé, Dan Zhang, and Gerhard P. Fettweis. Sphere-Decoding Aided SIC for MIMO-GFDM: Coded Performance Analysis. In *Wireless Communication Systems (ISWCS), 2016 International Symposium on*, pages 165–169, Poznan, 2016.

[MZSR17] Y. Medjahdi, R. Zayani, H. Shaiek, and D. Roviras. WOLA processing: A useful tool for windowed waveforms in 5G with relaxed synchronicity. In *2017 IEEE International Conference on Communications Workshops, ICC Workshops 2017*, pages 393–398, 2017.

[(NA] The Numerical Algorithms Group (NAG). The NAG Library.

[Nag17] Satoshi Nagata. 3GPP TSG RAN WG1 Meeting #88 Chairman's Notes. Technical Report April, 3GPP, 2017.

[NGM15] NGMN. 5G White Paper. Technical report, NGMN, 2015.

[NMZF17] Ahmad Nimr, Maximilian Matthe, Dan Zhang, and Gerhard Fettweis. Optimal Radix-2 FFT Compatible Filters for GFDM. *IEEE Communications Letters*, PP(99):1–1, 2017.

[NSC00] A.F. Naguib, N. Seshadri, and A.R. Calderbank. Increasing data rate over wireless channels. *IEEE Signal Processing Magazine*, 17(3):76–92, 2000.

[NZMF17] Ahmad Nimr, Dan Zhang, Ana-belen Martinez, and Gerhard Fettweis. A Study on the Physical Layer Performance of GFDM for High Throughput Wireless Communication. In *25th European Signal Processing Conference (EUSIPCO)*, pages 668–672, 2017.

[ÖBÇ17] Ersin Öztürk, Ertugrul Basar, and Hakan Ali Çirpan. Spatial modulation GFDM: A low complexity MIMO-GFDM system for 5G wireless networks. *2016 IEEE International Black Sea Conference on Communications and Networking, BlackSeaCom 2016*, 2017.

[OPF12] Luis G. Ordóñez, Daniel P. Palomar, and Javier Rodríguez Fonollosa. Array gain in the DMT framework for MIMO channels. *IEEE Transactions on Information Theory*, 58(7):4577–4593, 2012.

[Orr92] R.S. Orr. Finite discrete Gabor transform relations under periodization and sampling. In *[1992] Proceedings of the IEEE-SP International Symposium on Time-Frequency and Time-Scale Analysis*, pages 395–398. IEEE, 1992.

[Orr93] Richard S. Orr. Derivation of the finite discrete Gabor transform by periodization and sampling. *Signal Processing*, 34(1):85–97, oct 1993.

[PC95] B. Picinbono and P. Chevalier. Widely linear estimation with complex data. *IEEE Transactions on Signal Processing*, 43(8):2030–2033, 1995.

[Pei14] Chris Peikert. Lattice Cryptography for the Internet. In *International Workshop on Post-Quantum Cryptography*, volume 8772, pages 197–219, 2014.

[Pen15] Jyrki T. J. Penttinen, editor. *The LTE-Advanced Deployment Handbook*. Wiley, 2015.

[Pro95] J G Proakis. *Digital communications*. Communications and signal processing. McGraw-Hill Higher Education, 1995.

[PSM06] Stephan Pfletschinger, Frieder Sanzi, and A System Model. Error Floor Removal for Bit-Interleaved Coded Modulation with Iterative Detection. *IEEE Transactions on Wireless Communications*, 5(11):3174–3181, 2006.

[PTVF07] William H Press, Saul A Teukolsky, William T Vetterling, and Brian P Flannery. *Numerical Recipes 3rd Edition: The Art of Scientific Computing*. Cambridge University Press, New York, NY, USA, 3 edition, 2007.

[Qiu95] Sigang Qiu. Block-circulant Gabor-matrix structure and discrete Gabor transforms. *Optical Engineering*, 34(10):2872, oct 1995.

[RA09] Ffredrik Rusek and John B. Anderson. Constrained capacities for faster-than-nyquist signaling. *IEEE Transactions on Information Theory*, 55(2):764–775, 2009.

[Rah93] Moe Rahnema. Overview Of The GSM System and Protocol Architecture. *IEEE Communications Magazine*, 31(4):92–100, 1993.

[RHG11] Marco Renzo, Harald Haas, and Peter Grant. Spatial modulation for multiple-antenna wireless systems: a survey. *IEEE Communications Magazine*, 49(12):182–191, 2011.

[Ric00a] K W Richardson. UMTS overview. *Electronics & Communication Engineering Journal*, 12(3):93—-100, 2000.

[Ric00b] Tom Richardson. The Geometry of Turbo-Decoding Dynamics. *IEEE TRANSACTIONS ON INFORMATION THEORY*, 46(1):457–515, 2000.

[RL09] William Ryan and Shu Lin. *Channel Codes: Classical and Modern*. Cambridge University Press, 2009.

[RS97] Amos Ron and Zuowei Shen. Weyl-Heisenberg frames and Riesz bases in L2(R). *Duke Mathematical Journal*, 89(2):237–282, 1997.

[RU00] Thomas Richardson and Rudiger Urbanke. Thresholds for Turbo Codes. In *ISIT*, volume 45, 2000.

[RU01] Thomas J Richardson and R L Urbanke. The Capacity of low-density-parity-check codes under message-passing decoding. *IEEE TRANSACTIONS ON INFORMATION THEORY*, 47(2):599–618, 2001.

[SA05] Marvin K. Simon and Mohamed-Slim Alouini. *Digital Communication over Fading Channels, 2nd Edition*. Wiley, 2005.

[SAD+16] Meryem Simsek, Adnan Aijaz, Mischa Dohler, Joachim Sachs, and Gerhard Fettweis. 5G-Enabled Tactile Internet. *IEEE Journal on Selected Areas in Communications*, 8716(c):1–1, 2016.

[Sal67] B Saltzberg. Performance of an Efficient Parallel Data Transmission System. *Communication Technology, IEEE Transactions on*, 15(6):805–811, 1967.

[SB10] Christoph Studer and Helmut Bolcskei. SoftâĂŞInput SoftâĂŞOutput Single Tree-Search Sphere Decoding. *IEEE Transactions on Information Theory*, 56(10):4827–4842, oct 2010.

[SE94] C. P. Schnorr and M. Euchner. Lattice basis reduction: Improved practical algorithms and solving subset sum problems. *Mathematical Programming*, 66(1-3):181–199, 1994.

[SFS11] Christoph Studer, Schekeb Fateh, and Dominik Seethaler. ASIC implementation of soft-input soft-output MIMO detection using MMSE parallel interference cancellation. *IEEE Journal of Solid-State Circuits*, 46(7):1754–1765, 2011.

[SKS+16] Houssem Sifaou, Abla Kammoun, Luca Sanguinetti, Mérouane Debbah, and Mohamed-Slim Alouini. Max-Min SINR in Large-Scale Single-Cell MU-MIMO: Asymptotic Analysis and Low Complexity Transceivers. *IEEE TRANSACTIONS ON SIGNAL PROCESSING*, 65(7):1–13, 2016.

[SM15] Lukas Sendrei and Stanislav Marchevski. Nonlinear Noise Estimation and Compensation in GFDM Based Communication Systems for Cognitive Radio Networks. In *2015 25th International Conference Radioelektronika (RADIOELEKTRONIKA)*, pages 313–316, 2015.

[SMMF14] Lukas Sendrei, Stanislav Marchevski, Nicola Michailow, and Gerhard P. Fettweis. Iterative Receiver for Clipped GFDM Signals. In *2014 24th International Conference Radioelektronika*, pages 14–17, 2014.

[SSL02] P. Siohan, C. Siclet, and N. Lacaille. Analysis and design of OFDM/OQAM systems based on filterbank theory. *Signal Processing, IEEE Transactions on*, 50(5):1170–1183, may 2002.

[Str98] Thomas Strohmer. Numerical Algorithms for discrete Gabor Expansions. In H.G. Feichtinger and Thomas Strohmer, editors, *Gabor Analysis and Algorithms*, chapter 8, pages 267–294. Birkhäuser, 1998.

[SW14] Frank Schaich and Thorsten Wild. Relaxed synchronization support of universal filtered multi-carrier including autonomous timing advance. In *2014 11th International Symposium on Wireless Communications Systems (ISWCS)*, pages 203–208. IEEE, aug 2014.

[SWC14] Frank Schaich, Thorsten Wild, and Yejian Chen. Waveform Contenders for 5G - Suitability for Short Packet and Low Latency Transmissions. In *2014 IEEE 79th Vehicular Technology Conference (VTC Spring)*, pages 1–5. IEEE, may 2014.

[SZÖ+17] Meryem Simsek, Dan Zhang, David Öhmann, Maximilian Matthé, and Gerhard Fettweis. On the Flexibility and Autonomy of 5G Wireless Networks. *IEEE Access*, PP(PP), 2017.

[TB99a] C C Tan and N C Beaulieu. An investigation of transmission properties of Xia pulses. In *Communications, 1999. ICC '99. 1999 IEEE International Conference on*, volume 2, pages 1197–1201 vol.2, 1999.

[tB99b] Stephan ten Brink. Convergence of iterative decoding. *IEEE Electronics Letters*, 35(10):806–808, 1999.

[TJC99] Vahid Tarokh, Hamid Jafarkhani, and a. Robert Calderbank. Space âĂŞ Time Block Codes from Orthogonal Designs. *IEEE Transactions on Information Theory*, 45(5):1456–1467, 1999.

[TV05] David Tse and Pramod Viswanath. *Fundamentals of Wireless Communication.* Cambridge University Press, Cambridge, 2005.

[TWD+15] Nihat Engin Tunali, Michael Wu, Chris Dick, Christoph Studer, and San Jose. Linear Large-Scale MIMO Data Detection for 5G Multi-Carrier Waveform Candidates. In *Asilomar Conference on Signals, Systems, and Computers*, pages 1–5, 2015.

[VBDH17] Mathieu Van Eeckhaute, André Bourdoux, Philippe De Doncker, and François Horlin. Performance of emerging multi-carrier waveforms for 5G asynchronous communications. *EURASIP Journal on Wireless Communications and Networking*, 2017(1):29, 2017.

[VBTV15] Wantanee Viriyasitavat, Mate Boban, Hsin-Mu Tsai, and Athanasios V. Vasilakos. Vehicular Communications - Survey and Challenges of Channel and Propagation Models. *IEEE VEHICULAR TECHNOLOGY MAGAZINE*, 1(June 2015), 2015.

[VWS+13] Vida Vakilian, Thorsten Wild, Frank Schaich, Stephan ten Brink, and Jean-Francois Frigon. Universal-Filtered Multi-Carrier Technique for Wireless Systems Beyond LTE. In *9th International Workshop on Broadband Wireless Access (BWA) @ IEEE Globecom'13*, 2013.

[VZV+16] Jaakko Vihriälä, Ali A Zaidi, Venkatkumar Venkatasubramanian, Ning He, Esa Tiirola, Jonas Medbo, and Eeva Lähetkangas. Numerology and Frame Structure for 5G Radio Access. In *Personal, Indoor, and Mobile Radio Communications (PIMRC), 2016 IEEE 27th Annual International Symposium on*, pages 2–6, 2016.

[WBKK03] D. Wubben, R. Bohnke, V. Kuhn, and K.D. Kammeyer. MMSE extension of V-BLAST based on sorted QR decomposition. *2003 IEEE 58th Vehicular Technology Conference. VTC 2003-Fall (IEEE Cat. No.03CH37484)*, 1(1):0–4, 2003.

[WFGV98] P.W. Wolniansky, G.J. Foschini, G.D. Golden, and R.A. Valenzuela. V-BLAST: an architecture for realizing very high data rates over the rich-scattering wireless channel. In *Signals, Systems, and Electronics, 1998. ISSSE 98. 1998 URSI International Symposium on*, 1998.

[WJK+14] Gerhard Wunder, Peter Jung, Martin Kasparick, Thorsten Wild, Frank Schaich, Yejian Chen, Stephan Brink, Ivan Gaspar, Nicola Michailow, Andreas Festag, Luciano Mendes, Nicolas Cassiau, Dimitri Ktenas, Marcin Dryjanski, Slawomir Pietrzyk, Bertalan Eged, Peter Vago, and Frank Wiedmann. 5GNOW: non-orthogonal, asynchronous waveforms for future mobile applications. *IEEE Communications Magazine*, 52(2):97–105, feb 2014.

[Woj07] Piotr Wojdyllo. Modified Wilson Orthonormal Bases. *Sampling Theory in Signal and Image Processing*, 6(2):223—-235, 2007.

[WOJ08] P WOJDYŁŁO. Characterization of Wilson systems for general lattices. *International Journal of Wavelets, Multiresolution ...*, 6(2):305–314, 2008.

[WQK+14] Matthias Wildemeersch, Tony Q. S. Quek, Marios Kountouris, Alberto Rabbachin, and Cornelis H. Slump. Successive Interference Cancellation in Heterogeneous Networks. *IEEE Transactions on Communications*, 62(12), 2014.

[WR90] J. Wexler and S. Raz. Discrete Gabor expansions. *Signal Processing*, 21(3):207–220, nov 1990.

[WSJM11] Dirk Wubben, Dominik Seethaler, Joakim Jalden, and Gerald Matz. Lattice Reduction. *IEEE Signal Processing Magazine*, 28(3):70–91, may 2011.

[WV99] Xiaodong Wang and H. Vincent Poor. Iterative (Turbo) soft interference cancellation and decoding for coded CDMA. *IEEE Transactions on Communications*, 47(7):1046–1061, 1999.

[WXXL16] Peng Wei, Xiang Gen Xia, Yue Xiao, and Shaoqian Li. Fast DGT-Based Receivers for GFDM in Broadband Channels. *IEEE Transactions on Communications*, 64(10):4331–4345, 2016.

[WZR+16] Mao Wang, Jingjing Zhang, Bingying Ren, Wenjie Yang, Jun Zou, Min Hua, and Xiaohu You. The Evolution of LTE Physical Layer Control Channels. *IEEE Communications Surveys and Tutorials*, 18(2):1336–1354, 2016.

[Xia97] XG Xia. A family of pulse-shaping filters with ISI-free matched and unmatched filter properties. *Communications, IEEE Transactions on*, 45(10):1157–1158, 1997.

[YGR16] Ayhan Yenilmez, Tansal Gucluoglu, and Piotr Remlein. Performance of GFDM-maximal ratio transmission over Nakagami-m fading channels. In *Proceedings of the International Symposium on Wireless Communication Systems*, pages 523–527, 2016.

[YH15] Shaoshi Yang and Lajos Hanzo. Fifty Years of MIMO Detection: The Road to Large-Scale MIMOs. *IEEE Communications Surveys & Tutorials*, 17(4):1941–1988, 2015.

[ZBC+14] a Zanella, N. Bui, a Castellani, L. Vangelista, and M. Zorzi. Internet of Things for Smart Cities. *IEEE Internet of Things Journal*, 1(1):22–32, 2014.

[ZFF17] Dan Zhang, Andreas Festag, and Gerhard Fettweis. Performance of Generalized Frequency Division Multiplexing Based Physical Layer in Vehicular Communication. *IEEE Transactions on Vehicular Technology*, 9545(c), 2017.

[ZJC+15] X Zhang, M Jia, L Chen, J Ma, and Jing Qiu. Filtered-OFDM-Enabler for Flexible Waveform in The 5th Generation Cellular Networks. In *2015 IEEE Globecom*, 2015.

[ZMM+16] Dan Zhang, Luciano Leonel Mendes, Maximilian Matthé, Ivan Simões Gaspar, Nicola Michailow, and Gerhard P Fettweis. Expectation Propagation for Near-Optimum Detection of MIMO-GFDM Signals. *IEEE TRANSACTIONS ON WIRELESS COMMUNICATIONS*, 15(2):1045–1062, 2016.

[ZMMF15] Dan Zhang, Maximilian Matthé, Luciano Leonel Mendes, and Gerhard Fettweis. A Markov Chain Monte Carlo Algorithm for Near-Optimum Detection of MIMO-GFDM Signals. In *IEEE 26th International Symposium on Personal, Indoor and Mobile Radio Communications - (PIMRC '15)*, pages 281–286, 2015.

[ZMMF16] Dan Zhang, Maximilian Matthé, Luciano Leonel Mendes, and Gerhard Fettweis. Message Passing Algorithms for Upper and Lower Bounding the Coded Modulation Capacity in a Large-scale Linear System. *IEEE Signal Processing Letters*, 23(4):537–540, 2016.

[ZMMF17] Dan Zhang, Maximilian Matthe, Luciano Leonel Mendes, and Gerhard P. Fettweis. A Study on the Link Level Performance of Advanced Multicarrier Waveforms under MIMO Wireless Communication Channels. *IEEE Transactions on Wireless Communications*, PP(99), 2017.

[ZMSR16] R. Zayani, Y. Medjahdi, H. Shaïek, and D. Roviras. WOLA-OFDM: A potential candidate for asynchronous 5G. In *2016 IEEE Globecom Workshops, GC Wkshps 2016 - Proceedings*, 2016.

[ZSW+15] Zhao Zhao, Malte Schellmann, Qi Wang, Xitao Gong, Ronald Boehnke, and Wen Xu. Pulse shaped OFDM for asynchronous uplink access. In *Asilomar Conference on Signals, Systems and Computers*, pages 3–7, 2015.